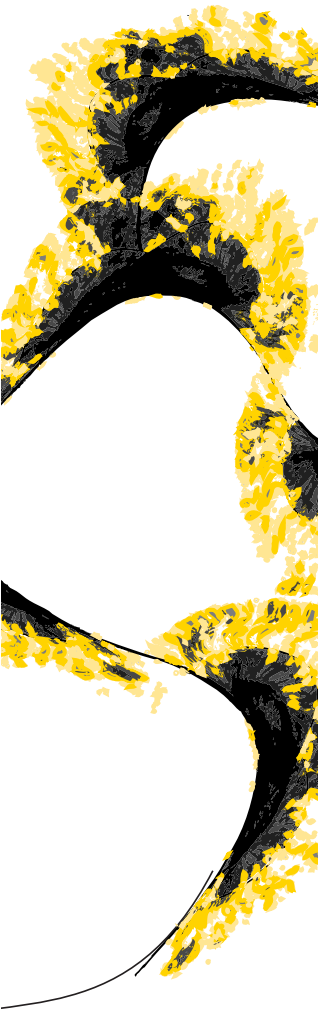

RAM ROBOTICS AND MECHATRONICS

3D PRINTED DIFFERENTIAL FORCE AND POSITION SENSOR BASED ON LOSSY TRANSMISSION LINES

P. (Parth) Patel

MSC ASSIGNMENT

Committee:
prof. dr. ir. G.J.M. Krijnen
ir. M. Schouten
dr. ir. R.A.R. van der Zee

March, 2021

016RaM2021
Robotics and Mechatronics
EEMCS
University of Twente
P.O. Box 217
7500 AE Enschede
The Netherlands

UNIVERSITY OF TWENTE. | TECHMED CENTRE UNIVERSITY OF TWENTE. | DIGITAL SOCIETY INSTITUTE

Abstract

Recent developments in 3D printing, also known as additive manufacturing, have helped the fabrication of conductive structures, such as force sensors. This project aims to design and manufacture a flexible force sensor based on a transmission line model using Fused Deposition Modelling (FDM), a 3D printing technology technique. Usually, 3D printed sensors exhibit anisotropic behaviour and have imperfections that affect the sensors' electrical properties. For example, the plates' resistance in a capacitive force sensor limits the maximum possible readout frequency. The force sensor is a flexible parallel plate capacitor printed using a flexible conductive carbon black-filled Thermoplastic Polyurethane (TPU). The force applied to the sensor changes the sensor's resistance and capacitance, which changes the impedance. The change in the impedance is measured using an in house developed multi-frequency impedance analyzer. Using this method, we measured both the total force applied and the location where the force is applied, using a low complexity sensor with a minimal number of connections. The resulting 3D printed sensor is highly customizable and hence, shows great potential for implementation in prosthetic and robotics applications.

Acknowledgements

I want to take this opportunity to thank the people without whom this thesis would not have been possible.

First and foremost, I would like to thank my supervisor, dr. Gijs Krijnen, for his valuable feedback, support and guidance throughout my thesis; thanks for not losing faith in me. I want to thank my daily supervisor ir. Martijn for his constant support throughout my thesis. Thanks for being patient and trusting me, especially during the experimental phase

I would like to thank the members of the NIFTy group for their valuable feedback.

Finally, I would like to thank my parents and my friends for their support throughout my master program. This journey would not have been possible without you guys.

Shukriya!

List of Figures

List of Tables

Contents

1 Introduction

This report describes the work of Parth Patel for his Master thesis. The goal of the assignment is to design and fabricate a 3D printed capacitive pressure sensor. This sensor uses the piezoresistive properties of the electrodes to simultaneously determine the magnitude and position of an applied force.

1.1 Context

3D printing is a recent trend in engineering, especially soft robotics which involves fabrication of 3D components layer by layer from raw materials. The technology offers versatile manufacturing and free customization, reducing the cost of manufacturing and lead time of the prototype. The higher level of design complexity and the reduction of assembly make this technology interesting for fabricating electronic components and complex sensors [4–7].

The most common technique for 3D printing is material extrusion, also known as Fused Deposition Modelling (FDM). It involves extruding a thermoplastic filament through use of an extruder, a heater and a nozzle, at temperatures high enough to melt the material. The melted material settles on the print bed and solidifies; this process is repeated layer by layer until a desired 3D object is obtained. FDM can be used with very flexible materials such as Thermoplastic polyurethane (TPU) and Conductive thermoplastic polyurethane (eTPU) figure 1.1 shows the schematic of an FDM printing technique.

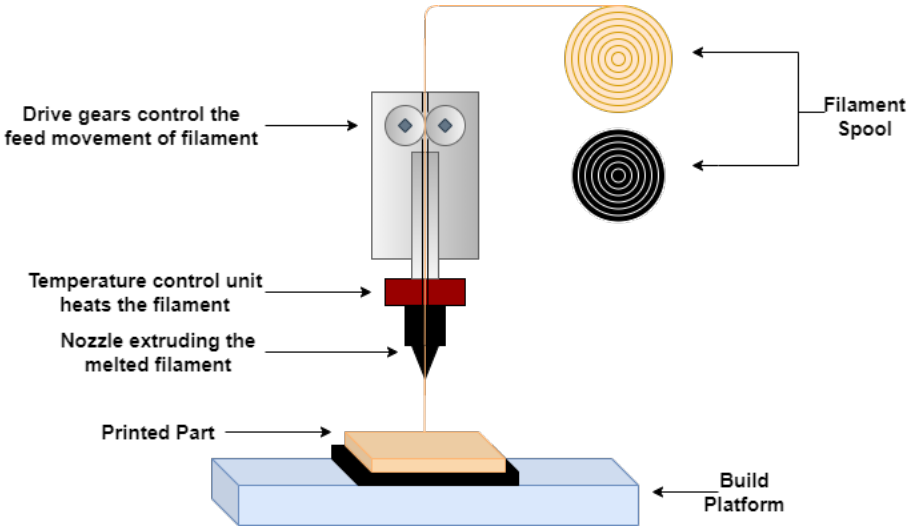

Figure 1.1: Fused Deposition Modelling

1.2 Project Goals

The assignment aims to address the following research question:

Is it possible to design and fabricate a sensor that can measure the magnitude and position of an applied force by measuring the change in impedance?

This research question is answered by addressing the following sub-questions:

1. **Which operating principle of the force sensor can be used to measure the magnitude and position of an applied force?**
2. **How can the sensor's electrical characteristics be modelled?**

3. **How can the sensor be designed, fabricated and tested based on this analytical model?**
4. **How can we determine the force and position from the impedance values?**

1.3 Approach

Since the assignment is research-oriented, a scientific approach will be used, followed by an engineering approach. A model originally developed by Gijs krijnen will be used and extended accordingly. MATLAB® calculations of the analytical model will be performed, which will then be verified with experimental results.

1.3.1 Definition

The experiments were done iteratively, and a total of five sensors were design and fabricated. For simplicity, these sensors will be referred by their abbreviations throughout the report. Below listed are the abbreviations of the sensors:

1. SNJ - Parallel plate sensor with Ninjaflex dielectric.
2. SX60 - Parallel plate sensor with X60 dielectric.
3. SESX60 - Same electrode size parallel plate sensor with X60 dielectric.
4. DSNJX60 - Differential sensor with Ninjaflex and X60 dielectric.
5. DSX60INF - Differential sensor with X60 dielectric.

1.4 Report Structure

The organisation of the thesis is done as follows:

Chapter 2 presents the literature survey followed by the analytical modelling and MATLAB® implementation of the proposed parallel plate and differential sensor. An inverse model to determine the force and position is implemented in the MATLAB®.

chapter 3 explains the material used to fabricate the sensors along with the effects of printing parameters on the electrical properties of the sensor. Design and fabrication of all five sensors is illustrated

chapter 4 discusses the type of experiments performed to characterize the change in impedance as a function of magnitude and position of an applied force. The experimental setup and the readout techniques are discussed.

chapter 5 presents an analysis of the results of an iterative experimental process of all the five sensor. The analysis justifies the reason behind of why a new sensor was designed, modelled and fabricated.

chapter 6 concludes this research by answering the main research questions and sub-questions along with the discussion and future scope.

2 Background and Modelling

2.1 Introduction

This chapter gives a literature overview of the previously published work related to 3D printed sensors, followed by the analytical model and MATLAB® implementation of the sensors designed in this assignment.

2.2 Related Work

2.2.1 Force Sensors and Pressure sensors

A force sensor converts applied forces into an electrical signal. Generally, a force sensor consists of 3 components, 1) Flexure, which converts the applied forces along a specific direction into displacement or strain. 2) A transducer that converts the displacement into an electric signal. 3) Packaging to protect the flexure and transducer. Force sensors have a vast number of applications, some of them include manufacturing, robotics, transportation, automotive industry, etc. However, general-purpose commercial force sensors have limitations such as lack of design and application specificity. In order to measure a pressure distribution, many sensors are needed, and in order to get a high spatial resolution, a technique with high spatial resolution is needed. The advantages of 3D printing technology discussed in section 1.1 overcome these limitations and can be used to fabricate an easily customizable, flexible force sensor [8].

Schouten et al. [9] developed a flexible force capacitive force sensor using Fused deposition modelling (FDM). The sensor consisted of a parallel plate capacitor. The electrodes were printed using the conductive Thermoplastic polyurethane (eTPU), and the dielectric between the electrode was printed using X60 ultra-flexible filament. The sensor showed good response to the applied force; the measured change in capacitance was 160 fF at a change in the force of 6.6 N at the operating frequency of 25 kHz and a voltage of 1 V.

Wolterink et al. [10] developed a thin, flexible capacitive force sensor based on the anisotropy in the 3D printed structures using FDM. The sensor was fabricated by depositing two thin layers of eTPU. Conductive 3D printed structures printed using FDM have anisotropic properties; this is due to high inter-layer resistance compared to the material's resistance. This results in poor resistive coupling and dominant capacitive coupling between layers. The force applied to the flexible material; changes distance between the layers resulting in capacitance change. This principle eliminated the extra dielectric layer between the electrodes. The sensor showed non-linear capacitance force behaviour due to the material properties, including creep and dampening.

Xavier et al. [11] developed a fully FDM 3D printed capacitive transducer. TPU was used as a dielectric, and semi-rigid carbon-based b polylactic acid (PLAcb) was used as electrically conductive electrodes. Different samples with varying dielectric thickness were fabricated and used. The sensor's relative sensitivity is independent of the dielectric thickness and depends on the electrode's Young modulus and area. To confirm this, four samples with different dielectric thickness were used. The samples were subjected to load tests and the relative sensitivity was consistent across all four samples. The 2 mm^2 electrode area, in combination with a 400 µm dielectric, resulted in a capacitance change of 857 fF.

Saari et al. [12] developed a capacitive force sensor by combining the advantages of a fibre encapsulation additive manufacturing (FEAM) and thermoplastic elastomer additive manufacturing (TEAM). The sensor consisted of an Acrylonitrile butadiene styrene (thermoplastic polymer)-based rigid frame encapsulating a copper wire. Thermoplastic elastomer (TPE) material was used to print the dielectric. The sensor was subjected to a uniaxial load test and the

sensor showed good results except for a delay of 8.3 seconds during unloading due to material hysteresis.

C Hong et al. [13, 14] developed a fibre Bragg grating (FBG) based pressure sensor using the FDM process to monitor vertical pressures. FBG is a sensing element in an optical fibre used to measure stress, strain, temperature, displacement and pressure. The sensor was fabricated by embedding the FBG sensor into the PLA material during the printing process. Vertical pressure applied on the sensor's surface results in the FBG sensor's elongation, which exhibits a wavelength change. The change in wavelength was used to determine the applied pressure. The sensor was subjected to cyclic loading tests. The measurement results showed a consistent change of wavelengths to the applied pressure. The stress-strain relationship was linear at high pressure. However, the optical fibre sensors are expensive to fabricate.

From the papers discussed above can it can be concluded that it is possible to 3D print a capacitive force sensor to determine the vertical force. Thermoplastic polyurethane (TPU) is a good choice to print the dielectric of the sensor due to its flexibility and the conductive variant of TPU (eTPU) material can be used to print the flexible electrodes.

Emon et al [15] a soft stretchable pressure sensor using multi-material printing. The five-layer sensor incorporated three different materials: the insulation, the conductive electrodes and the pressure-sensitive layer. The pressure-sensitive layer was sandwiched between the conductive electrodes, and the top and bottom insulating layers encapsulated these layers. The sensing unit taxel is formed at each point where the electrodes cross each other. A 2 x 2 electrode configuration (4 taxels) sensor was fabricated. Force applied manually on one of the taxels, and the resulting response was recorded in terms of the change in ΔV_{out}.

Joo et al. [16] developed a sensitive and flexible capacitive pressure sensor. The top electrode was fabricated using the Polydimethylsiloxane (PDMS) surface embedded with silver nanowires (AgNW). The bottom electrode was inkjet printed on the flexible Arylite substrate, and the dielectric layer of Polymethyl methacrylate (PMMA) was spin-coated onto the bottom electrode. The pressure was applied to test the sensitivity of the capacitive sensor. The sensor was able to detect small forces and had a faster response time. The sensor was further scaled into 3x3 and 5x5 pixel type pressure sensor array to detect spatial pressure. The same group developed another flexible capacitive sensor with tunable sensitivity by controlling the PDMS matrix's mixing ratios, which changed the PDMS matrix's mechanical properties and the buckled structure's crest shape [17]. However, if compared to the FDM printed sensors, this fabrication process is complex and time-intensive. Metal induced conductive filling suffers from oxidation, instability in conductivity which results in poor accuracy and reproducibility [18].

Woo et al. [19] developed a 4x4 capacitive pressure sensor array consisting of conductive elastomeric ink (carbon nanotube (CNT)-doped PDMS matrix. The fabricated sensor was a combination of soft-lithographic replication and micro-contact printing (μCP) [20]. Ecoflex based polymer was used as a dielectric between the two CPDMS electrodes. To evaluate the sensor performance, the sensor was applied with a normal force of 20N, including other tests such as twisting, bending, stretching and folding. The sensor was mechanically robust, and the sensor's electrical response was highly linear with very low hysteresis suitable for detecting spatial pressure. The sensor was further tested on a human finger as a skin-like sensor to demonstrate the sensor's practical usability. However, the sensor is not scalable as every NxN array requires 2N electrical connections making the system more complex. The throughput is lower as compared to FDM as the manufacturing process is complex and involves several steps. The mechanical properties of the PDMS affect the reproducibility [21, 22].

Xu et al. [23] developed a soft, flexible and stretchable programmable rubber keyboard. The keyboard uses dielectric elastomer (DE) sheets that were made from a PDMS dielectric of approximately 100 um in thickness sandwiched between two conductive PDMS electrodes doped

with carbon black particles. The transmission line model is used to localize the pressure. The distributed resistance within the DE's electrodes has a lossy nature, creating a voltage gradient across the electrodes for different sensing signals. The DE electrodes are treated as an infinite chain of resistor and capacitor segments (transmission line model), each acting as a low-pass filter to account for the high resistance. The lower capacitive signals maintain the strength through the entire sheet while higher frequencies signal get attenuated as they further travel into the electrode. The target location of pressure can be determined by performing electrical separation using a signal with low and high-frequency components and comparing their respective capacitive changes. The sensor was fabricated by laminating two DE sheets on top of each other oriented at 90 degrees (y and y direction). For testing, the sensor sheet was artificially divided into 4 quadrants (with no physical separation). Two different capacitance sensing circuits were created to excite the keyboard in x and y direction and sensing frequencies of 1KHZ and 60KHZ were chosen after the frequency sweep. Capacitance change of higher frequency in both x and y direction was used simultaneously to determine which quadrant was pressed. The capacitance change is bigger when pressed near the origin than when pressed further away from the origin. The lower frequency capacitance change was used to determine the amount of pressure applied. This multi-frequency approach was used to scale the sensor from a 2x2 array to 3x3 array. The sensor can be subdivided to increase the resolution; however, there is a limit as each additional section reduces the area of the section, which reduces the difference in capacitance between two adjacent frequencies.

The lossy transmission line principle presented by Xu et al. will be used to localize the applied force and to characterize the sensors illustrated in this assignment.

2.3 Analytical Model

FDM printed 3D structures have anisotropic electrical properties. The printing process parameters such as raster angle, layer thickness, and air gap influence the resistivity due to voids and bonding conditions between adjacent layers. Conductive paths parallel to the printed structure has a lower resistivity than paths perpendicular to the structure [24, 25]. To characterize the electrical anisotropy in conductive structures, the model of Gijs Krijnen discussed in Alexander's report is used. The model of Gijs Krijnen tries to model the conduction in 3D printed structures as a collection of track elements known as traxels, assuming they exist. FDM printed 3D model consist of a finite number of traxels printed in discrete line elements.

The 3D printed sensor proposed in this assignment is a parallel plate capacitor printed traxel by traxel, layer by layer. The cross-section of the proposed sensor is shown in figure 2.1. The sensor is formed by layer of dielectric of thickness d printed using thermoplastic polyurethane (TPU) sandwiched between two conductive layers printed using conductive thermoplastic polyurethane acting as electrodes of the capacitor. The sensor has length L in x-direction, width W in y-direction and height H in z-direction. 3D printed capacitive sensors behave like a lossy transmission. Figure 4.5 shows the measurement setup and the electrical connections to the sensor. The flow of current is due to changing potential, the current and voltage across each electrode can be described using a set of differential equations which can be solved using the eigen-values and corresponding eigen-vectors with coefficients determined by the possible boundary conditions.

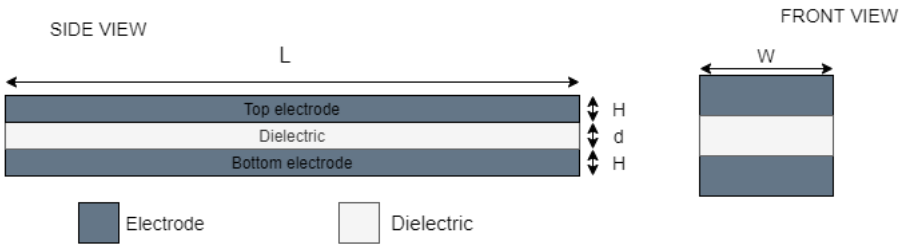

Figure 2.1: Schematic diagram of the proposed sensor.

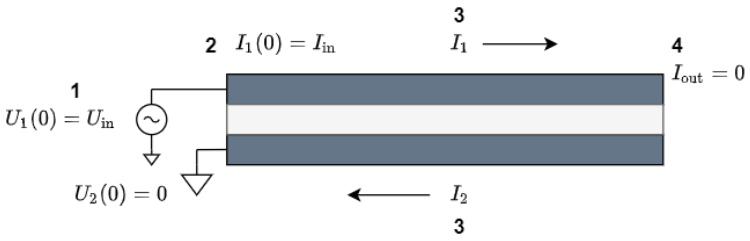

Figure 2.2: Possible boundary conditions

Boundary conditions

To solve for the coefficients there are four possible boundary conditions for voltage and current at $x = 0$ and $x = L$ as shown in figure 2.2:

1. Fixed voltage: The top electrode is connected to fixed voltage supply U_{in} and the bottom electrode is connected to the ground.

$$\begin{aligned} U_1(0) &= U_{in} \\ U_2(0) &= 0 \end{aligned} \tag{2.1}$$

2. Fixed current: The current at the input of the sensor:

$$I_1(0) = I_{in} \tag{2.2}$$

3. Open connections: The sensor is not connected on the other side (open connections).

$$I_{out}(L) = 0 \tag{2.3}$$

4. Since there is no output current, all the current going in will return to the source.

$$I_1(L) = -I_2(L) \tag{2.4}$$

2.3.1 Model Calculation

The parallel plate capacitive sensor is represented by its equivalent circuit diagram of a lossy transmission line (figure 2.3) [23]. For simplicity we assume that the electrode is purely resistive. The resistance of the sensor of Δx width can be defined as $R = \frac{\rho \Delta x}{HW}$ with ρ being the volume resistivity of the electrode in Ωm.

If an infinitesimal part of the sensor is considered, due to potential difference in track U_1, the current flows from left to right and can be described using the following differential equations [26]:

$$I_1(x,t) = \frac{\Delta U_1(x,t)}{R_n} = \frac{-HW}{\rho} \frac{\Delta U_1(x,t)}{\Delta x} \tag{2.5}$$

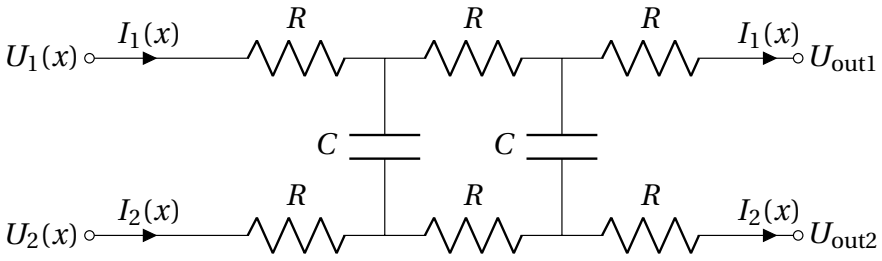

Figure 2.3: Electrical diagram of the transmission line. This structure is repeated unlimited to times to form the sensor.

Taking the limit for $\Delta x \to 0$:

$$I_1(x,t) = \frac{-HW}{\rho}\frac{\partial U_1(x,t)}{\partial x} \tag{2.6}$$

This equation is in the time-domain form. However, impedance is estimated in frequency domain and the Fourier transform of the above equation yields:

$$\hat{I}_1(x,\omega) = \frac{-HW}{\rho}\frac{\partial \hat{U}_1(x,\omega)}{\partial x} \tag{2.7}$$

Differentiating the above expression to x gives a second order term for voltage.

$$\frac{\partial \hat{I}_1(x,\omega)}{\partial x} = \frac{-HW}{\rho}\frac{\partial^2 \hat{U}_1(x,\omega)}{\partial x^2} \tag{2.8}$$

The capacitance can be calculated using a parallel plate approximation given by:

$$C = \frac{\varepsilon_0 \varepsilon_r A}{d} \tag{2.9}$$

where A is the area of the plates, d is the distance between the plates, ε_0 is the permittivity of vacuum $\mathrm{F\,m^{-1}}$ and ε_r the relative permittivity.

$$C = \frac{\varepsilon_0 \varepsilon_r W \Delta x}{d} \tag{2.10}$$

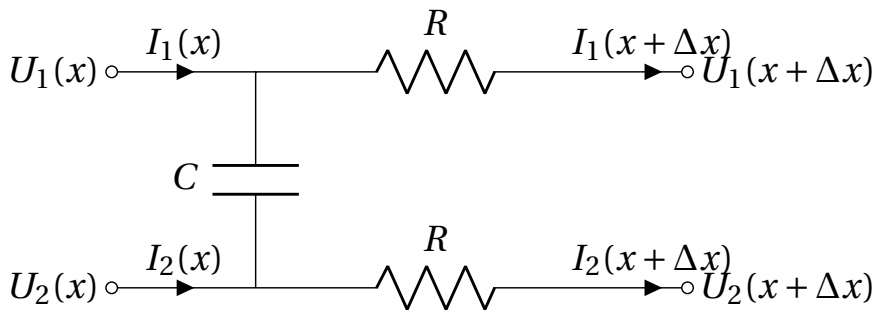

Figure 2.4: Electrical diagram for the infinitesimal part of the sensor

The current through the capacitor C flows due to the temporal changes in potential difference U_2 to U_1 . The current I_c through the capacitor is expressed in Fourier transform assuming harmonic functions:

$$\hat{I}_1(x+\Delta x,\omega) - \hat{I}_1(x,\omega) = -\hat{I}_c(\omega) \tag{2.11}$$

$$\hat{I}_1(x+\Delta x,\omega)-\hat{I}_1(x,\omega)=\frac{-\left(\hat{U}_2(x,\omega)-\hat{U}_1(x,\omega)\right)}{\hat{Z}_{\mathrm{eq}}(\omega)} \tag{2.12}$$

The impedance between the two plates is given by:

$$\hat{Z}_{\mathrm{eq}}(\omega)=\frac{1}{j\omega C}=\frac{d}{j\omega\varepsilon_0\varepsilon_{\mathrm{r}}W\Delta x} \tag{2.13}$$

Combining equation 2.12 and 2.13 we get,

$$\hat{I}_1(x+\Delta x,\omega)-\hat{I}_1(x,\omega)=\frac{j\omega\varepsilon_0\varepsilon_{\mathrm{r}}W\Delta x\left(\hat{U}_1(x,\omega)-\hat{U}_2(x,\omega)\right)}{d} \tag{2.14}$$

Considering the slice of the sensor to be extremely thin, the expression can be re-written by means of partial derivatives:

$$\frac{\partial\hat{I}_1(x,\omega)}{\partial x}\rightarrow\frac{-HW}{\rho}\frac{\partial^2\hat{U}_1(x,\omega)}{\partial x^2}=\frac{j\omega\varepsilon_0\varepsilon_{\mathrm{r}}W\left(\hat{U}_1(x,\omega)-\hat{U}_2(x,\omega)\right)}{d} \tag{2.15}$$

The W term occurs on both sides and drops out and multiplying the negative sign inside we get:

$$\frac{\partial^2\hat{U}_1(x,\omega)}{\partial x^2}=\frac{\rho\, j\omega\varepsilon_0\varepsilon_{\mathrm{r}}\left(\hat{U}_{2,}(x,\omega)-\hat{U}_1(x,\omega)\right)}{Hd} \tag{2.16}$$

We introduce a conduction parameter:

$$\Gamma=\frac{j\omega\varepsilon_0\varepsilon_{\mathrm{r}}\rho}{Hd} \tag{2.17}$$

Substituting 2.17 in 2.16 yields a second order differential equation for top track:

$$\frac{\partial^2\hat{U}_1(x,\omega)}{\partial x^2}-\Gamma\left(\hat{U}_2(x,\omega)-\hat{U}_1(x,\omega)\right)=0 \tag{2.18}$$

Similarly, solving for the bottom track the differential equation is given by:

$$\frac{\partial^2\hat{U}_2(x,\omega)}{\partial x^2}-\Gamma\left(\hat{U}_1(x,\omega)-\hat{U}_2(x,\omega)\right)=0 \tag{2.19}$$

This set of equations can be written in matrix form $\frac{\partial^2\vec{U}}{\partial x^2}=A\vec{U}$ which yields the eigen value problem:

$$(A-\lambda^2 I)\vec{U}=\begin{Bmatrix}\Gamma-\lambda^2 & -\Gamma\\ -\Gamma & \Gamma-\lambda^2\end{Bmatrix}\begin{Bmatrix}U_1\\ U_2\end{Bmatrix}=0 \tag{2.20}$$

with

$$A=\begin{Bmatrix}\Gamma & -\Gamma\\ -\Gamma & \Gamma\end{Bmatrix} \tag{2.21}$$

The solution of these two coupled differential equations 2.18 and 2.19 is given by:

$$\vec{\hat{U}}_1(x,\omega)=B_{1,1}e^{\lambda_1 x}+B_{1,2}e^{\lambda_2 x}+B_{1,3}e^{\lambda_3 x}+B_{1,4}e^{\lambda_4 x} \tag{2.22}$$

$$\vec{\hat{U}}_2(x,\omega)=B_{2,1}e^{\lambda_1 x}+B_{2,2}e^{\lambda_2 x}+B_{2,3}e^{\lambda_3 x}+B_{2,4}e^{\lambda_4 x} \tag{2.23}$$

Which can be written as a single equation by using eigen vectors:

$$\begin{Bmatrix}\vec{\hat{U}}_1(x,\omega)\\ \vec{\hat{U}}_2(x,\omega)\end{Bmatrix}=B_1\vec{\eta_1}e^{\lambda_1 x}+B_2\vec{\eta_2}e^{\lambda_2 x}+B_3\vec{\eta_3}e^{\lambda_3 x}+B_4\vec{\eta_4}e^{\lambda_4 x} \tag{2.24}$$

Solving for the eigen values λ by taking the determinant of equation 2.21 yields:

$$\lambda_{1,2} = 0, \lambda_3 = \sqrt{2\Gamma}, \lambda =_4 -\sqrt{2\Gamma} \tag{2.25}$$

This means equation 2.24 can be re-written as:

$$\overrightarrow{\hat{U}}(x,\omega) = B_1\overrightarrow{\eta_1} + B_2\overrightarrow{\eta_2}x + B_3\overrightarrow{\eta_3}e^{\sqrt{2\Gamma}x} + B_4\overrightarrow{\eta_4}e^{-\sqrt{2\Gamma}x} \tag{2.26}$$

Solving for the eigen vectors $\overrightarrow{\eta}$ we get,

$$\begin{aligned} \overrightarrow{\eta}_1 = \overrightarrow{\eta}_2 &= \begin{Bmatrix} 1 \\ 1 \end{Bmatrix} \\ \overrightarrow{\eta}_3 = \overrightarrow{\eta}_4 &= \begin{Bmatrix} 1 \\ -1 \end{Bmatrix} \end{aligned} \tag{2.27}$$

Which results in:

$$\overrightarrow{\hat{U}}(x,\omega) = \begin{Bmatrix} \overrightarrow{\hat{U}}_1(x,\omega) \\ \overrightarrow{\hat{U}}_2(x,\omega) \end{Bmatrix} = B_1 \begin{Bmatrix} 1 \\ 1 \end{Bmatrix} + B_2 \begin{Bmatrix} 1 \\ 1 \end{Bmatrix} x + B_3 \begin{Bmatrix} 1 \\ -1 \end{Bmatrix} e^{-\sqrt{2\Gamma}x} + B_4 \begin{Bmatrix} 1 \\ -1 \end{Bmatrix} e^{\sqrt{2\Gamma}x} \tag{2.28}$$

To solve for the B's the boundary conditions need to be applied. The **first boundary condition** (2.1) is applied where the input voltage U_{in} is applied in the U_1 track and the U_2 track is connected to the ground, which means equation 2.28 becomes:

$$\hat{U}_1(0,\omega) = \hat{U}_{\text{in}} = B_1 + B_3 + B_4 \tag{2.29}$$

$$\hat{U}_2(0,\omega) = 0 = B_1 - B_3 - B_4 \tag{2.30}$$

Solving 2.29 and 2.30 yields B_1:

$$B_1 = B_3 + B_4 = B_1 = \frac{\hat{U}_{\text{in}}}{2} \tag{2.31}$$

When current is taken as the boundary condition, the derivative of equation 2.28 can be used:

$$\frac{\partial \overrightarrow{\hat{U}}(x,\omega)}{\partial x} = B_2 \begin{Bmatrix} 1 \\ 1 \end{Bmatrix} - B_3 \begin{Bmatrix} 1 \\ -1 \end{Bmatrix} \sqrt{2\Gamma} e^{-\sqrt{2\Gamma}x} + B_4 \begin{Bmatrix} 1 \\ -1 \end{Bmatrix} \sqrt{2\Gamma} e^{\sqrt{2\Gamma}x} \tag{2.32}$$

the above equation is solved for current (I) at a length L of the traxel:

$$\overrightarrow{\hat{I}}(L,\omega) = \frac{-HW}{\rho} \left(B_2 \begin{Bmatrix} 1 \\ 1 \end{Bmatrix} - B_3 \begin{Bmatrix} 1 \\ -1 \end{Bmatrix} \sqrt{2\Gamma} e^{-\sqrt{2\Gamma}L} + B_4 \begin{Bmatrix} 1 \\ -1 \end{Bmatrix} \sqrt{2\Gamma} e^{\sqrt{2\Gamma}L} \right) \tag{2.33}$$

Using the **fourth boundary condition** (2.4) the current in both tracks will be equal and opposite $\hat{I}_1(L,\omega) = -\hat{I}_2(L,\omega)$

$$\hat{I}_1(L,\omega) = \frac{HW}{\rho} \left(-B_2 + B_3\sqrt{2\Gamma} e^{-\sqrt{2\Gamma}L} - B_4\sqrt{2\Gamma} e^{\sqrt{2\Gamma}L} \right) \tag{2.34}$$

$$\hat{I}_2(L,\omega) = \frac{HW}{\rho} \left(-B_2 - B_3\sqrt{2\Gamma} e^{-\sqrt{2\Gamma}L} + B_4\sqrt{2\Gamma} e^{\sqrt{2\Gamma}L} \right) \tag{2.35}$$

solving the above two equations gives that coefficient B_2 as 0. Using the **second boundary condition** (2.2) the input current at track U_1 will be $\hat{I}_1(0,\omega) = \hat{I}_{\text{in}}$

$$\hat{I}_{\text{in}} = \frac{HW}{\rho} \left(B_3\sqrt{2\Gamma} - B_4\sqrt{2\Gamma} \right) \tag{2.36}$$

Solving equation 2.36 and 2.31 yields B_3 and B_4:

$$B_4 = \frac{-2\hat{I}_{\text{in}}\rho + HW\hat{U}_{\text{in}}\sqrt{2\Gamma}}{4HW\sqrt{2\Gamma}} \tag{2.37}$$

$$B_3 = \frac{\hat{U}_{\text{in}}}{2} - B_4 = \frac{\sqrt{2}\hat{I}_{\text{in}}\rho + H\sqrt{\Gamma}\hat{U}_{\text{in}}W}{4H\sqrt{\Gamma}W} \tag{2.38}$$

Hence the output current at length L will be:

$$\hat{I}_{\text{out}}(L,\omega) = \frac{e^{-\sqrt{2\Gamma}L}HW\left(2(1+e^{\sqrt{2\Gamma}2L})\hat{I}_{\text{in}}\rho + \sqrt{2}(-1+e^{\sqrt{2\Gamma}2L})H\sqrt{\Gamma}\hat{U}_{\text{in}}W\right)}{4H\rho W} \tag{2.39}$$

The output voltage at a certain length L is $\hat{U}_{\text{out1}}$ and $\hat{U}_{\text{out2}}$ which are given by:

$$\hat{U}_{\text{out1}} = \hat{U}_1(L,\omega) = B_1 + B_3e^{-\sqrt{2\Gamma}L} + B_4e^{\sqrt{2\Gamma}L} \tag{2.40}$$

$$\hat{U}_{\text{out2}} = \hat{U}_2(L,\omega) = B_1 - B_3e^{-\sqrt{2\Gamma}L} - B_4e^{\sqrt{2\Gamma}L} \tag{2.41}$$

Solving 2.40 and 2.41 we get,

$$\hat{U}_{\text{out}} = \frac{e^{-\sqrt{2\Gamma}L}\left(-\sqrt{2}(-1+e^{\sqrt{2\Gamma}2L}\right)\hat{I}_{\text{in}}\rho + (1+e^{\sqrt{2\Gamma}2L})H\Gamma\hat{U}_{\text{in}}W)}{2H\Gamma W} \tag{2.42}$$

Calculation of output parameters at known input parameters at length L of the sensor is given by a transfer matrix A:

$$\begin{Bmatrix} U_{\text{out}} \\ I_{\text{out}} \end{Bmatrix} = \begin{Bmatrix} A_{11} & A_{12} \\ A_{21} & A_{22} \end{Bmatrix} \begin{Bmatrix} U_{\text{in}} \\ I_{\text{in}} \end{Bmatrix} \tag{2.43}$$

Using equation 2.39 and 2.42, elements of matrix A are calculated:

$$A_{11} = \frac{1}{2}e^{-\sqrt{2\Gamma}L}(1+e^{\sqrt{2\Gamma}2L}) \tag{2.44}$$

$$A_{12} = \frac{-e^{-\sqrt{2\Gamma}L}(-1+e^{\sqrt{2\Gamma}2L})\rho}{\sqrt{2\Gamma}HW} \tag{2.45}$$

$$A_{21} = \frac{-e^{-\sqrt{2\Gamma}L}(-1+e^{2\sqrt{2\Gamma}L})\sqrt{\Gamma}HW)}{2\sqrt{2}\rho} \tag{2.46}$$

$$A_{22} = \frac{1}{2}e^{-\sqrt{2\Gamma}L}(1+e^{2\sqrt{2\Gamma}L} \tag{2.47}$$

$$A = \begin{Bmatrix} \frac{1}{2}(e^{-\sqrt{2\Gamma}L}(1+e^{\sqrt{2\Gamma}2L}) & \frac{-e^{-\sqrt{2\Gamma}L}(-1+e^{\sqrt{2\Gamma}2L})\rho}{\sqrt{2\Gamma}HW} \\ \frac{-e^{-\sqrt{2\Gamma}L}(-1+e^{2\sqrt{2\Gamma}L})\sqrt{\Gamma}HW)}{2\sqrt{2}\rho} & \frac{1}{2}e^{-\sqrt{2\Gamma}L}(1+e^{2\sqrt{2\Gamma}L}) \end{Bmatrix} \tag{2.48}$$

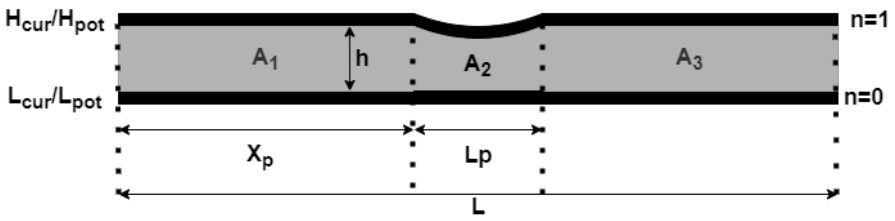

Figure 2.5: Definition of each section of the sensor

Figure 2.5 shows a parallel plate sensor of length L separated by a dielectric of height h (parameter 'd' is replaced by 'h'). When the sensor is pressed at a specific position, X_p, the pressed part L_p will have slightly different parameters then the unpressed part splitting the sensor into three sections. Each of these sections will have its own transformation/conduction matrix A, calculated using different parameters. The change in section A_2 is due to change in the dielectric thickness and the electrode's piezoresistivity. To predict the change in thickness the following equation is used [9]:

$$\Delta h = -\frac{F h_0}{A_0 E'} \tag{2.49}$$

Where Δh is the change in thickness, F is the applied compressive force, A_0 is the area of the electrodes and E' is the effective Young's modulus of the dielectric. The 3D printed dielectric is assumed to be compressible (poisson's ratio of zero) due to the ample amount of air present in it, hence change in the electrode area is neglected. The piezoresistivity of the electrode is modelled on a macroscopic level with the relative change in resistivity due to the applied force is calculated using the sensitivity factor S_n:

$$\frac{\Delta \rho}{\rho} = S_n F \tag{2.50}$$

Since the output of one section is connected to the input of another section, the A matrices can be multiplied. The final matrix used to calculate the conduction through different sections is given by:

$$A_{\text{final}} = A_3(L - X_p - L_p) A_2(L_p) A_1(X_p) \tag{2.51}$$

By applying the **third boundary** condition the impedance Z can be calculated:

$$I_{\text{out}} = A_{21} U_{\text{in}} + A_{22} I_{\text{in}} = 0 \tag{2.52}$$

And the definition of the impedance of the sensor as well as the A values from equation [26]:

$$\begin{aligned} Z_{\text{total}} &= \frac{\hat{U}_1(0,\omega) - \hat{U}_2(0,\omega)}{\hat{I}_1(0,\omega)} \\ &= -\frac{A_{22}}{A_{21}} \\ &= \frac{\sqrt{2}\rho(1 + e^{2\sqrt{2\Gamma}L})}{H\sqrt{\Gamma}W(-1 + e^{2\sqrt{2\Gamma}L})} \end{aligned} \tag{2.53}$$

The total impedance for resistance and capacitance in series is given by:

$$Z_{\text{total}}(\omega) = \Re\{Z(\omega)\} + \Im\{Z(\omega)\}\, j \tag{2.54}$$

Where $\Re\{Z(\omega)\}$, is the impedance of the resistance and $\Im\{Z(\omega)\}$ is the impedance of the capacitor.

$$Z_{\text{total}}(\omega) = R + \frac{1}{j2\pi f C} \tag{2.55}$$

2.4 MATLAB® Implementation

The model explained in section 2.3.1 has been implemented in MATLAB®. The parameters used to simulate the model of the 3 sensors are illustrated in table 2.1. Actual physical parameters of the fabricated sensors are used to obtain a more realistic change in impedance with respect to force and position. A frequency sweep is performed to predict the impedance spectrum. Next the impedance is calculated as a function of force and the position where the force is applied.

Table 2.1: Sensor parameters for modelling and simulation

Parameter name	SNJ	SX60	SESX60
Sensor length (L)	14 cm	14 cm	12 cm
Sensor width (W)	1 cm	1 cm	1 cm
L_{press}	0.8 cm	0.8 cm	0.8 cm
x_{press}	1 cm	1 cm	1 cm
Relative permittivity (ε_{r})	5.78	5.93	6.28
Dielectric height (h)	300 µm	300 µm	600 µm
Young's modulus (E')	12 MPa [27]	6 MPa [28]	6 MPa [28]
Resitivity of electrode (ρ)	0.25 Ω m	0.85 Ω m	0.98 Ω m
Frequency	1 kHz	1 kHz	1 kHz

2.4.1 Frequency behaviour

For the frequency response, Γ is the key parameter that determines the sensor's conduction. The conduction parameter is proportional to the frequency ($\Gamma \propto \omega$ and $\omega = 2\pi f C$). At lower frequency the impedance will be high and the capacitive reactance X_C will be larger than the resistance R, very little current flows through the sensor and response will be purely capacitive. Similarly, at a higher frequency, the resistive effects become dominant and the conduction is purely resistive. The change in the conduction mode is related to the cut-off frequency of f_{c}. For an RC low-pass filter circuit, the cut-off frequency (−3 dB) is when the resistance's magnitude is the same as the magnitude of capacitive reactance. The theoretical cut-off frequency of an RC filter is given by:

$$f_{\text{c}} = \frac{1}{2\pi RC} \tag{2.56}$$

When in this report a cut-off frequency is mentioned, the cut-off frequency of a RC filter with a capacitor and resistor equal to the series capacitance and series resistance of the transmission line is meant. A frequency sweep with six orders of magnitude from 10 Hz to 10 MHz is performed on the sensors. Figure 2.6 shows the relation between the series resistance and series capacitance as a function of frequency.

Since our sensor's lumped model is an RC low-pass filter, the sensor performs well until the frequency of 10 kHz. After the cut-off frequency, the path of the current changes, it does not longer go through the entire sensor, but only through the part closest to the connections. Since we want to measure on the entire sensor using a single frequency we will use a frequency lower than the cut-off frequency. Hence, all the simulations and measurements will be done at a frequency well below the cut-off frequency. The simulations for these sensor's impedance behaviour is done at an operating frequency of 1 kHz.

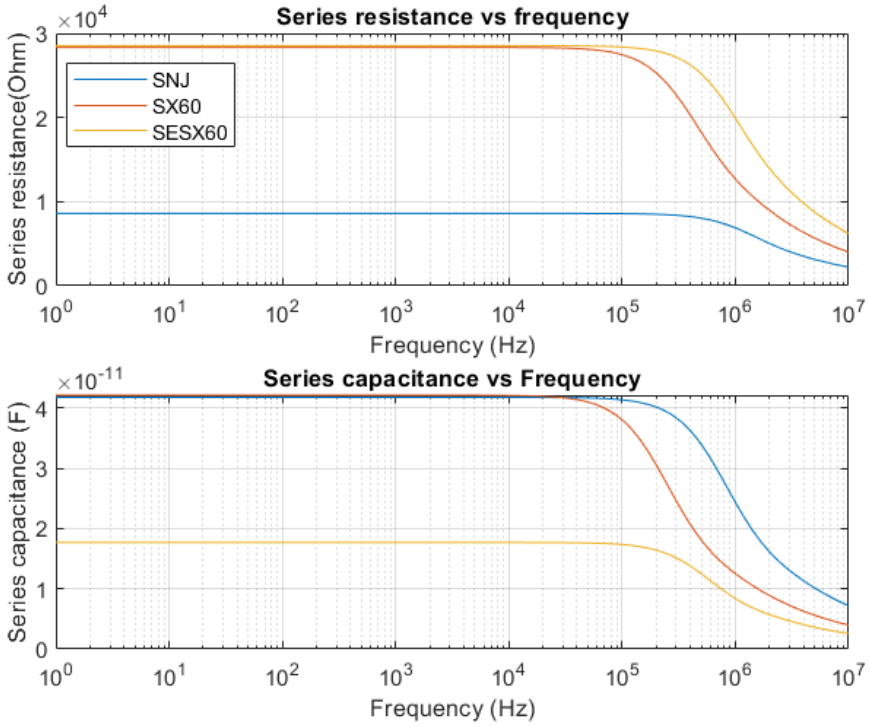

Figure 2.6: Impedance spectrum predicted by model for SNJ,SX60,SESX60

2.4.2 Impedance behaviour with respect to position and Force

This assignment aims to determine the applied vertical force and position where the force is applied using the real and imaginary impedance values at a single operating frequency. It is essential to know the sensor's impedance behaviour versus the position and force value. For simulation, a force of 3 to 11 N is applied on the sensor (at position x_{press}) and an operating frequency of 1 kHz. The changing parameters of the pressed part are calculated using equation 2.49 and 2.50. The impedance values are calculated as a function of position (x_{press}) and force (F) as shown in the figures below. The plots clearly show that the imaginary impedance depends only on force applied, and the real impedance depends both on the force and the position where the force is applied. The series capacitance is calculated from the imaginary impedance using the following equation:

$$C = -\frac{1}{2\pi f \Im\{Z(\omega)\}} \tag{2.57}$$

However, the change in the capacitance with changing force is less than 20 fF for all the three sensors, this is because for all three senors, a dielectric with 100 % infill ratio is assumed, increasing the effective youngs modulus [9] of the dielectric closer to that of the electrodes. The sensitivity of the sensor can be improved by printing the dielectric with lower infill percentage. The series resistance depends on the resistivity of the electrodes. Figure 2.7,2.8 and 2.9 show the change in impedance as a function of magnitude and position of an applied force.

Parallel Plate capacitive sensor with NinjaFlex dielectric (SNJ)

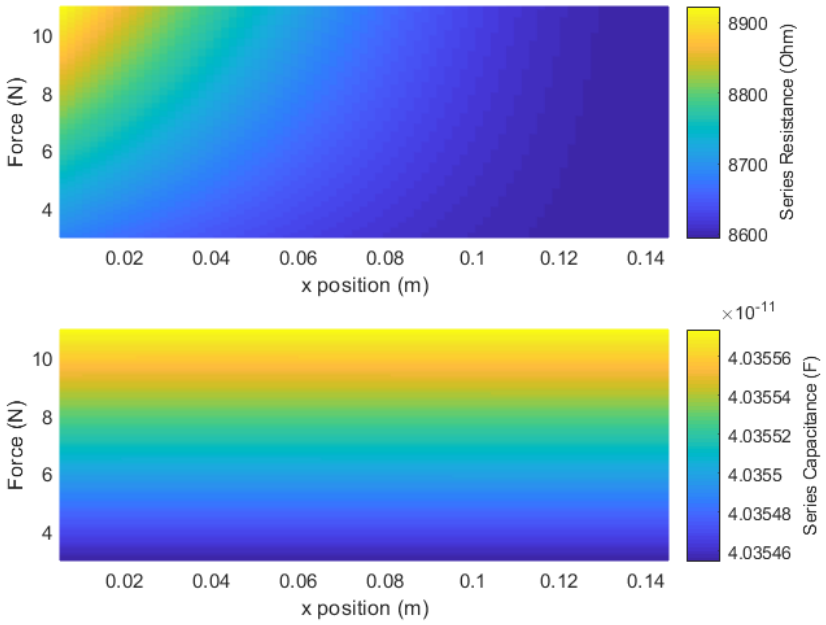

Figure 2.7: Impedance predicted by the model for Ninjaflex dielectric

Parallel Plate capacitive sensor with X60 dielectric (SX60)

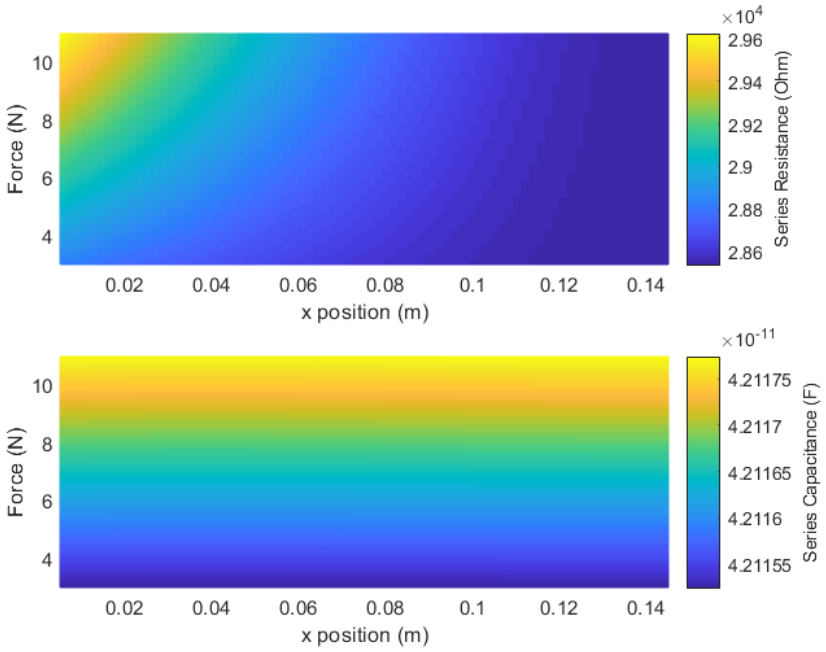

Figure 2.8: Impedance predicted by the model for X60 dielectric

Same size Parallel plate capacitive sensor with X60 dielectric (SESX60)

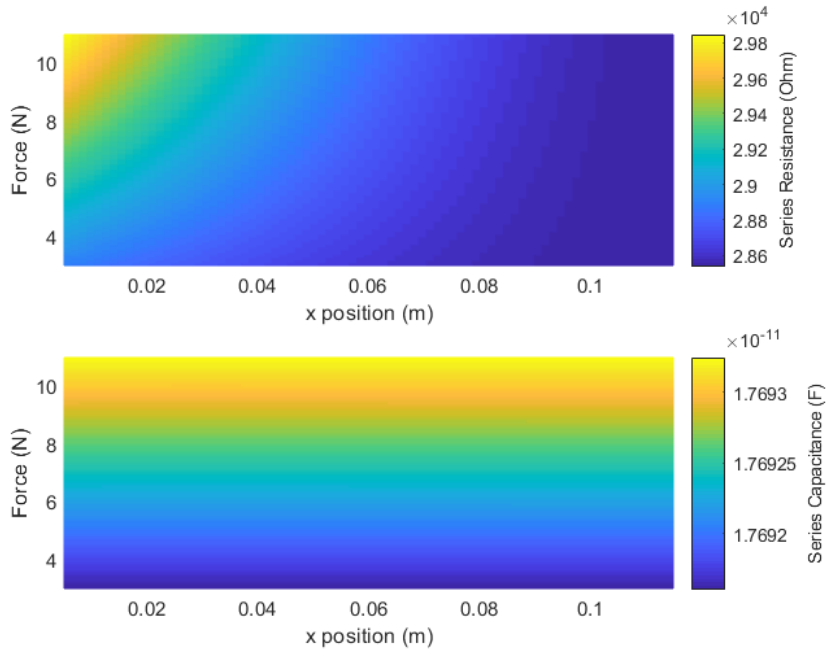

Figure 2.9: Impedance spectrum predicted by the model for the same size electrodes with X60 dielectric

2.5 Differential force sensor

The three sensors discussed in the previous section were tested, section 4.3 explains the experiments performed to characterize the change in impedance as a function of the magnitude and position of the applied force. The sensors did not work as predicted by the model; chapter 5 discusses each sensor's results. Hence, a different approach was utilized by designing and fabricating a differential sensor. In this approach, two parallel plates capacitive sensors are stacked, one top of the other, as shown in 2.10 hence, the sensor can be seen as a combination of two coupled lossy transmission lines. The operating principle is still the same as for previous sensor.

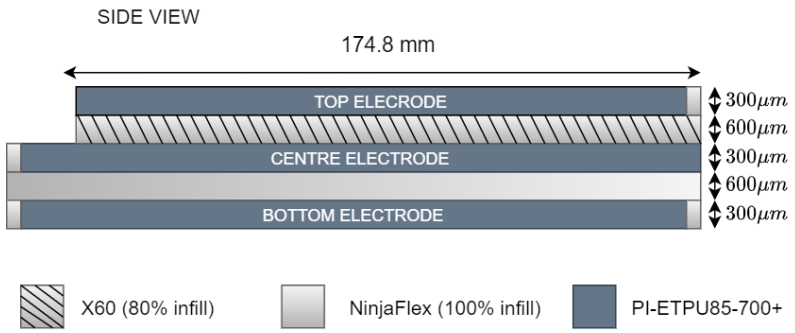

Figure 2.10: Schematic diagram of the differential sensor with X60 dielectric

2.5.1 Model calculation

The derivation is adapted from appendix A. Figure 2.11 shows the equivalent circuit diagram of an infinitesimal Δx part of the two coupled lossy transmission lines. Kirchhoff's voltage law applied to the circuit yields:

$$U_n(x) - R_n \Delta x I_n(x) - U_n(x + \Delta x) = 0 \tag{2.58}$$

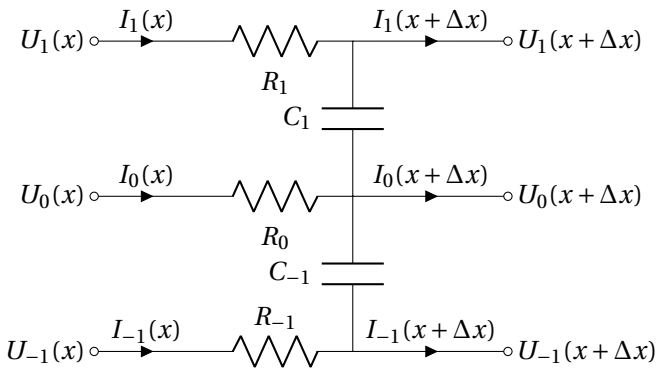

Figure 2.11: Electrical circuit diagram of an infinitely small part of the sensor. Image courtesy of appendix A

and applied Kirchhoff's current law yields:

$$I_n(x) - G_n \Delta x (U_n(x+\Delta x) - U_{n-1}(x+\Delta x)) - I_n(x+\Delta x) = 0 \tag{2.59}$$

Dividing 2.58 and 2.59 by Δx and taking the limit as $\Delta x \to 0$ yields the following differential equations:

$$\frac{\partial U_n(x)}{\partial x} = -R_n I_n \tag{2.60}$$

$$R_n = \frac{\rho_n}{h_{n,e} W} \tag{2.61}$$

where R is the resistance per meter length of the electrode, ρ_n is the resistivity of the electrode, $h_{n,e}$ is the height of the electrode and W is the width of the electrode.

$$\frac{\partial I_n(x)}{\partial x} = G_n(U_{n-1}(x) - U_n(x)) \tag{2.62}$$

$$G_n = j\omega C_n = \frac{j\omega \varepsilon_n \varepsilon_0 W}{h_{n,d}} \tag{2.63}$$

where G_n is the admittance per meter length of the dielectric, ε_0 is the relative permittivity of vacuum, ε_n is the relative permittivity of the dielectric and $h_{n,d}$ is the height of the dielectric. The relation between the conduction parameter Γ from equation 2.17 in the previous derivation and G_n is:

$$\Gamma = G_n R_n = \frac{j\omega \varepsilon_0 \varepsilon_n \rho_n}{h_{n,d} h_{n,e}} \tag{2.64}$$

The current equations for all the electrodes are given by:

$$\frac{\partial I_1(x)}{\partial x} = G_1(U_0(x) - U_1(x)) \tag{2.65}$$

$$\frac{\partial I_0(x)}{\partial x} = G_1(U_1(x) - U_0(x)) + G_{-1}(U_{-1}(x) - U_0(x)) \tag{2.66}$$

$$\frac{\partial I_{-1}(x)}{\partial x} = G_{-1}(U_0(x) - U_{-1}(x)) \tag{2.67}$$

The first order differential equations are easier to solve compared to second order differential equations. The set of equations can be written into matrix form:

$$\frac{\partial \vec{P}}{\partial x} = A\vec{P} \tag{2.68}$$

$$P = \begin{Bmatrix} U_1 \\ I_1 \\ U_0 \\ I_0 \\ U_{-1} \\ I_{-1} \end{Bmatrix}, \; A = \begin{Bmatrix} 0 & -Z_1 & 0 & 0 & 0 & 0 \\ -G_1 & 0 & G_1 & 0 & 0 & 0 \\ 0 & 0 & 0 & -Z_0 & 0 & 0 \\ G_1 & 0 & -G_1 - G_{-1} & 0 & G_{-1} & 0 \\ 0 & 0 & 0 & 0 & 0 & -Z_{-1} \\ 0 & 0 & G_{-1} & 0 & -G_{-1} & 0 \end{Bmatrix} \tag{2.69}$$

The solution of these equations can be found from the exponential functions based on eigen values and eigen vectors and is given by:

$$\overrightarrow{P} = \overrightarrow{C}\, Y(x) \tag{2.70}$$

where Y(x) is a matrix formed by six eigen vectors $\overrightarrow{\eta}_n$ and eigen values λ_n:

$$Y(x) = \left\{ \overrightarrow{\eta}_1 e^{\lambda_1 x} \quad \overrightarrow{\eta}_2 e^{\lambda_2 x} \quad \overrightarrow{\eta}_3 e^{\lambda_3 x} \quad \overrightarrow{\eta}_4 e^{\lambda_4 x} \quad \overrightarrow{\eta}_5 e^{\lambda_5 x} \quad \overrightarrow{\eta}_6 e^{\lambda_6 x} \right\} \tag{2.71}$$

The coefficients in vector $\overrightarrow{C}$ can be calculated by the boundary conditions as before. For a known $\overrightarrow{P}(x)$, at certain position x, $\overrightarrow{C}$ can be calculated using:

$$\overrightarrow{C} = Y^{-1}(x)\overrightarrow{P}(x) \tag{2.72}$$

If the input parameters are known then the output parameters at length L are given by transformation matrix N (similar to A in the previous derivation)

$$\overrightarrow{P}(L) = N(L)\overrightarrow{P}(0) \tag{2.73}$$

and $N(L)$ given by:

$$N(L) = Y(L)Y^{-1}(0) \tag{2.74}$$

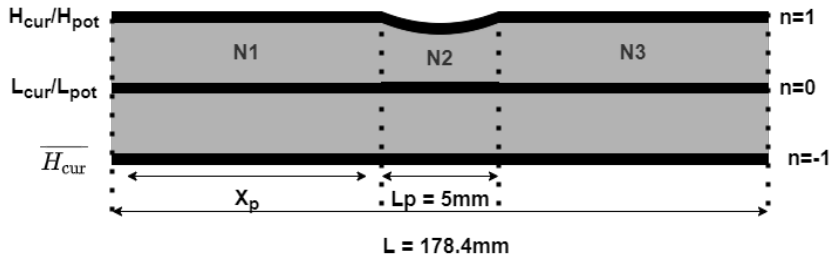

Figure 2.12: Definition of each section of the sensor

Figure 2.12 shows the differential sensor of length L with a dielectric of height $H_{n,d}$. When the sensor is pressed at a specific position X_p, the pressed part L_p will have slightly different parameters than at the unpressed parts. In the analysis the sensor is split into three parts. Each of these sections will have their own transfer matrix N, calculated using different parameters. The change in the section N_2 is due to the change in the dielectric thickness and the electrode's piezoresitivity. The change in thickness is predicted using the equation 2.49. Both the dielectrics are assumed to be compressible due to the large amount of air present (poisson's ratio of zero) and the change in the area of the dielectrics is neglected. The relative change in the resistivity is calculated using equation 2.50. The final matrix used to calculate the propagation is given by:

$$N_{\text{final}}(L) = N_3\left(L - X_\mathrm{p} - \frac{1}{2}L_\mathrm{p}\right) N\left(l_\mathrm{p}\right) N_1\left(X_\mathrm{p} - \frac{1}{2}L_\mathrm{p}\right) \tag{2.75}$$

The sensor is applied with similar boundary conditions as before and masking matrices M_U and M_I are used to mask out the current and voltage rows resulting in the following boundary condition equations:

$$M_U \overrightarrow{P}(0) + M_I \overrightarrow{P}(L) = \overrightarrow{B} \tag{2.76}$$

with:

$$M_U = \begin{Bmatrix} 1 & 0 & 0 & 0 & 0 & 0 \\ 0 & 0 & 0 & 0 & 0 & 0 \\ 0 & 0 & 1 & 0 & 0 & 0 \\ 0 & 0 & 0 & 0 & 0 & 0 \\ 0 & 0 & 0 & 0 & 1 & 0 \\ 0 & 0 & 0 & 0 & 0 & 0 \end{Bmatrix}, M_I = \begin{Bmatrix} 0 & 0 & 0 & 0 & 0 & 0 \\ 0 & 1 & 0 & 0 & 0 & 0 \\ 0 & 0 & 0 & 0 & 0 & 0 \\ 0 & 0 & 0 & 1 & 0 & 0 \\ 0 & 0 & 0 & 0 & 0 & 0 \\ 0 & 0 & 0 & 0 & 0 & 1 \end{Bmatrix}, \overrightarrow{B} = \begin{Bmatrix} U_1(0) \\ I_1(L) \\ U_0(0) \\ I_0(L) \\ U_{-1}(0) \\ I_{-1}(L) \end{Bmatrix} \tag{2.77}$$

Using these boundary conditions and equation 2.73 and 2.75 the current going through each electrode can be calculated using:

$$\overrightarrow{P}(0) = (M_U + M_I N_{\text{final}})^{-1} \overrightarrow{B} \tag{2.78}$$

The impedance Z is given by:

$$Z = -\frac{U_1(0) - U_0(0)}{I_0(0)} \tag{2.79}$$

2.5.2 MATLAB® Implementation

The model is implemented in MATLAB®. The parameters used to simulate the model of the two sensors are illustrated in table 2.2. Actual physical parameters of the fabricated sensors are used to obtain a more realistic change in impedance with respect to force and position. Next the impedance is calculated as a function of force and the position where the force is applied.

Table 2.2: Sensor parameters for modelling and simulation

Parameter name	DSNJX60	DSX60INF
Sensor length (L)	17.8 cm	17.8 cm
Sensor width (W)	0.84 cm	0.84 cm
L_{press}	1 cm	1 cm
x_{press}	5 cm	5 cm
Relative permittivity top dielectric (ε_1)	6.33	4.66
Relative permittivity bottom dielectric (ε_{-1})	4.89	6.54
Dielectric height (h)	600 µm	600 µm
Young's modulus top dielectric (E'_1)	1 MPa	1 MPa [28]
Young's modulus bottom dielectric (E'_{-1})	12 MPa [27]	6 MPa [28]
Resitivity of top electrode (ρ_1)	0.07 Ω m	0.15 Ω m
Resitivity of center electrode (ρ_0)	0.2 Ω m	0.93 Ω m
Resitivity of top electrode (ρ_{-1})	0.072 Ω m	0.04 Ω m
Frequency	3 kHz	3 kHz

2.5.3 Frequency response

A frequency sweep with six orders of magnitude from 1 kHz to 1 MHz performed on the sensors. Figure 2.13 shows the relation between the series resistance and series capacitance as a function of frequency. The lumped model of the differential sensor is and RC-low-pass filter. The sensor performs well at low frequency. After the cut-off frequency the path of current changes and it no longer go through the entire sensor, but only through the part closest to the connections. Hence, the simulations and measurements will be done below cut-off frequency. Similar to the parallel plate sensor the admittance G_n determines the conduction in the sensor.

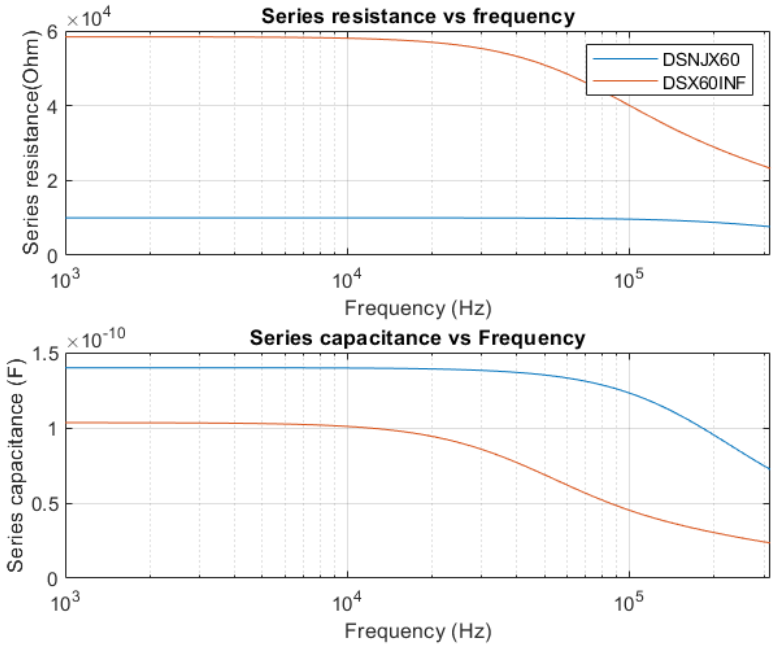

Figure 2.13: Impedance spectrum predicted by model for DSNJX60 and DSX60INF

2.5.4 Force excitation

The sensor is simulated with the same configuration as described in section 2.4.2 except with an operating frequency of 3 kHz. Figure 2.14 and 2.15 show that the series capacitance is only dependent on the force, but the series resistance is dependent on both the position and the force. The change in the capacitance for both sensors is 800 fF.

Sensor DSNJX60

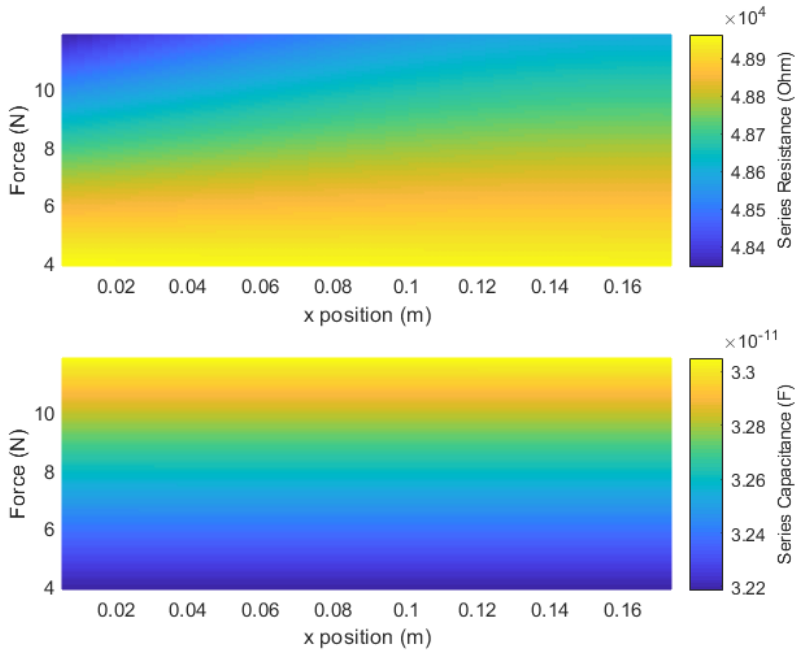

Figure 2.14: Differential Impedance against force and position predicted by model for DSNJX60

Sensor DSX60INF

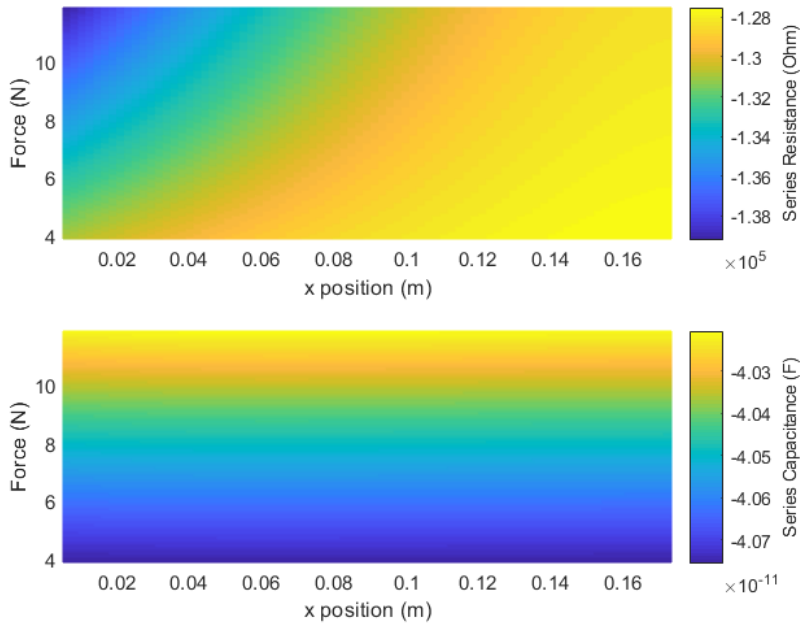

Figure 2.15: Differential Impedance against force and position predicted by model for DSX60INF using equation 2.79

2.6 Inverse Model

The MATLAB® implementation of the analytical model calculates the change in impedance at a known force and position but the goal of the assignment is to determine the force and position from the impedance. The model discussed in this section estimates the force and position values from the impedance values. Sensor SESX60 is used for implementation of the inverse model.

2.6.1 Estimation using $fmincon$

The model utilized simple equations to estimate the change in resistance and capacitance. In this simple model the relation between force and capacitance is approximated by a linear equation. It is also assumed that the resistance is linearly dependent on the force. However the relation between resistance and position is approximated by a quadratic equation. First an initial estimation is done where the resistance and capacitance values are estimated, along with the change in resistance and capacitance due to force and position. These initial estimated parameters are listed below:

- Estimated resistance, R_0
- Estimated capacitance, C_0
- change in capacitance due to applied force, C_F
- change in resistance due to applied force, A
- quadratic term of the position, B
- change in resistance due to change in position, D
- change in resistance due to force and position, E

The parameters are multiplied by weight vector w_0 to determine the coefficients of the equations. The w_0 is a vector of ones, $w_0 = [1,1,1,1,1,1,1]$. The change in capacitance is calculated by:

$$C = C_0 + FC_{\mathrm{F}} \tag{2.80}$$

The change in resistance is calculated by:

$$R = R_0 + AF + Bx^2 + Dx + EFx \tag{2.81}$$

where F is the force applied and x is the position where the force is applied. The real impedance $\Re\{Z(\omega)\}$ and imaginary impedance $\Im\{Z(\omega)\}$ are calculated from the resistance and the capacitance, using that they are in series.

A cost function is defined which is the root mean square of the summation of the squared difference between the model impedance and the estimated impedance:

$$J = \sqrt{\frac{1}{m}\sum_{i=1}^{m}\left(\Re\{Z_{\mathrm{M}}\} - \Re\{Z_{\mathrm{est}}\}\right)^2} + \sqrt{\frac{1}{m}\sum_{i=1}^{m}\left(\Im\{Z_{\mathrm{M}}\} - \Im\{Z_{\mathrm{est}}\}\right)^2} \tag{2.82}$$

The MATLAB® function *fmincon* is used to minimize the error of this cost function by finding the optimal coefficients given by $w_{\mathrm{fit}} = [0.18, 0.28, 0.11, 0.23, 0, 2.96, 0.29]$. The impedance is calculated using w_{fit} vector and the result is shown in figure 2.16.

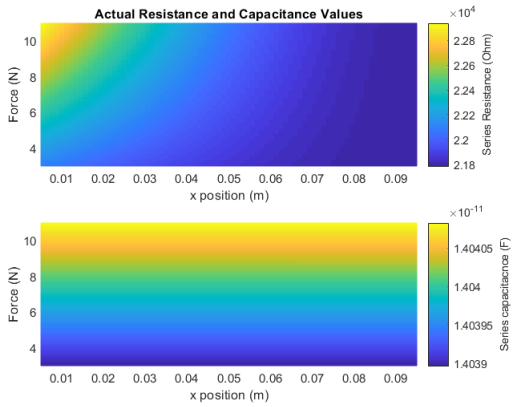

(a) Series resistance vs force and position

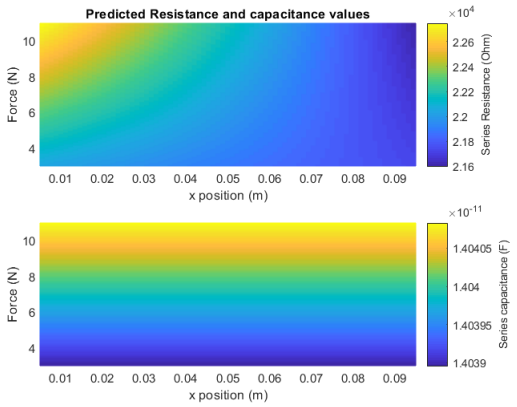

(b) Series resistance vs force and position

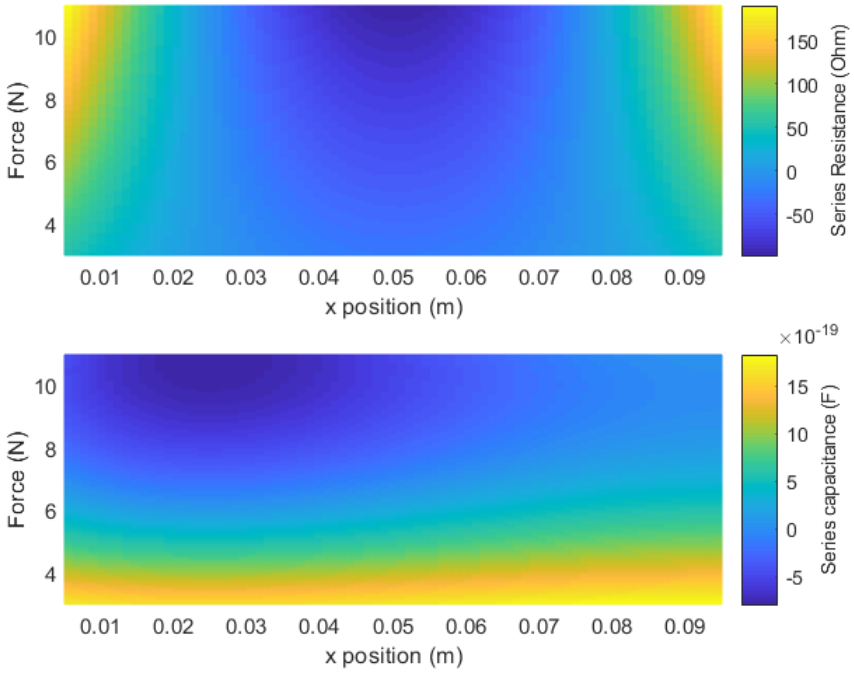

(c) Series resistance vs force and position

Figure 2.16: (a) Impedance value calculated based on the analytical model (b)Impedance value after fitting the simplified model using $fmincon$ to a. (c) The difference between the model data and the estimated data. The difference is less and the estimated model fits quite well)

Now to determine position and force from the impedance an inverse function is implemented in MATLAB® by inverting equation 2.81 and 2.80. The applied force F is calculated using:

$$F = \frac{C - C_0}{C_F} \tag{2.83}$$

and the change in position x is calculated by solving the quadratic formula $\frac{-b-\sqrt{b^2-4ac}}{2a}$, however this formula did give values that were outside of the sensor and those values were neglected:

$$x = \frac{-(D+EF) - \sqrt{-(D+EF)^2 - 4B(R_0+AF)}}{2B} \tag{2.84}$$

The function takes impedance, the initial estimated parameter and optimized weights as an input and gives the corresponding force and position as output. Figure 2.17 shows force as

a function of $\Re\{Z(\omega)\}$ and $\Im\{Z(\omega)\}$. It is clear from the plot second plot that the force value of 3-11 N is given by the $\Im\{Z(\omega)\}$. Similarly, the $\Re\{Z(\omega)\}$ gives the position information, the calculated position is in the range of 0.01-0.09 m which is the actual length of the sensor.

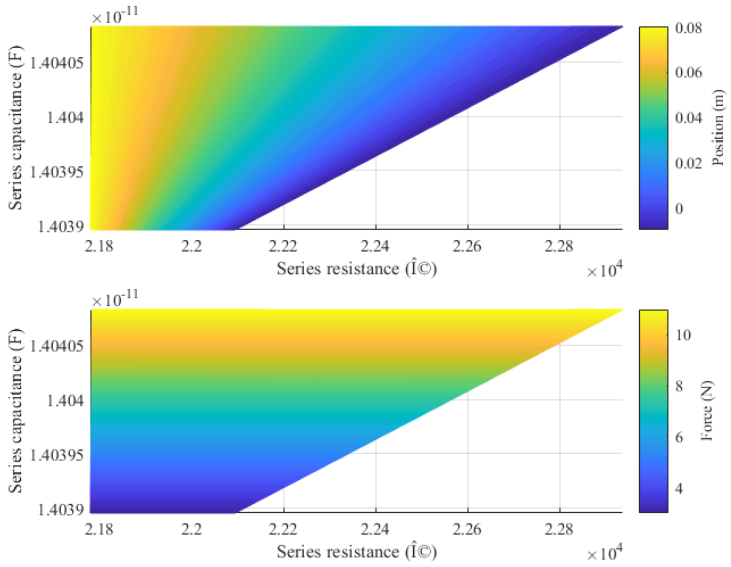

Figure 2.17: Force and position calculated from the impedance by the inverse model (SESX60)

2.7 Conclusions

- From the literature survey a model by Xu et. al was selected which models the capacitive sensor as a lossy transmission line.
- The parallel plate and differential sensor's electrical characteristics are analytically modelled using the partial differential equations of the voltage and current along the transmission line.
- The differential equations are solved using the eigenvalue expansion and their corresponding eigenvectors with the coefficients determined by the boundary conditions.
- The analytical model of the sensors is then implemented in the MATLAB® and the impedance has been calculated as a function of magnitude and position of an applied force.
- The 3D plot results showed that the imaginary impedance is only dependent on the force and real impedance is force and position dependent.
- Since, the senors' lumped model is an RC low-pass filter, the sensor behaviour is different at high frequencies and this behaviour only holds up till a frequency of 100 kHz.
- To determine the force and position from the impedance, an inverse model is implemented in the MATLAB®
- The inverse model works for the model data.

The next chapter discusses the fabrication design and fabrication process of the proposed sensors.

3 Materials and Fabrication

3.1 Introduction

This chapter aims to explain the materials used to fabricate the sensors, explain the 3D printing process, and the effect of the printing parameters on the electrical properties of the material used. Finally, the design and fabrication of the five sensors are illustrated.

3.2 Materials

The sensor is fabricated using two materials; the dielectric is made of Thermoplastic polyurethane (TPU) and the conductive electrodes are made using an electrically conductive variant of TPU (eTPU). The following section explains both materials in detail.

3.2.1 Flexible Conductive material

Conductive polymer composites filled with conductive fillers such as Carbon Black (CB) show piezoresistivity and have been studied extensively for smart sensing applications. The main advantages include great flexibility, low weight, high environmental stability, low density and low manufacturing cost [1, 29]. CB is an amorphous form of carbon produced from the incomplete combustion of petroleum products. Hence, it is inexpensive and has good availability [25]. When adding CB as a conductive filler to an insulating elastomer, the volume resistivity of the material decreases strongly up to a critical concentration of CB. The phenomenon of the forming of conductive networks is called percolation [30]. During the initial loading, the polymer is insulating because there are to few CB nanoparticles in the polymer matrix, due to which they cannot form conductive pathways through the polymer. However, on increasing the CB particle density to the percolation threshold long-range networks are formed causing a sharp decline in the electrical resistivity. Beyond this threshold, the resistivity further decreases slowly, as there are more and more particles in the polymer matrix to contribute to the conductive network. The electrical percolation depends on the nature and the aspect ratio of the filler particles [1,30].

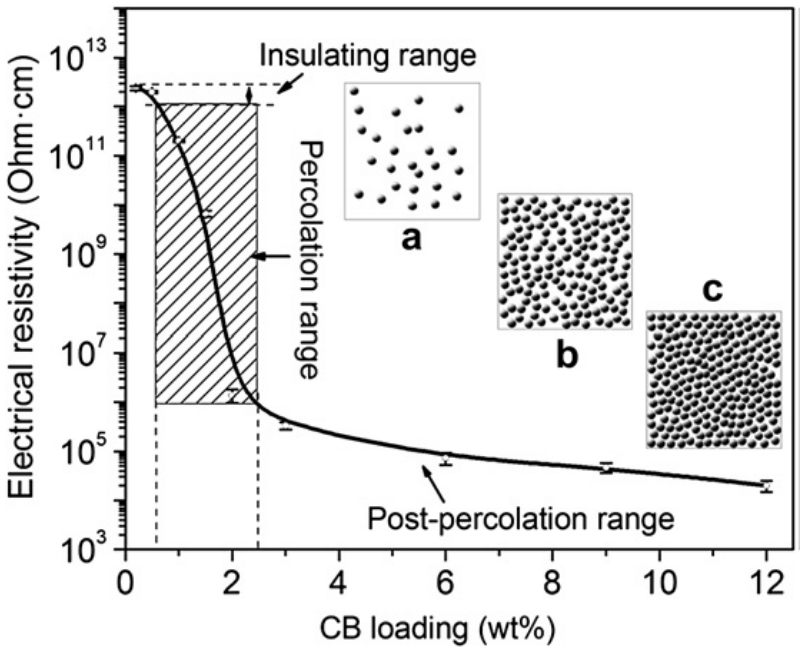

Figure 3.1: Relationship between resistivity and CB loading. The insets (a) insulating range, (b) percolation range/threshold, (c) post-percolation range [1]

Previously it was thought that the conduction in the carbon-based networks was due to percolation of electrically connected particles; new research shows that the conduction is further aided by quantum-mechanical junction tunneling [31]. It is a phenomenon in which a higher applied electric field excites the electron to jump through the potential barrier [32]. CPCs are often thermoplastic and therefore can be used in FDM 3D printing. The available materials in the market right now are protopasta [33], PI-eTPU 85-700+ [34] and EEL [35]. These materials are studied and compared by Watschke et al. [36]. PI-eTPU 85-700+ will be used in this assignment because of its flexibility and low resistivity. PI-eTPU 85-700+ has been studied before by Schouten, and he found in his measurements an electrical resistivity of 7.43 Ω m and relative permittivity of 176 [28]. The material is used to fabricate various sensors; some of them include a whisker inspired 3D printed flexible tactile sensor, capacitive force sensor, and flexible soft and flexible sEMG electrodes [9, 37–39].

PI-eTPU85-700+

This flexible and conductive filament was sourced from Palmiga innovations. The material consists of TPU filled with carbon black. The shore hardness as reported by the manufacture is 85 A and the maximum extension is more than 700 %. Table-3.1 shows the mechanical and electrical properties of the material.

3.2.2 Dielectric

The dielectric is the compressive material between the two electrodes and will influence the change in the capacitance of the sensor and hence, sensitivity of the sensor. The two available dielectric materials for the sensors are NinjaFlex and X60.

NinjaFlex

It is a flexible TPU filament made by NinjaTek [27] and was the first choice as a dielectric material as it has the same shore hardness and Young's modulus as eTPU and it also is relatively easy to print. The similar mechanical properties will lead to the same elastic deformation. Table-3.1 shows the mechanical properties of the material.

X60 dielectric

X60 is a flexible TPU filament made by the collaboration between Diabase Engineering and MakeShaper [40]. It is one of the softest filaments available in the market and has a shore hardness of 60 A, softer than Ninjaflex. Table 3.1 shows the mechanical properties of the material.

Table 3.1: Mechanical properties of the materials used to design the sensor

Mechanical Properties	PI-eTPU 85-700+ [34]	NinjaFlex [41]	X60 [42]
Tensile Strength	15 MPa	4 MPa	35 MPa
Tensile Modulus	12 MPa	12 MPa	6 MPa
Elongation at break	700 %	660 %	1000 %
Hardness	85 Shore A	85 Shore A	63 Shore A
Printing Temperature	210 °C	216 °C	220 °C

3.3 Fabrication

3.3.1 3D Printer

The Diabase H series 3D printer from Diabase Engineering is used to 3D print the sensors for this assignment. It has 5 extruders with automatic tool changer and allows printing 5 different materials in the same print. The printer comes with its own extruder called flexion extruder [43] which offers high speed printing of ultra flexible filament materials (X60). The extruder has

a self cleaning brush which cleans the drive roller and keeps the teeth sharp for consistent extruding. The printer uses a cam dial and cam follower screw to compress the filament to apply tension on the filament. The cam dial has 4 settings for printing different materials. The printer has an enclosure to prevent contamination of prints.

3D Printing process

The 3D printing process includes the following steps to build a 3D object [44]:

- **Pre-processing:** Generate a 3D model of the object using computer-assisted design (CAD) software. The CAD model is then converted to an STL file to tesselate the 3D shape and slice it into digital layers. The STL file is then sliced into machine-readable G-code using dedicated software that calculates the path to extrude thermoplastic and support materials.
- **Fabrication:** This step includes loading the printer with filaments. The printer prints the 3D model by depositing material traxel by traxel and layer by layer. The printed part is then removed from the build platform with its support structure.
- **Post-processing:** This includes the removal of the support material and cleaning the part.

3.3.2 Printing Parameters

The printing parameters are essential to give the desired characteristics to the sensor. Every parameter affects both the mechanical and electrical properties of the sensor. The parameters selected for the sensor are discussed and justified below:

Infill

Since FDM 3D printers print the object line by line and layer by layer, the 3D part has two aspects, the exterior walls and the material inside this wall to fill the object, called infill. The infill has two important parameters: the infill density and the infill pattern. Both play a considerable role in the printed object's mechanical and electrical properties. The infill density determines the amount of material inside the part, usually defined as a percentage from 0 to 100. The part having a lower infill density is hollow and compressible. A decrease in infill reduces Young's modulus and affects the print time and material consumption. The commonly available infill patterns are rectilinear, lines, honeycomb, triangular and concentric [45]. Since eTPU is the flexible conductive filament, the electrodes have 100 % infill to reduce the resistance and improve the conductivity of the electrodes because flexibility is not the issue. The dielectric is the compressible layer between the electrodes and sensors with different infill percentage are tested. The infill density of the dielectric affects the capacitive sensing of the sensor (refer to section 5.6). The default rectilinear infill pattern is used to print of both materials.

Temperature

The two temperature parameters are: nozzle temperature and build plate/bed temperature. The TPU filament is melted at elevated temperature in the heater just above the nozzle and cools down on the build platform. A higher heater temperature causes the material to ooze and causes printing inconsistency, which affects the sensor's conductivity and mechanical properties. Hence, print temperatures, as recommended in the datasheet, were chosen to print the sensors. The bed temperature should be high enough to have proper adhesion between the layers. The bed temperature for sensors SNJ, SX60, SESX60 was 60 °C and for DSNJX60 and DSX60INF was 75 °C.

Line width/Extrusion Multiplier

The extruder extrudes the filament in thin lines. The width of the line depends on the nozzle diameter and extrusion multiplier. The amount of material extruding per unit length through the extruder at a given speed is regulated by the extrusion multiplier parameter. It changes the cross-section of the extruded filament and influences all layers and fillings of the print. The default multiplier value is 1. If set above 1 it allows to print dense parts, but a too high value can cause material overflow resulting in inconsistent prints with lower dimensional accuracy. If it is < 1 the resulting print uses less filament, affecting the tensile strength of the print [45].

3.4 Post-processing

CPCs can show a pyroresistive behaviour due to which the electrical resistivity can increase with the temperature also known as positive temperature coefficient (PTC) effect, or a decrease in electrical resistivity called negative temperature coefficient (NTC) effect [46]. The PTC effect is due to the polymer matrix's large thermal expansion coefficient below its melting point. The NTC effect is due to the decrease in elastic modulus of the polymer matrix at high temperatures by reducing the distance between the CB particles and reforming the conductive pathways [47]. However, these are general explanations with certain assumptions. Other theories of the effects include tunneling current mechanism, congregation and migration changes of filler particles, electric field mechanism, internal stress mechanism and percolation theory [48]. Although the interpretation is still unclear, the effects are there.

Lee et al. discussed the effect of annealing on the electrical resistivity of the FDM printed 3D sensors. The experimental results showed that the electrical conductivity was affected by the residual stress. The three causes for residual stress are: 1) once the molten polymer is extruded at high temperature, solidification occurs due to rapid cooling at room temperature before polymer stabilisation. 2) Shear flow occurs due to friction and cooling at the nozzle wall due to lower extrusion speed relative to the nozzle centre, which is not affected by the shear. 3) differential stress due to polymer orientation. The other factors influencing the conductivity include defects in the micro-structure such as impurity, precipitation and dislocation. The annealing improved the sensor's electrical conductivity by enabling polymer chains, eliminating dislocation, crystallisation which induces grain refinement and grain boundary growth, and thus reducing the residual stress of the sensor. [49, 50].

To improve the conductivity of the electrodes, all sensors fabricated in this assignment were annealed in the oven at 150 °C for 24 h. The sensors were slightly curved along the x and y axes. The resistance was measured using a multi-meter before and after the annealing process. The results showed decrease in the electrical resistance of the electrodes for all the sensors.

3.5 Sensor with NinjaFlex dielectric (SNJ)

The parallel plate flexible sensor was the first prototype printed based on the analytical model. The sensor CAD file was designed in Autodesk Fusion 360 and sliced with Simplify 3D software. NinjaFlex was used as a dielectric sandwiched between two PI-ETPU 85-700+ 3D printed electrodes with the dimensions as shown in figure 3.2 and using the printing parameters as shown in table 3.2. The actual picture of the sensor can be found in figure 3.3. The top electrode was designed smaller than the bottom electrode and the dielectric to avoid a short between the two at the sensor's edge as the dielectric is very thin. However, the sensor was not able to produce reasonable results as discussed in section 5.2

Table 3.2: Print settings for SNJ

Printing parameter	PI-EPTU 85-700+	NinjaFlex
Layer height	50 µm	50 µm
Infill	100 %	100 %
Print Temperature	210 °C	220 °C
Nozzle Diameter	0.4 mm	0.4 mm
Extrusion width multiplier	1.1	1.2
Extrusion width	0.44	0.48
Cam dial settings	3	2

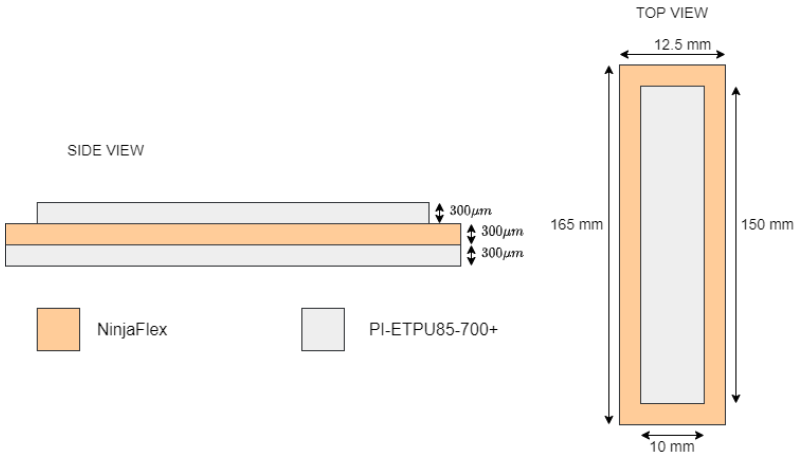

Figure 3.2: Schematic diagram of the sensor with NinjaFlex dielectric

Figure 3.3: Picture of the sensor with NinjaFlex dielectric

3.6 Sensor with X60 dielectric (SX60)

The flexible sensor was the second prototype printed on the same analytical model. The sensor was designed and sliced with the same software as before. The only modification was the use of X60 as the dielectric as it is more flexible than NinjaFlex. The sensor was designed using the same dimensions as shown in figure 3.4 using the printing parameters shown in table 3.3. The actual picture of the sensor can be found in figure 3.5. The sensor was fabricated to compare the performance with SNJ and check if there was a measurable signal with a more flexible dielectric and, therefore a larger capacitance change for the same force. However, the sensor could not produce reasonable results, as discussed in section 5.3.

Table 3.3: Print settings for SX60

Printing parameter	PI-EPTU 85-700+	X60
Layer height	50 µm	50 µm
Infill	100 %	100 %
Print Temperature	210 °C	230 °C
Nozzle Diameter	0.4 mm	0.4 mm
Extrusion width multiplier	1.1	1.25
Extrusion width	0.44 mm	0.48 mm
Cam dial settings	3	1

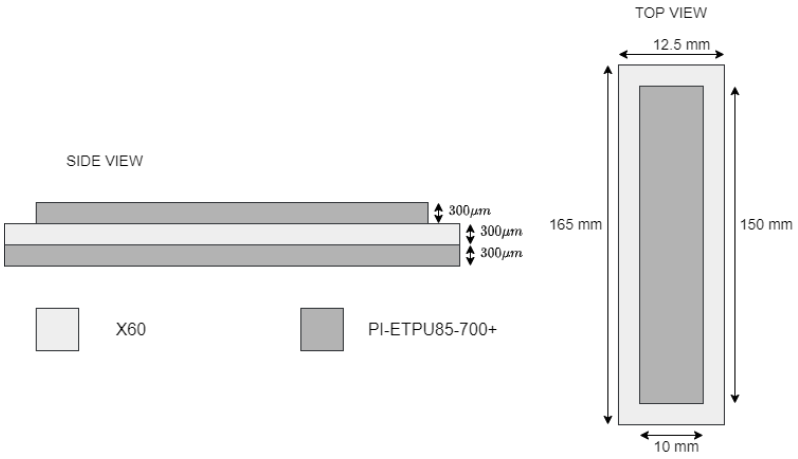

Figure 3.4: Schematic diagram of the sensor with X60 dielectric

Figure 3.5: Picture of the sensor with X60 dielectric

3.7 Sensor with same electrode size (SESX60)

The flexible sensor was the third and the last prototype printed on the same analytical model. The sensor was designed and sliced using the same software as before. There were two design modifications: 1) the top and bottom electrodes now had same length. 2) the dielectric thickness was doubled to 600 µm encapsulating the bottom electrode from two ends as shown in figure 3.6. Table 3.4 shows the printing parameters. The second modification was to avoid short between top and bottom electrode and increasing the dielectric thickness decreases the capacitance and increases the cut-off frequency. The actual picture of the sensor can be found in figure 3.7. The sensor performance is compared with previous two prototypes in section 5.4.

Table 3.4: Print settings for SESX60

Printing parameter	PI-EPTU 85-700+	X60
Layer height	50 µm	50 µm
Infill	100 %	100 %
Print Temperature	210 °C	230 °C
Nozzle Diameter	0.4 mm	0.4 mm
Extrusion width multiplier	1.2	1.25
Extrusion width	0.44	0.5
Cam dial settings	3	1

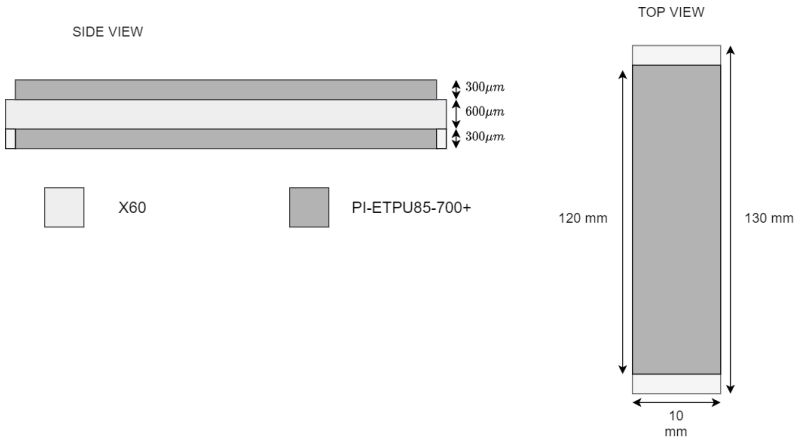

Figure 3.6: Schematic diagram of the sensor with same electrode size and X60 dielectric

Figure 3.7: Picture of the sensor with same electrode size and X60 dielectric

3.8 Differential Sensor with NinjaFlex and X60 dielectric (DSNJX60)

The fourth flexible sensor prototype was printed based on the differential analytical model. The sensor CAD file was designed in Autodesk inventor and sliced using open-source Cura 4.7.1 slicing software with custom post-processing script [51]. Two parallel plate sensors were stacked together with one on top of the other, making five layers. The centre and bottom electrode with NinjaFlex dielectric formed one sensor. The centre and top electrode with X60 dielectric formed the second sensor, the centre electrode being the common electrode between two sensors. NinjaFlex was used to print the bottom dielectric, and X60 with an infill of 80 % was used to print the top dielectric. The dielectric was printed with a lower infill percentage to improve the compressibility and sensitivity of the sensor. The NinjaFlex dielectric encapsulated the bottom electrode from two ends and the centre electrode from one end. The X60 dielectric encapsulated the top electrode from one end, as shown in figure 3.8. The actual picture of the sensor can be found in figure 3.9. Table 3.5 shows the printing parameters of the sensor. Since, the sensor was printed at a glass bed temperature of 75 °C and PI-EPTU 85-700+ has very good adhesive properties to glass, the sensor was printed on top of a BVOH (butenediol vinyl alcohol copolymer) layer [52] to facilitate easy removal from the build platform. It

is a water-soluble support material and has good bonding with nearly all build materials. The sensor performance is discussed in section 5.5.

Table 3.5: Print settings for DSNJX60

Printing parameter	PI-EPTU85-700+	X60	NinjaFLex
Layer height	50 µm	50 µm	50 µm
Infill	100 %	80 %	100 %
Print Temperature	220 °C	230 °C	215 °C
Nozzle Diameter	0.4 mm	0.4 mm	0.4 mm
Extrusion width multiplier	1	1	1
Extrusion width	0.4	0.4	0.4
Cam dial settings	3	1	2

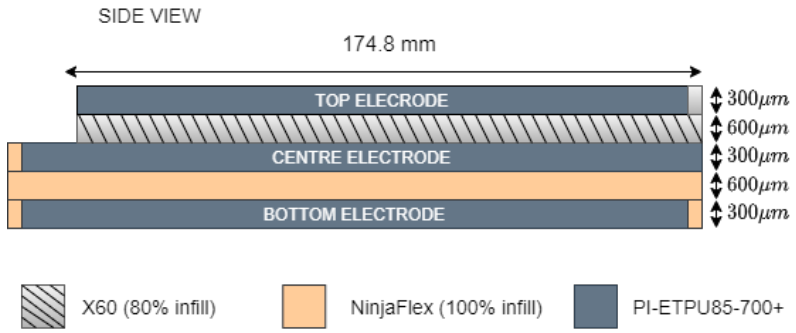

Figure 3.8: Schematic diagram of the differential sensor with NinjaFlex and X60 dielectric

Figure 3.9: Picture of the differential sensor with NinjaFlex and X60 dielectric

3.9 Differential Sensor with X60 dielectric (DSX60INF)

The sensor was the fifth and final prototype based on the differential analytical model. X60 dielectric was used for both the sensors with the top dielectric printed 70 % infill to improve the sensitivity and exhibit symmetric behaviour due to similar mechanical properties, e.g. creep. The sensor dimensions are the same as DSNJX60, as shown in figure 3.10. Table 3.6 shows the printing parameters. The actual picture of the sensor can be found in figure 3.11. The sensor performance and experimental results are discussed in section 5.6.

Table 3.6: Print settings for DSX60INF

Printing parameter	PI-EPTU 85-700+	X60
Layer height	50 µm	50 µm
Infill	100 %	80 %, 100 %
Print Temperature	210 °C	230 °C
Nozzle Diameter	0.4 mm	0.4 mm
Extrusion width multiplier	1	1
Extrusion width	0.44	0.44
Cam dial settings	3	1

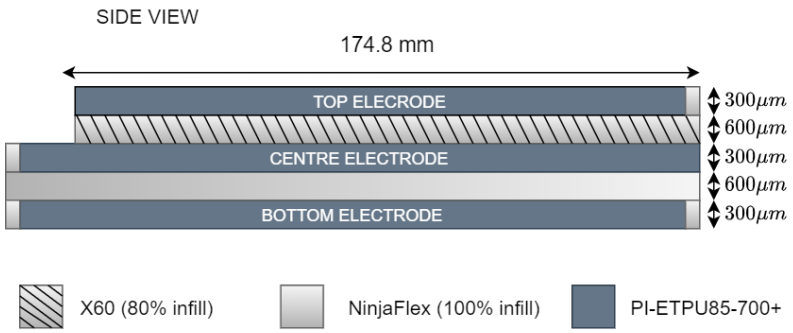

Figure 3.10: Schematic diagram of the differential sensor with X60 dielectric

Figure 3.11: Schematic diagram of the differential sensor with X60 dielectric

3.10 Conclusions

The chapter discussed the design and fabrication process of the sensor and the effects of the printing parameters on the fabrication process.

- PI-eTPU 85-700+ is used to print the electrodes due to its low resistivity and flexibility.
- The dielectric of the sensor is printed using flexible TPU material, NinjaFlex and X60.
- Extrusion multiplier of 1 ± 0.3 is used to yield clean and consistent prints.
- X60 dielectric is printed with a lower infill percentage to improve the sensitivity of the sensor.
- Annealed sensors showed improvement in the electrical conductivity of the electrodes.

The next chapter discusses the experiments performed on these sensors to characterize the change in impedance.

4 Experimentation

4.1 Introduction

This chapter explains the types of experiments performed to determine the performance of the fabricated sensors. Followed by the explanation of experimental setup, types of equipment used, and readout techniques are discussed. The final goal of the experiments is the characterization of the change in impedance as a function of the magnitude and position of an applied force.

4.2 Experimental Setup

The two-point impedance measurement is done with the sensor, electrical contacts are made by applying the silver conductive paint (Ag) on the ends of the top and bottom electrodes, as shown in figure 3.11. Next, the copper tape is placed on the mount and the clamp, as shown in figure 4.1. Using the copper tape with silver ink ensures that there is less contact resistance. Next, the sensor is placed on the mount and clamped from both ends, as shown in figure 4.2a. The electrical connections are made, and the sensor is connected to the LCR, as shown in figure 4.2b.

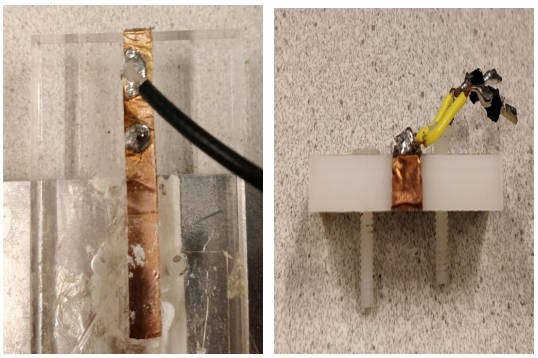

(a) **(b)**

Figure 4.1: (a) Copper tape is placed on the mount with soldered wires to connect the bottom electrode, (b) Copper tape placed on the clamp with soldered wires to connect the top electrode

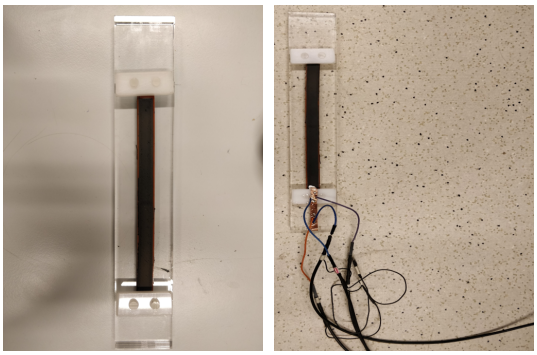

(a) **(b)**

Figure 4.2: (a) Sensor places on the mount and clamped from both ends, (b) Electrical connections are made and the sensor is connected to the LCR

4.2.1 Linear actuator setup

A vertical compressive force is applied to the sensor using a force-controlled linear-actuator. The SMAC actuator (LCA25-050-15F) is controlled via the LCC-10 controller using a simple force control Python script. Figure 4.3 shows the layout of the linear actuation setup. The linear actuator is mounted vertically, as shown in figure 4.4 and the weight of the actuator is 90 g So when applying the force to the sensor, an additional value of 0.9 N is added to the applied force value.

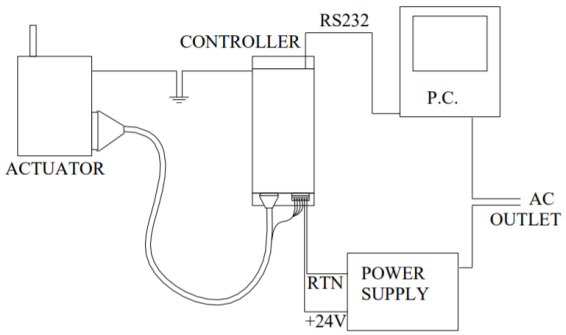

Figure 4.3: Schematic diagram of the linear actuation setup [2].

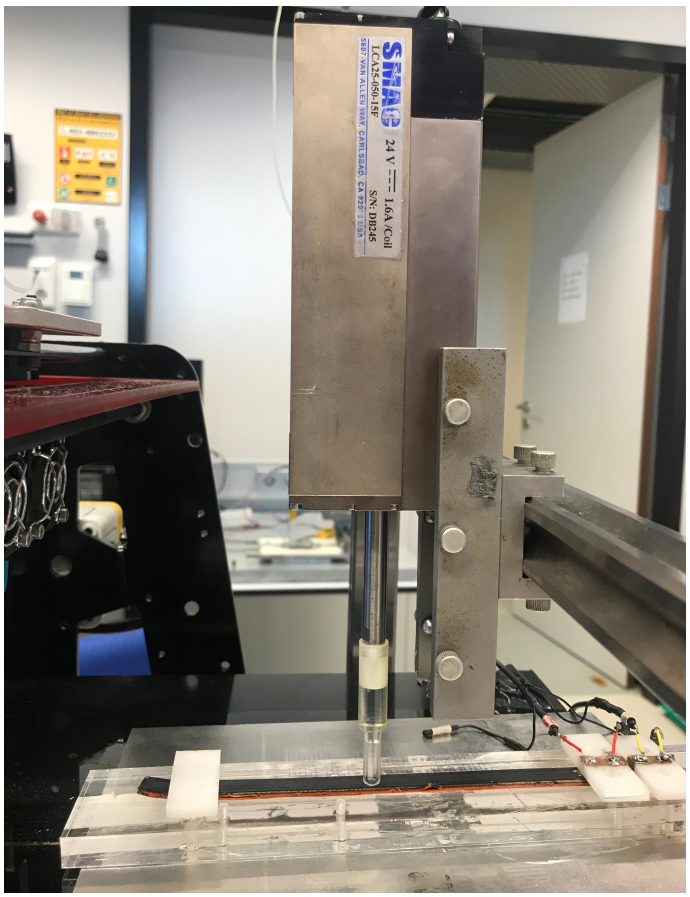

Figure 4.4: Picture of the linear actuator mounted vertically on the steel frame. The actuator applies compressive vertical force on the sensor at different positions. An actuator tip placed on the piston reduces the interference due to capacitive coupling.

4.3 Measurement setup for Experiments

It is established in chapter 2 that the impedance changes with respect to the applied force and position where the force is applied. To verify and characterize the fabricated sensors, three types of experiments were performed:

1. **Forward-Backward:** let us assume the end where the input signal is given to be point 'A' and the other end of the sensor to be point 'B'. The sensor is applied with a constant vertical compressive force at various positions starting from point $A \rightarrow B$ and back from point $B \rightarrow A$. The impedance value at each press is recorded using an LCR-meter. Moving forward and backwards between two points helps gain more insight into the behaviour of the sensor.

2. **Multiple presses at single points:** To test the repeatability of the sensors, a compressive force is applied at any single point on the sensor ten times. The impedance values are recorded at each press using an LCR meter.

3. **Multiple force at different position**: This basically combines the previous two experiments. A compressive force of 4,5,6,9 and 12 N is applied for 2 s, and the measurement is repeated at a different position in a forward-backwards press.

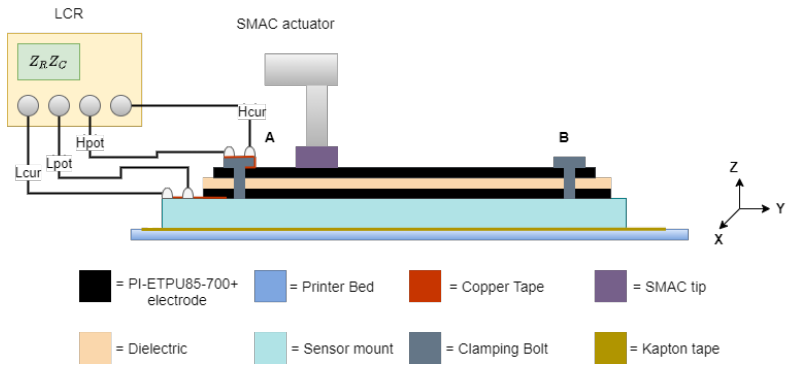

Figure 4.5: Schematic diagram of the experiment setup

The printer bed of a RoVa 3D printer by ORD solutions was used to perform the above two experiments. The build plate moves along the y-axis. The sensor mount was placed on the ground steel plate and fixed on the bed using double-sided tape. A layer of Kapton tape was placed on the bed before placing the mount to avoid damage from the double-sided tape. The linear actuator was mounted clamped on a steel frame, fixing it at a fixed height above the print bed. The control of the bed's movement, actuator actuation, and recording of the change in impedance values was done using a python script. The sensor clamped at both ends on the mount is positioned along the y-axis, next the actuator applied a compressive force ranging from 1-10 N at that particular position, and the change in impedance was recorded. The measurement is repeated after increasing the y-axis position of the bed. Figure 4.5 and 4.6 show the measurement setup for the parallel plate and differential sensor respectively.

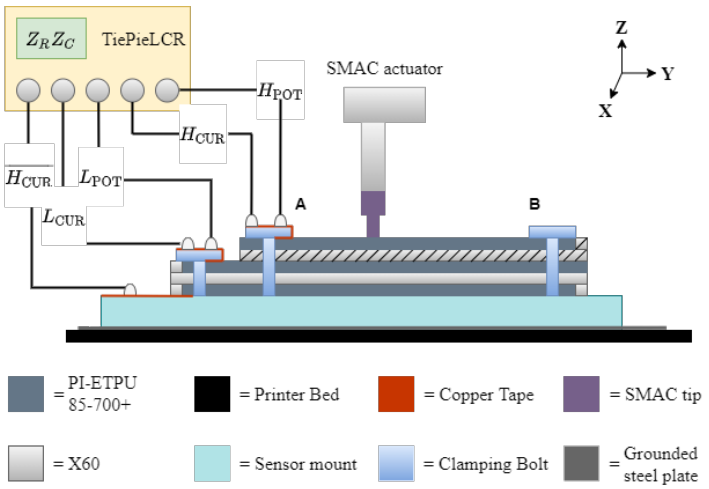

Figure 4.6: Schematic diagram of the experiment setup

4.4 Readout Techniques

The sensor readout is done using an impedance analyzer. The sensor is connected to the impedance analyzer, as shown in figure-4.5. Two LCR meters are used throughout the experiments, and both of them will be explained in this section.

4.4.1 HP4284A

The HP4284A is an LCR meter that uses an auto-balancing bridge method, as shown in figure 4.7 to measure the sensor's impedance. The circuit has four terminals H_{CUR}, H_{POT}, L_{CUR} and L_{POT}, all of which are connected to the sensor. The H_{CUR} applies a measurement current generated using a controlled frequency and amplitude to the sensor with a frequency range of 20 Hz to 1 MHz. The L_{CUR} terminal converts the current flowing through the sensor into a voltage, based on the detected resistance, while the terminal's potential is held to 0 V. The voltage across the sensor is measured using the H_{POT} and L_{POT} terminals. The circuit has phase detectors that measure voltage and current in a phase-locked manner and precisely identify the phase angle, θ between them. The measured impedance consists of real and imaginary parts. The impedance in rectangular form is given by:

$$Z = R + jX \tag{4.1}$$

Where the resistance, R represents the real or in-phase part of the impedance and the reactance, jX represents the imaginary or 90° out of phase part of the impedance (capacitance). The actual resistance and capacitance values are calculated using real and imaginary parts [3, 53]. Usually, LCR meters have two RC circuit measurement modes, series and parallel. Series measurement mode is chosen since the lumped model of our sensor is resistance and capacitance in series.

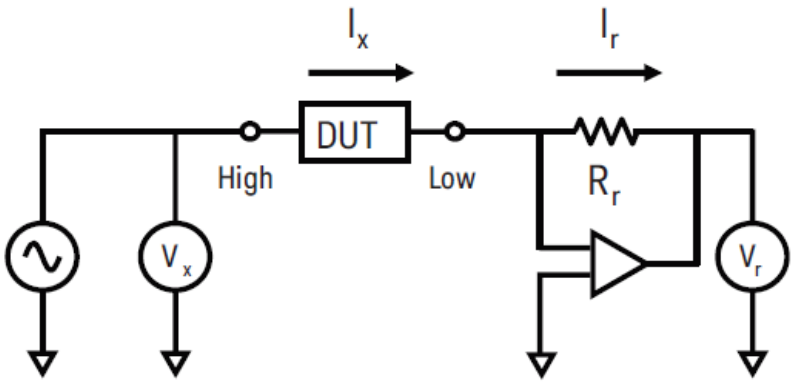

Figure 4.7: Schematic of auto balance of bridge method [3, p. 2-04].

4.4.2 TiePieLCR

This LCR is built by M. Schouten, the circuit uses a differential auto-balancing bridge method and is built using LTC6268 and LTC6268-10 opamps, combining high input impedance with a large gain-bandwidth. The LCR is connected to the Handyscope HS5-540 oscilloscope, the waveform generator of the oscilloscope generates a harmonic excitation signal that is connected to the input voltage V_{in}. The voltage and current are demodulated using a python script to calculate the impedance. The main advantage of this method is the continuous measurement of impedance with a large bandwidth. Figure 4.8 shows the simplified circuit diagram of the TiePieLCR and figure 4.9 shows the GUI of the TiePieLCR.

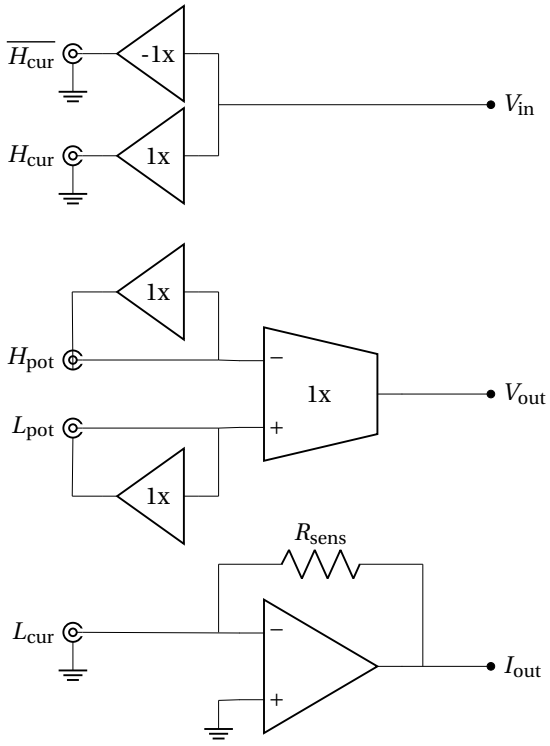

Figure 4.8: Simplified circuit diagram of the TiePieLCR. Image courtesy of appendix A. The connection of this circuit to the sensor is shown in figure 4.6.

.

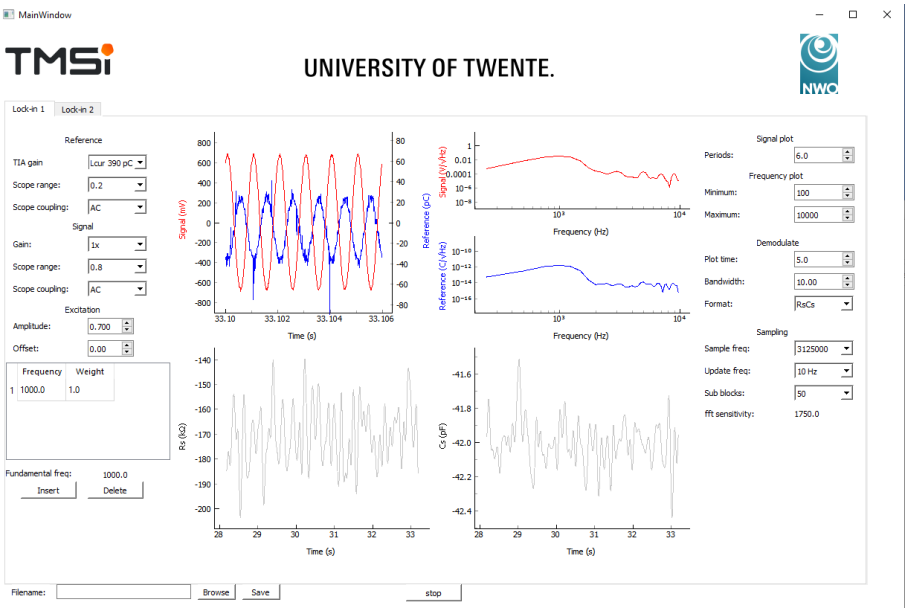

Figure 4.9: GUI of the TiePieLCR

Readout technique for SNJ,SX60,SESX60

The impedance is measured using the HP4284A LCR meter; a two-point measurement is done in a four-terminal configuration, as shown in figure 4.10. It reduces the measurement errors due to lead impedance and contact resistances by using separate cables for current and voltage detection [3, p. 3-04]. Also, at low impedance, a large current flows through the current lead generating the leads' magnetic field, leading to mutual coupling between the current and voltage leads. This effect of mutual coupling is solved using the outer shield conductors, which work as a return path for the current signal. The magnetic field due to the inner and outer current signal cancel out each other [3, p. 3-06]. However, the sensors in this assignment have high impedance hence, the effect of mutual coupling is neglected. The top electrode is connected to H_{CUR} and H_{POT} and the bottom electrode is connected to the L_{CUR} and L_{POT}. The impedance values are measured at an input voltage of 1 V and a frequency of range 1-20 kHz.

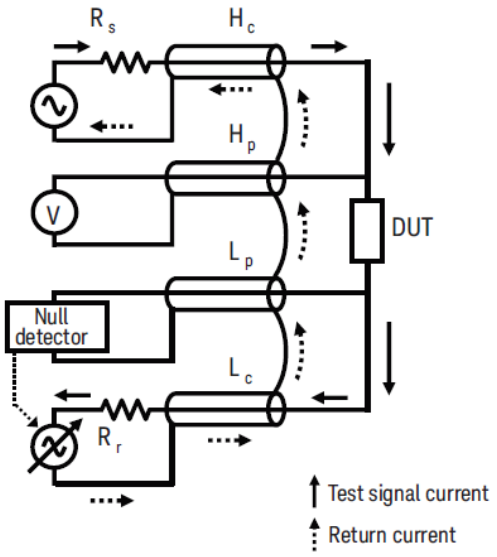

Figure 4.10: Schematic of a four-terminal configuration [3, p. 3-04].

Differential readout

Initially, the impedance of the differential sensor was measured using a combination HP4284A and the TiePieLCR. An inverse measurement current ($\overline{H_{\text{cur}}}$) is given to the bottom electrode, the centre electrode being the common electrode is connected to the L_{CUR} and L_{POT}. The top electrode is supplied with measurement signal H_{CUR} and connected to higher potential H_{POT}. Figure-4.11 differential readout setup, the measurement signal H_{CUR} from HP4284A is split to obtain the inverse signal ($\overline{H_{\text{cur}}}$). This leads to a five-terminal configuration. The measured impedance is the difference between the two sensors.

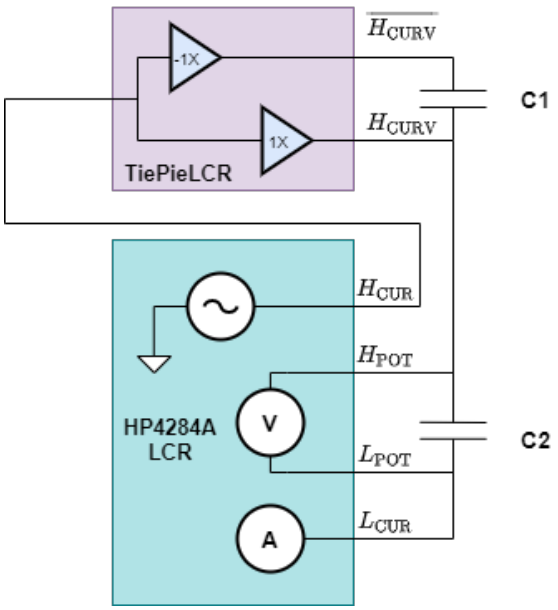

Figure 4.11: Schematic of five-terminal configuration

During the later stages of the experiments, when the TiePieLCR was ready and the demodulation process was complete, the differential impedance was measured using only the TiePieLCR setup since it offers continuous impedance measurements.

4.5 Linear actuator Tip

The linear actuator consists of a metal piston sliding in an actuator to apply the compressive force. Since the actuator and the sensor are at a different potential, capacitive coupling can occur between the tip and the area where it is pressed during the pressing situation. The noise-induced due to coupling can interfere with the impedance measurements [54]. The distance between the sensor and the piston was increased using a dielectric actuator tip to reduce noise effects. The tips were designed, and 3D printed iteratively.

4.5.1 Flat tip

The first prototype will be referred to as the flat tip, as shown in figure 4.12. The tip was fabricated using VeroBlack [55], a hard Polyjet material. The hollow part is a cylinder with one open end with a wall thickness of 0.60 mm that encapsulates the actuator's metal tip; the solid part presses the sensor. The radius of the tip is 9.15 mm which is less than the width of the sensor. (1 cm).

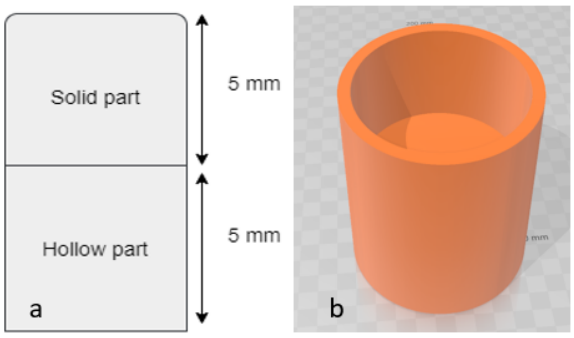

Figure 4.12: a) Schematic of the flat tip, b) STL file

4.5.2 Round tip

Since the sensor is pressed with a force of up to 11 N, to ensure that the pressure applied by the actuator is distributed evenly on the pressed area, a second prototype was designed and fabricated using AGILUS30 black [56], which is a flexible Polyjet material. It will be referred to as the round tip. Figure 4.13 shows the schematic, STL file and actual picture of the second prototype. Even after multiple experiments, there was no permanent deformation in the solid part of the tip. The material is quite flexible and regains its original shape after the press motion.

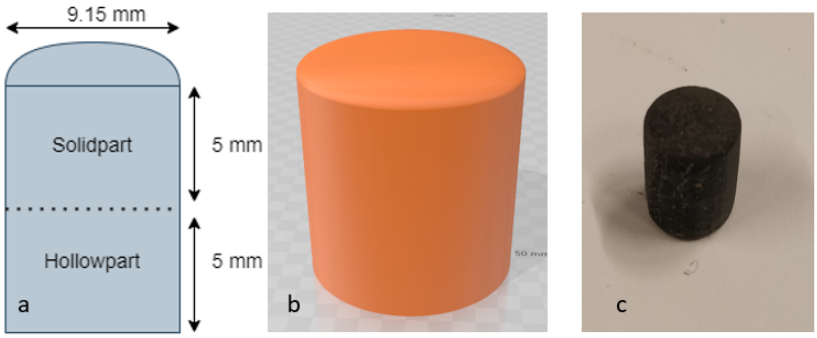

Figure 4.13: a) Schematic of the round tip, b) STL file, c) Picture of the second prototype

4.5.3 Soft and Hard tip

The thin cylinder walls of the round tip got loose after multiple presses and were no longer able to encapsulate the metal tip properly. So, it was necessary to redesign the tips. The third prototype was designed and fabricated using two materials and will be referred to as the soft tip. The part that presses on to the sensor was fabricated using AGILUS30 black flexible Polyjet material. The part that encapsulates the tip of the actuator was fabricated using hard and transparent Veroclear [57] Polyjet material. A fourth and final prototype was designed and fabricated using only the Veroclear Polyjet material and will be referred as hard tip. The part that presses on to the sensor is a cylinder with one end open. The cylinder wall thickness of both prototypes was increased to 1 mm. The length of both the prototypes was further increased to 3 cm to reduce the capacitive coupling between the linear actuator and the sensor. Figure 4.14 shows the schematic and picture of the tips. The performance of the hard and soft tip is compared in section 5.6.1.

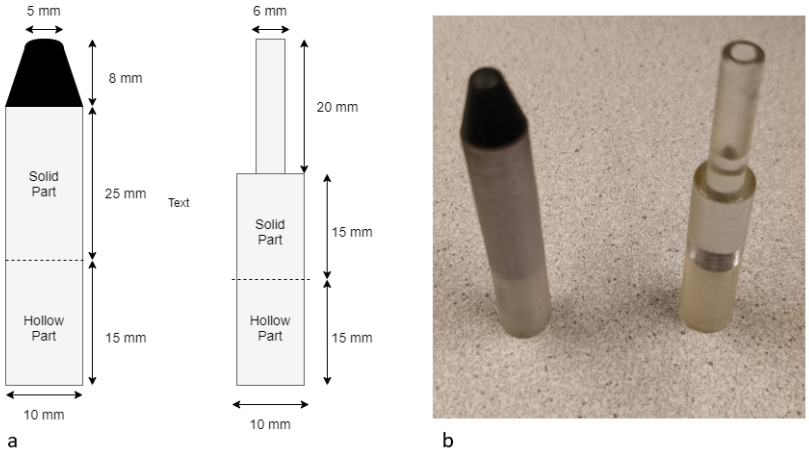

Figure 4.14: a) Schematic of the soft and hard tip, b) Picture of the tips

4.6 Conclusions

The chapter discussed the experiments performed to characterize the change in impedance along with the experimental setup and readout techniques. Following are the conclusions of this chapter:

- Copper tape and silver conductive paint are used to form the electrical contacts.
- The sensor has a low-complexity sensor with only four electrical connections.
- A two-point impedance measurement is performed to calculate the change in the impedance of the sensor.
- Two types of experiments are performed to characterize the change in impedance as a function of magnitude and position of an applied force.
- The sensor is pressed multiple times at a single point to check for repeatability.
- Four different types of tips are designed and fabricated to reduce the noise from the linear actuator.

Chapter 5 discusses the results of the experiments performed.

5 Results and discussion

5.1 Introduction

This chapter discusses the results of the experiments described in previous chapters. The experiments are done iteratively, the results of each sensor is analyzed which explains why a new prototype was designed, modelled and fabricated. The chapter also discusses the reasons behind the different readout techniques used throughout the experiment process.

5.2 Sensor SNJ

The SNJ was the first sensor fabricated and tested. The measured capacitance using the HP4248A LCR meter was 254.64 pF and the resistance was 12.89 kΩ at 1 kHz. The cut-off frequency of the sensor calculated using equation 2.56 was 48 kHz.The measured resistance of the top electrode was 2.45 kΩ and the electrical resistivity calculated using 5.1

$$\rho = \frac{RL}{A} \tag{5.1}$$

was 0.04 Ω m. Similarly, the measured resistance of the bottom electrode was 1.969 kΩ and the calculated electrical resistivity 0.046 Ω m. The relative permittivity calculated using 5.2

$$\varepsilon_r = \frac{Cd}{\varepsilon_0 A} \tag{5.2}$$

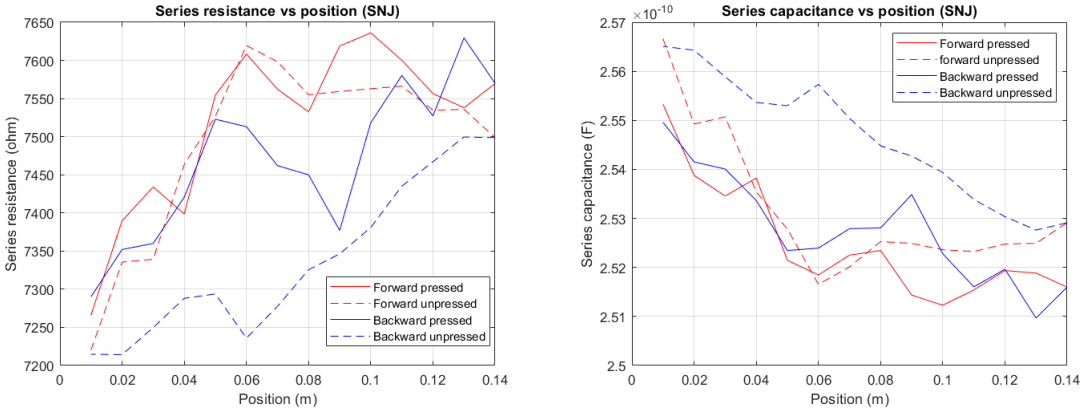

(a) Series resistance vs position

(b) Series capacitance vs position

Figure 5.1: Series resistance and capacitance against position (TiePie). There is drift in the baseline unpressed condition. The trend in the series resistance and series capacitance do not match the model.

was 5.73.

5.2.1 Measurement with TiePieLCR

The sensor was subjected to a continuous forward-backwards experiment. A compressive force of 5.7 N was applied on the sensor with the flat tip. The impedance at each press was measured using the TiePieLCR at an input frequency of 19 kHz which was below the cut-off frequency.

Figure 5.1a shows the measured series resistance as a function of position where the force is applied. The behaviour of resistance is different from what was predicted in the model; the difference between the pressed and unpressed situation seems random at each position. Given the same configuration of the experimental setup and the continuous forward and backward

press, the result shows drift in the baseline unpressed condition. Although the forward direction and backward direction press follow the same trend with respect to the position, it is still unclear where exactly the sensor was pressed. The change in the series resistance from one end to another end in the pressed condition is 4.17 % for forward pressing cycle and 3.69 % for backward pressing cycle.

The capacitance was calculated from the imaginary impedance using equation 2.57. As predicted in the model the capacitance is a straight line independent of the position and only depends on the applied force. However, figure 5.1b shows drift in the unpressed situation, the change in the capacitance in unpressed situation from one end to another end is 1.4 % for both forward and backward pressing cycle. The capacitance should increase when the sensor is pressed however the change in the unpressed capacitance with position is more than the pressed condition.

5.2.2 Measurement with HP4248A

The configuration of the experimental setup was the same except that the TiePieLCR was replaced with the HP4248A LCR meter. The sensor was also subjected to the same continuous forward backward press.

Figure 5.2a shows the measured series resistance as a function of position where the force is applied. It can clearly be seen that there is drift in the unpressed situation. There is no clear trend between the pressed and unpressed condition. At few positions the pressed situation had less resistance than the unpressed situation which is not possible according to our model. The change in resistance from one end to another end in the pressed situation is 3.78 % in forward pressing cycle and 3.4 % in backwards pressing cycle.

Similarly, the results of series capacitance, figure 5.2b, showed a drift in the unpressed condition. There is no clear trend between the pressed and unpressed condition. The capacitance change from one end to another end in the unpressed condition is 2 % for forward pressing cycle and 1.6 % for backwards pressing cycle. One interesting thing about figure 5.2a and 5.2b is that the trend of pressed and unpressed conditions in one figure is an inverse of the trend in other figure. However, the reason is unclear.

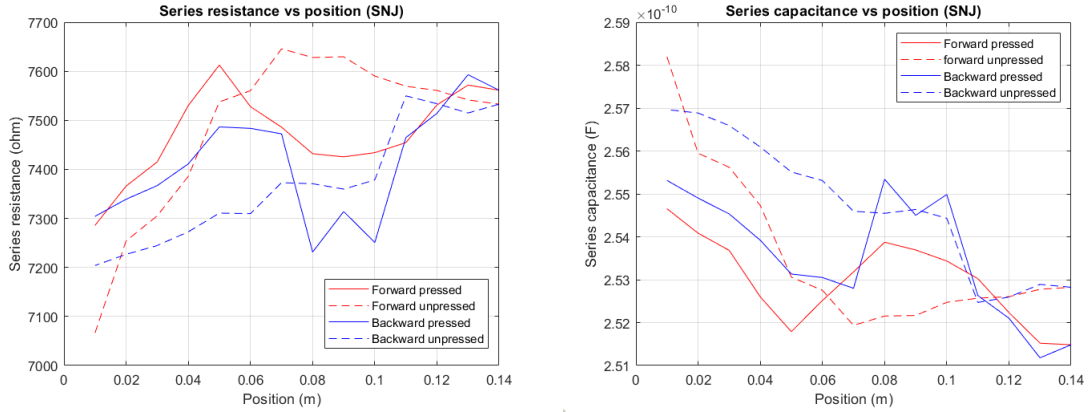

(a) Series resistance vs position

(b) Series capacitance vs position

Figure 5.2: Series resistance and capacitance against position (HP4248A). There is drift in the baseline unpressed condition. The trend in the series resistance and series capacitance do not match the model.

5.2.3 Conclusion

The results show large drift in unpressed condition in all the measurements. From the resistance values it is unclear if the sensor was pressed. The change in the capacitance in pressed

condition is less than the unpressed condition at some positions. The senor did not perform as predicted in the model. The reason behind the error in the measurements is unclear as there are many factors such as:

- The electrical noise induced by the linear actuator, due to improper grounding of the linear actuator and the sensor.
- The input frequency can be too high for the measurements due to which the drift of the resistive part also shows up in the capacitive measurements.
- One of the bugs in the demodulation in the TiePieLCR caused the drift in the measurement.
- The actuator with the flat tip induced mechanical noise by not pressing the sensor in exactly the same way each time, due to play on the actuator shaft.

It can be concluded that the combination of measurement and sensor did not work as expected.

5.3 Sensor SX60

The goal was to fabricate a more sensitive sensor. Hence, X60 was used as dielectric since it has a lower tensile modulus and shore hardness than NinjaFlex. This is expected to improve the sensitivity of the sensor. The measured capacitance using HP4248A was 265 pF and resistance was 42 kΩ at 1 kHz with a cut-off frequency of 14.3 kHz. The measured electrical resistance of the top electrode was 25.35 kΩ and the resistivity calculated using equation 5.1 was 0.5 Ω m. Similarly, for bottom electrode the measured resistance was 25.7 kΩ and calculated electrical resistivity 0.60 Ω m. The calculated relative permittivity ε_r using equation 5.2 was 5.98.

5.3.1 Measurements with TiePieLCR

The sensor was subjected to the same experimental configuration as before except that the round tip was used which was made from flexible Polyjet material in an attempt to make the effect of the actuator presses more consistent. The impedance was measured using the TiePieLCR at an input frequency of 19 kHz. The input frequency was kept above the cut-off frequency and the goal was to examine the position dependence of the resistive part.

Figure 5.3a shows the measured series resistance as a function of position where the force is applied. The resistive part has high sensitivity compared to the results for the SNJ sensor and moreover shows a reasonable consistency as far as the difference between pressed and unpressed condition is considered. However, the sensor did not behave as predicted in the model and there is drift in the baseline unpressed condition. The change in resistance from one end to another end in the pressed condition is 3.94 % for the forward pressing cycle and 1.38 % for the backward pressing cycle. The pressed and unpressed condition have the same trend however, there is still too much drift to be able to determine where the sensor was pressed.

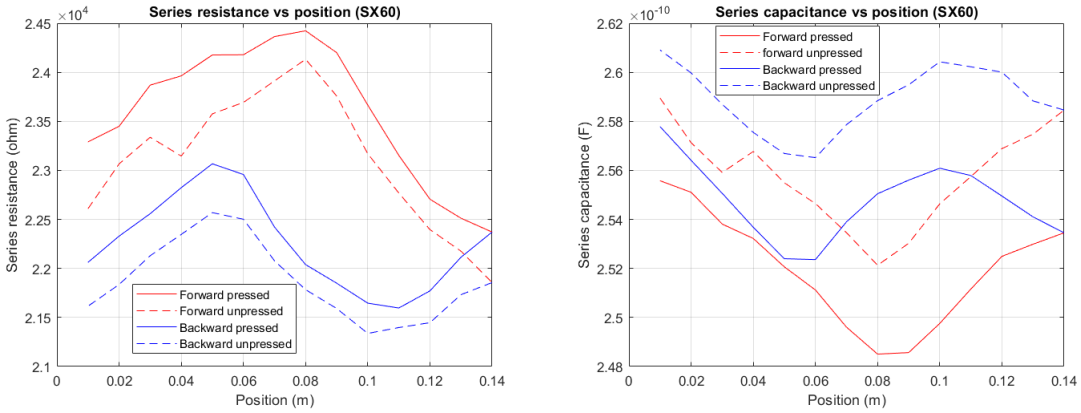

(a) Series resistance vs position

(b) Series capacitance vs position

Figure 5.3: Series resistance and capacitance measurements against position (TiePie). The results show a reasonable consistency compared to sensor SNJ however, there still too much drift to resolve where the sensor was pressed. The decrease in the capacitance after the press is expected to be due to a bug in the TiePieLCR

Figure 5.3b shows the series capacitance as a function of position where the force is applied. There is drift in the baseline unpressed condition but it follows the same trend in the forward and backward press. The change in the capacitance from one end to another end in unpressed condition is 0.18 % for froward pressing cycle and 0.94 % for backward pressing cycle. It should also be noted that for this sensor the press caused a decrease of the capacitance instead of an increase, this is expected to be due to a bug in the TiepieLCR demodulation algorithm. The results with the HP4248A LCR meter are shown in the appendix B.1.

5.3.2 Conclusion

The same experiment setup was tested with a different sensor and the key takeaways from the measurements are:

- The sensitivity was improved by using X60 as the dielectric, the sensor did not work as expected based on the model.
- There is drift in the baseline unpressed condition in both the series resistance and capacitance.
- The measurement was performed above cut-off frequency and therefore an effect of the drift of the resistive part on the capacitive part can be expected.
- To prevent this drift input frequency should be lowered.
- The measurements showed reasonable consistency however the exact effects of the round actuator tip is unclear.

5.4 Sensor SESX60

The sensor was the third prototype fabricated, there were two requirements: 1) The sensor should have an increased cut-frequency. 2) the electrodes should have the same size. The first requirement was accomplished by increasing the dielectric thickness to 600 µm. The increase in the dielectric thickness decreases the capacitance and increases the cut-off frequency. The thickness of 600 µm was chosen after trials and errors as it does not decrease the capacitance too much and prevents the electrode from short-circuiting. To reduce the EMI induced by the

linear actuator, a common mode filter circuit was connected to the output of the controller of the actuator. Thick shielded cables were used and the linear actuator was connected to ground.

The measured capacitance was 139 pF and resistance was 58 kΩ at 1 kHz with cut-off frequency of 20 kHz. The electrical resistance of the top electrode was 32.44 kΩ and the calculated resistivity using equation 5.1 was 0.8 Ω m. Similarly, the bottom electrode resistance and resistivity was 21.89 kΩ and 0.68 Ω m respecively. The calculated relative permittivity ε_r using equation 5.2 was 6.28. The impedance measurements were done using the HP4248A LCR meter with an input frequency of 3 kHz for both the experiments.

5.4.1 Multiple presses at single point

To check the repeatability, the sensor was subjected to a compressive force of 11 N for 5 s. The impedance was recorded before and after the press. The measurement was repeated 10 times. Figure 5.4a shows the series resistance as a function of applied force. Both the pressed and unpressed condition is quite stable. The mean of the difference between the pressed and unpressed condition is 237 Ω. The change in the series resistance of the pressed condition between the first and last press is 0.15 % with a standard deviation of 14 Ω.

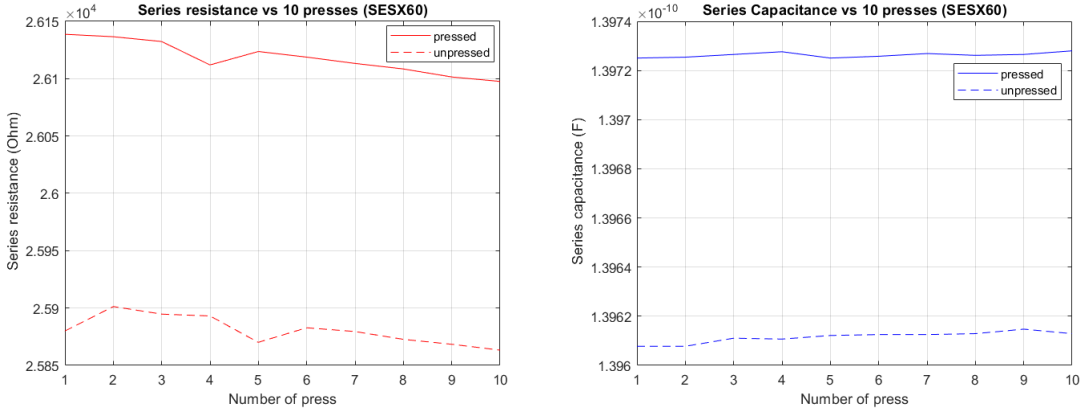

(a) Series resistance vs 10 presses

(b) Series capacitance vs 10 presses

Figure 5.4: Series resistance and capacitance measurements against 10 presses at single point (HP4248A). The pressed and unpressed condition are quite stable. The change in resistance is 237 Ω and the change in capacitance is 114 fF.

Figure 5.4b shows the series capacitance as a function of applied force. Since, the dielectric thickness was doubled the capacitance is reduced by a factor of 2. The pressed and unpressed condition is almost a straight line. The sensor has a change in the capacitance of 114 fF with a standard deviation of 1.2 fF.

5.4.2 Position measurements

To measure the impedance as a function of position the sensor was subjected to forward-backward press experiment with the same compressive force of 11 N. Figure 5.5a shows the series resistance as a function position where the force is applied. The measurements show drift in the base line unpressed condition. The change in the series resistance in the pressed condition is 0.64 % for forward press and 0.27 % for backward press. It is unclear where the sensor was pressed as the change in resistance between pressed and unpressed is the same approximately for all positions in both forward and backwards direction press.

Similarly, the capacitance measurement shows drift in the unpressed condition, as shown in figure 5.5b. The change in the series capacitance in unpressed condition is 0.05 % for the for-

ward pressing cycle and 0.02 % for the backward pressing cycle. If compared to the previous sensors there is improvement in the capacitance readings.

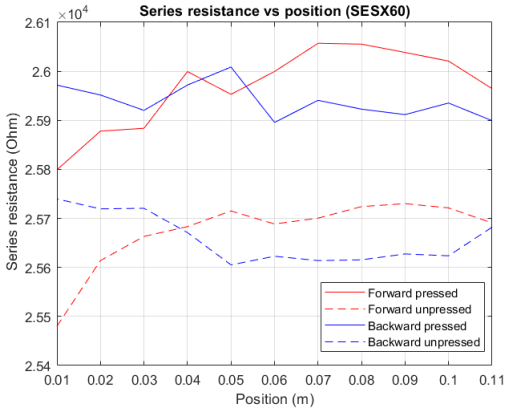

(a) Series resistance vs position

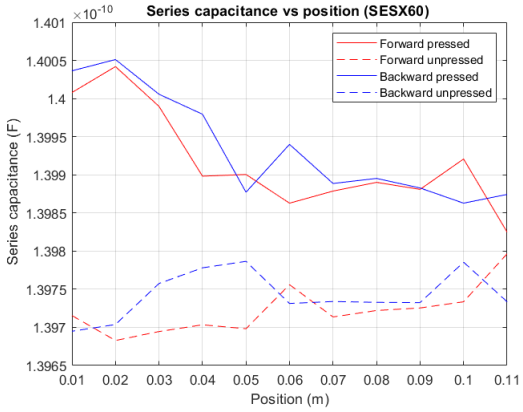

(b) Series capacitance vs position

Figure 5.5: Series resistance and capacitance measurements against position (HP4248A). The measurements show drift and do not resolve where the sensor was pressed.

5.4.3 Conclusion

The key takeaways from these measurements are:

- The sensor when pressed at a single point multiple times shows good response.
- The measurements of forward-backward experiment to determine the position show drift in the unpressed condition.
- The measurements do not resolve where the sensor is pressed.
- Reducing the noise and proper grounding did help improve the performance of the sensor.

It can be concluded that the sensor did not work as expected.

5.5 Sensor DSNJX60

The sensor was the fourth prototype fabricated. The goal was to reduce the drift and non-linearity in the resistive and the capacitive part and hence, the differential sensor was fabricated to compensate that. The dielectric thickness of both the NinjaFlex and X60 was 600 µm. The X60 dielectric between the top and centre electrode was printed with an infill of 80 % to make it more compressible and sensitive without short circuiting the electrodes. The measured capacitance C_1 of the top parallel plate sensor was 139 pF with a relative permittivity ε_1 of 6.33 (using equation 5.2). Similarly, the capacitance C_2 of the bottom parallel plate sensor was 108.3 pF with a relative permittivity of ε_2 of 4.89. The electrical resistance and resistivity calculated using equation 5.1 of the top electrode was 4.45 kΩ and 0.07 Ω m respectively. Similarly, for the bottom electrode the resistance and resistivity was 4.78 kΩ and 0.072 Ω m respectively.

The differential impedance was measured using both the HP4248A and TiePieLCR in a five terminal configuration (see figure 4.11) with a readout frequency of 3 kHz

5.5.1 Multiple presses at single point

To check the repeatability the sensor was subjected to a compressive force of 11 N for 3 s and unloaded for 2 s. The impedance was recorded before and after the press, the measurement was

repeated 10 times. Figure 5.6a and 5.6b show the series resistance and capacitance as a function of applied force. The response in the pressed and unpressed condition is quite stable. The mean difference between the pressed and unpressed condition for the resistance is 2680 Ω and for the capacitance it is 237 fF. The change in the resistance between the first and the last press is 1.6 % with a standard deviation of 255 Ω. Similarly, the standard deviation for capacitance is 7.8 fF.

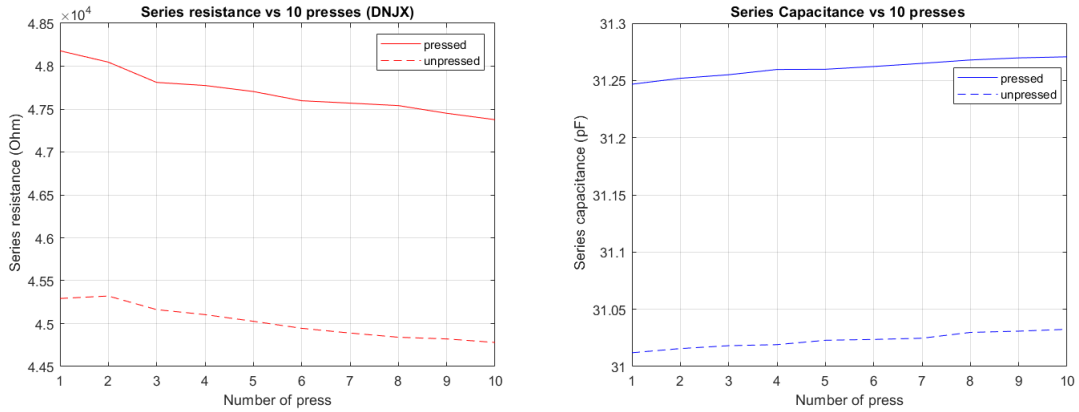

(a) Series resistance vs 10 presses

(b) Series capacitance vs 10 presses

Figure 5.6: Series resistance and capacitance measurements against 10 presses at a single point

5.5.2 Position measurements

To measure the impedance as a function of the pressed position the sensor was subjected to a forward-backward experiment with the same compressive force of 11 N. Figure 5.7a shows the series resistance as a function of position where the force is applied. The differential measurements shows improvement in the drift and non-linearity of the baseline unpressed condition. The resistance in the pressed condition is increasing with position. The behaviour of the sensor is opposite to the one predicted by the model. Since, the sensor is based on a lossy transmission line the change in the resistance should decrease with increasing position from the source. The change in the resistance in the pressed condition for forward and backward press is 4.7 %.

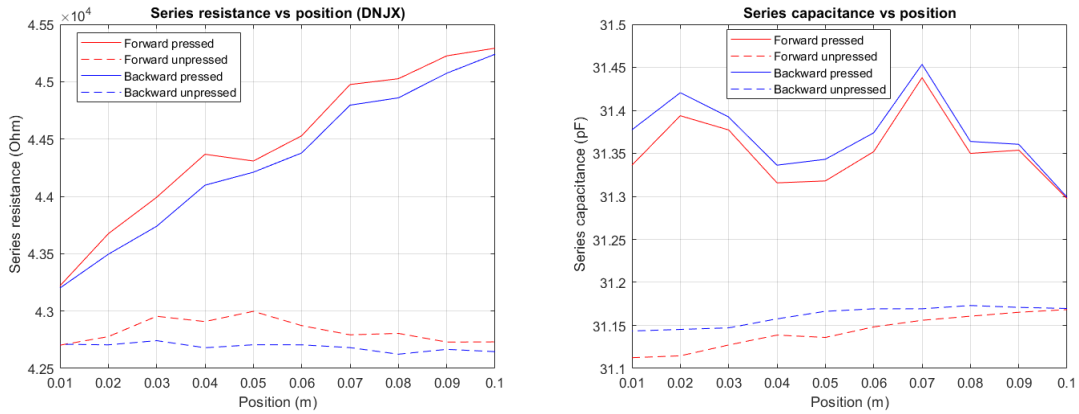

(a) Series resistance vs position

(b) Series capacitance vs position

Figure 5.7: Series resistance and capacitance measurements against position

Similarly, figure 5.7b shows the capacitance as a function of applied force and the position where the force is applied. The measurement shows improvement in the baseline unpressed

condition. The pressed condition follows the same trend in forward and backward press. The change in the capacitance in pressed condition is 0.05 %.

5.5.3 Conclusion

The key takeaways from these measurements are:

- The sensor shows good response when pressed multiple times at a single point.
- The differential readout reduced the drift and non-linearity in the unpressed condition.
- The series resistance is increasing with increase in position which is opposite of what is predicted by model.
- There is no such improvement in the measurement of the capacitance .

5.6 Sensor DSX60INF

This was the fifth and the final prototype fabricated. Since, the fabrication of the previous sensor was a success the sensor was printed with an X60 dielectric for both the top and the bottom sensor to have more symmetric behaviour. The infill percentage was decreased to 70 % to make the top sensor more compressible. The dimensions of the sensor were kept the same as for the previous sensor. The measured capacitance C_1 of the top parallel plate sensor was 101 pF with the relative permittivity of 4.68. Similarly, the capacitance C_2 of the bottom parallel plate was 160 pF with a relative permittivity of 6.54. The cut-off frequency of the sensor was 24 698 Hz. The differential impedance measurement was done using the TiePieLCR. Until now the impedance was recorded just before and after the press however, in these experiments the measurements were done continuously and instead the timestamps of the pressed and unpressed conditions were recorded. The ground of the LCR was connected to the common ground. To reduce the capacitive coupling between sensor and SMAC, longer tips were fabricated and used (third and fourth prototype). The tips were compared during the multiple press experiments.

5.6.1 Multiple presses at a single point

To check the repeatability, the sensor was subjected to a compressive force of 4.9 N for 3 s and unloaded for 2 s. The linear actuator is lowered with a smaller force (just high enough to overcome friction) and then pressed with 4.9 N of force on the sensor. The timestamps were recorded before and after the press, the measurement was repeated 10 times. The experiment was performed twice, first with the soft tip and then with the hard tip. Figure 5.8a and 5.8b show the measured series resistance and capacitance. The measurement is continuous with the timestamps (circles). In the previous measurements the impedance was recorded just before and after the press. However, by performing continuous measurements more insight can be gained into impedance behaviour of the sensor after the press. Information of the other factors on the measurements like the moving the bed can be obtained. However, for data analysis and better understanding the measurement data is plot into a bar graph. Figure 5.9 and 5.10 show the comparison of series resistance and capacitance of two tips. The measurement shown is the difference between the pressed and unpressed condition. Table 5.1 shows the comparison of the change in resistance and capacitance for both the tips.

Table 5.1: Analysis of two tips

	Soft tip	Hard tip
mean (ΔR)	$-783\,\Omega$	$-1.37\,k\Omega$
Standard deviation (R)	$127\,\Omega$	$137\,\Omega$
mean (ΔC)	137 fF	167 fF
Standard deviation (C)	0.0084 pF	0.0145 pF

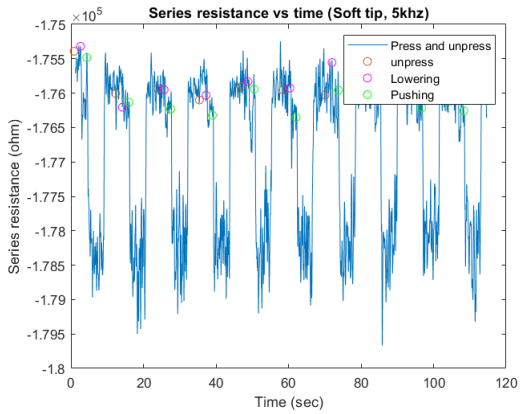

(a) Series resistance vs time

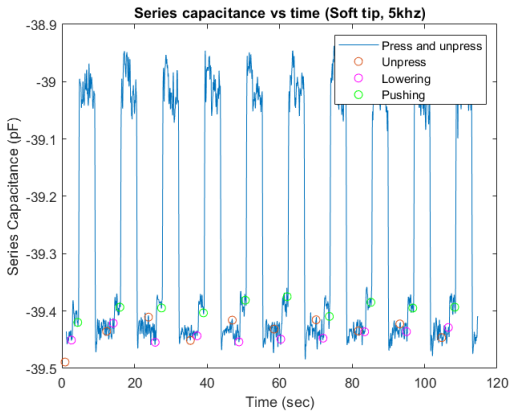

(b) Series capacitance vs time

Figure 5.8: Series resistance and capacitance measurements for multiple presses at a single point.

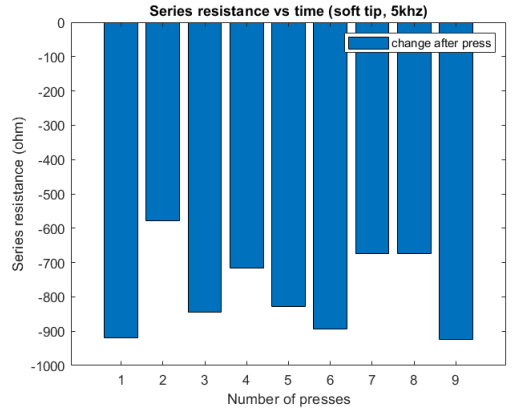

(a) Series resistance (Soft tip)

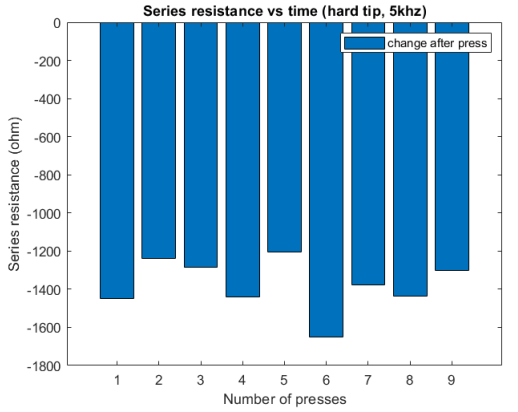

(b) Series resistance (Hard tip)

Figure 5.9: Comparison of change in series resistance between pressed and unpressed conditions for the two tips

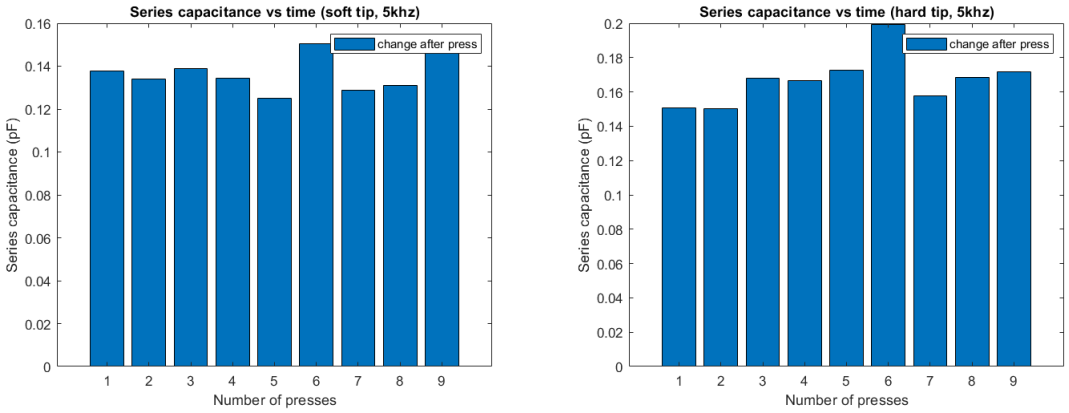

(a) Series capacitance (Soft tip)

(b) Series capacitance (Hard tip)

Figure 5.10: Comparison of change in series capacitance between pressed and unpressed conditions for the two tips

The mean change in the capacitance is almost similar for both the tips however, the mean of change in resistance is higher when pressed with the hard tip. This is expected because when the actuator with the soft tip applies compressive force, the flexible part of the tip deforms and the pressure is applied evenly on the sensor surface. When pressing with the hard tip the force applied is concentrated on a smaller area and hence there is more electrode deformation. The experiments were done 2 more times at higher frequencies to confirm the effects of both tips. The results are shown in the appendix B.2 and B.3. Hence, for further experiments the hard tip was chosen as the tip of the actuator.

5.6.2 Position measurement

To measure the impedance as a function of position, a force of 4.9 N was applied and the forward-backward experiment was performed. Figure 5.11a shows the measurement data of the series resistance as a function of position where the force is applied and the time stamps (circles). The change in the resistance is decreasing with increasing position, as predicted in the model. The resistance is negative and the change is decreasing because the differential measurement is the relative change in the resistance of the top and bottom sensor. The bottom electrode has larger resistance and experiences more change when pressed. The change in the resistance in the pressed condition forward press is 0.93 % and for backward press is 0.63 %. Figure 5.12a shows the bar graph illustration of the series resistance of the pressed condition. The capacitance shown in the figure 5.11b is negative as the capacitance of the bottom capacitor is bigger than the top capacitor. The measured capacitance is almost a straight line with change in pressed condition of 0.12 % for forward press and 0.14 % for backward press. For better understanding a bar graph illustration is shown in figure 5.12b.

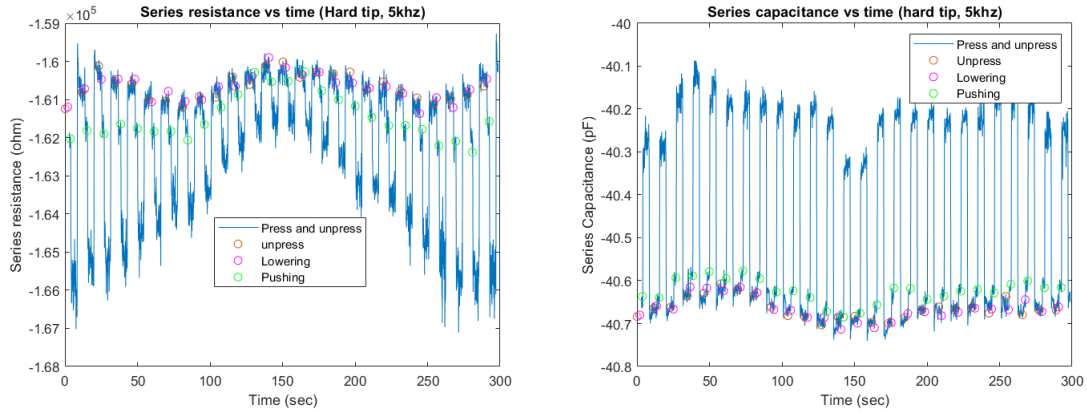

(a) Series resistance vs time

(b) Series capacitance vs time

Figure 5.11: Series resistance and capacitance measurements for forward-backward press.

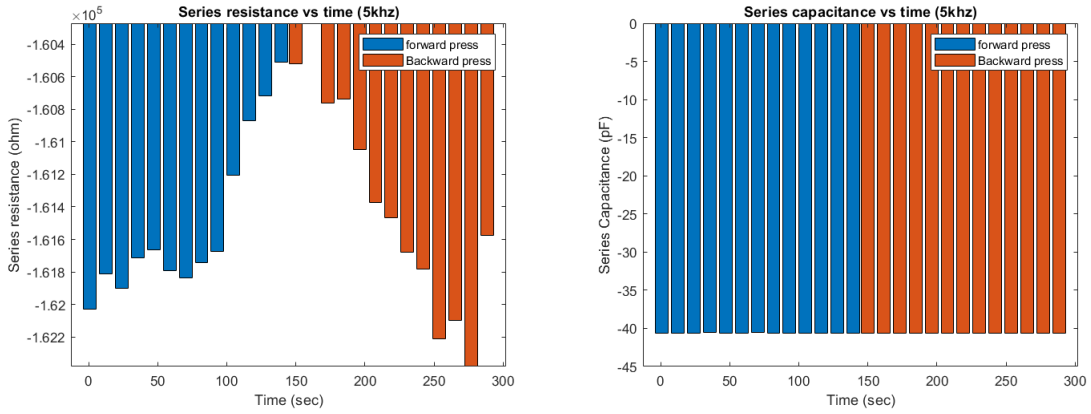

(a) Series resistance vs time

(b) Series capacitance vs time

Figure 5.12: Series resistance and capacitance measurements for forward-backward press.

Position measurements at 25 kHz

At lower frequencies the imaginary part of the impedance is more dominant and it becomes harder to measure the real part of the impedance as they are in series. So, to see the position dependence of the real part more clearly, the measurement was done at 25 kHz which is slightly above the cut-off frequency. Figure 5.13 shows the series resistance as a function position where the force is applied. The change in the pressed condition is 3.3 % for forward press and 2.97 % for backward press. The change in resistance is more clear compared to the change at 5 kHz.

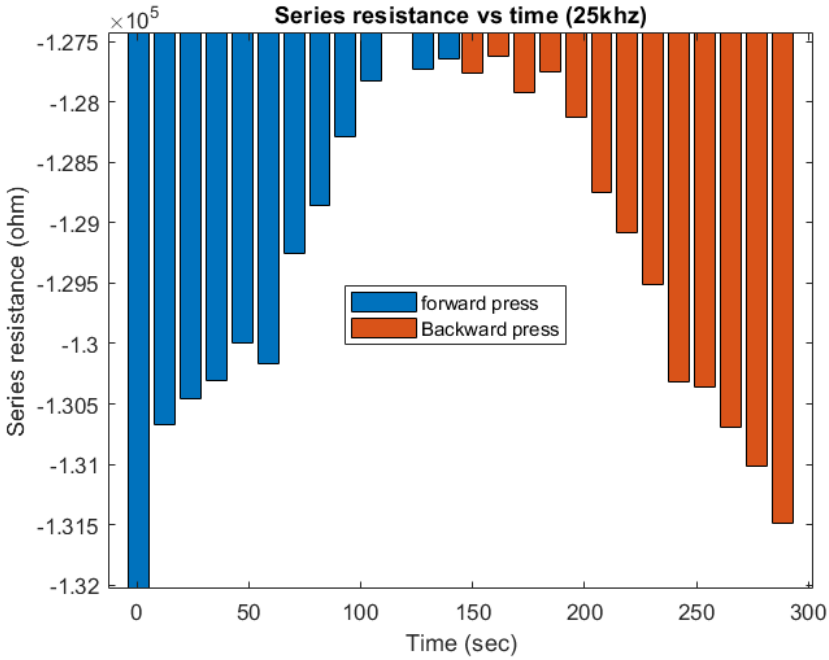

Figure 5.13: Series resistance vs time (DSX60INF)

5.6.3 Multiple presses at each position

Since the sensor showed a position dependent real part in the measurement the sensor was subjected to the third type of experiment where the linear actuator applied a consecutive compressive force of 3.9, 4.9, 6.9, 8.9 and 11.9 N for 2 s at one position. The measurement was repeated after increasing the position. The readout frequency was lowered to 3 kHz.

Figure 5.14a shows the measured series resistance as a function of applied force and the position where the force is applied. The impedance data was processed in Matlab using a FIR low-pass filter with a cut-off frequency of 0.5 Hz to reduce the noise in the measurements. The sensor is more sensitive to changing force values at small positions with a change of 9 kΩ. Similarly, Figure 5.14b shows the series capacitance, the change in capacitance is 940 fF.

Although, due to the noise in measurements, the capacitance is not completely independent of position and, as mentioned in the previous section, that it becomes harder to measure the real part at lower frequency, the measurement results are reasonably comparable to the simulated results.

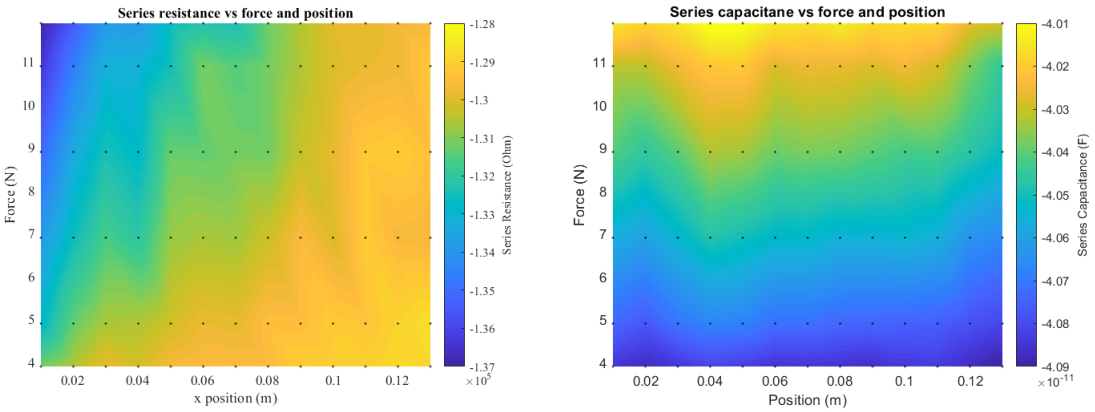

(a) Series resistance vs force and position

(b) Series resistance vs force and position

Figure 5.14: Series resistance and capacitance measurements against force and position (the black dots are measurement points).

5.6.4 Frequency Sweep

A frequency sweep with six orders of magnitude from 10 Hz to 1 MHz was performed on the sensor using TiePieLCR. To verify the results, the impedance spectrum was also measured using HP4248A. Figure 5.15 shows that the impedance spectrum both the LCR follow the same trend and the sensor behaves well until 10 kHz. However, the simulation trend is slightly different from the measurements. The measured spectrum deviates from the simulation at low and high frequency. The deviation in the resistance at low frequency is expected due to the model not taking into account the dielectric loss and leakage of dielectric. The deviation at high frequency might be due to the steel ground plate not being taken into account.

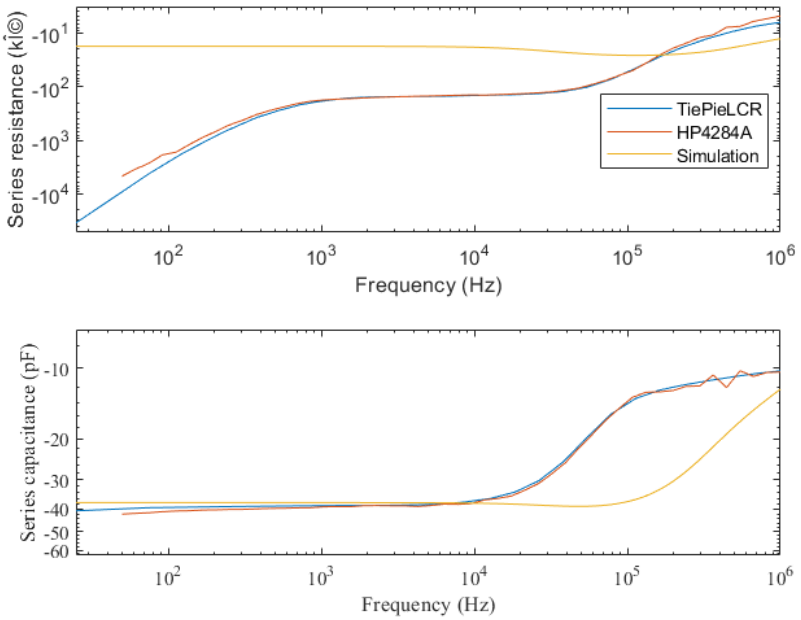

Figure 5.15: Measured and simulated differential impedance spectrum (DSX60INF)

5.7 Conclusion

This chapter discussed the results of the impedance measurements of all the five sensors. Following are the conclusions of this chapter:

- The impedance measurements of the parallel plate sensors SNJand SX60 showed drift and non-linearity in the baseline unpressed condition due to the noise-induced by a linear actuator.
- The electrical noise was reduced by grounding the linear actuator, connecting a common mode filter circuit and the mechanical noise was reduced by fabricating actuator tips.
- Reducing the noise showed improvement in the results of multiple presses at a single point experiment for SESX60.
- However, the position measurements of SESX60 still showed drift in the unpressed conditions.
- It can be concluded that the sensors SNJ, SX60, SESX60 did not work as predicted by their model.
- Two differential sensor DSNJX60 and DSX60INF were fabricated iteratively to compensate the drift and non-linearity.
- Impedance measurements of DSNJX60 showed improvement in the drift and non-linearity however, the position measurements were not reasonable.
- The demodulation algorithm of the TiePieLCR was fixed, and the impedance measurements of DSX60INF showed improvement in the position measurements.
- Soft and hard tips were compared by performing multiple pressed at a single point experiment, and hard tip produced more change in the resistance and capacitance.
- The results of multiple force at different position experiment with DSX60INF were reasonably comparable to the simulated results.

6 Conclusion

This thesis aims to design a sensor that can measure the magnitude and position of an applied force by measuring the change in impedance of the sensor. To help achieve this goal, a set of sub-questions were defined. This chapter will try to answer these sub-questions and, thereby, the main research question.

Which operating principle of the force sensor can be used to measure the magnitude and position of an applied force?

- For this, a literature survey was conducted, and different capacitive force sensors were studied.
- From this survey a model was selected which models the capacitive sensor as a lossy transmission line and this formed as a basis for the sensor in this assignment.
- The force applied to the sensor changes the sensor's resistance and capacitance, which changes the impedance.
- The change in the piezoresistivity of the electrodes determine the position of an applied force
- The change in capacitance between the electrodes determine the magnitude of an applied force.

How can the sensor's electrical characteristics be modelled?

- The sensor's electrical characteristics are modelled using the partial differential equations of the voltage and current along the transmission line.
- The differential equations are solved using the eigenvalue expansion and their corresponding eigenvectors with the coefficients determined by the boundary conditions.
- The model is then implemented in the MATLAB® and the impedance has been calculated as a function of magnitude and position of an applied force.
- The 3D plot results showed that the imaginary impedance is only dependent on the force and real impedance is force and position-dependent.
- Since the senors' lumped model is an RC low-pass filter, the sensor behaviour is different at high frequencies, and this behaviour only holds up to a frequency of 10 kHz.

How can the sensor be designed, fabricated and tested based on this analytical model?

- The experiments were performed iteratively; each sensor's results were analyzed and compared to the analytical model.
- The impedance measurements were performed in a two-point measurement using HP4248A LCR meter and in house developed TiePieLCR.
- At the start, a thin and flexible parallel plate capacitive sensor is designed and fabricated using FDM.
- The sensor designed has low complexity with only 4 electrical connections.
- Printing parameters such as infill percentage for the dielectric, nozzle temperature and extrusion multiplier are explored.

- The sensor electrodes are printed using a flexible conductive TPU material, and the dielectric material is printed using a flexible TPU material NinjaFlex and X60.
- Sensor SNJ, SX60 and SESX60 (parallel plate models) did not produce reasonable results because there were drift and non-linearity in the measurement.
- There was noise in the measurements due to electrical and mechanical noise induced by the linear actuator.
- The electrical noise was reduced by connecting a common mode filter circuit to the controller of the actuator, and the mechanical noise was reduced by modifying the actuator tips.
- The dielectric with a lower infill percentage was used to improve the sensitivity of the sensor.
- A new differential sensor design where two capacitive sensors are printed on top of each other was proposed to reduce the drift and non-linearity in the resistive part.
- The demodulation algorithm of the TiePieLCR was also fixed, and LCR was connected to the common ground.
- The differential sensor was modelled and tested the same way as the parallel plate sensor.
- DSX60INF produced satisfactory results which after processing were comparable to the analytical model.

How can the force and position be determined from the impedance values?

- The thesis aims to determine the magnitude and position of an applied force. However, for the experiments, the impedance was calculated at a known force and position.
- To determine the force and position from the impedance values, an inverse model was derived is implemented in the MATLAB®.
- Considering the time and resource constraints, the inverse model was implemented for the model data only.

After answering all sub-questions, this thesis concludes by addressing the main research question.

Is it possible to design and fabricate a sensor that can measure the magnitude and position of an applied force by measuring the change in impedance?

The thesis was aimed at designing a 3D printed flexible force and position sensor based on a lossy transmission line. The differential capacitive sensor results suggest that it is possible to determine the force and position from the change in impedance value. However, this research is far from complete, and there are many avenues to model, design, test and improve sensor behaviour. Few suggestions on this are presented in the next section.

6.1 Discussion and Future recommendation

This section discusses the ideas and further improvements to the current research.

1. The aim was to design and fabricate a working sensor; hence, a simple parallel plate sensor was designed. However, new design ideas can be explored by defining proper design constraints. The electrodes can be printed using various conductive materials other than the PI-eTPU 85-700+ and similarly for the dielectric. Infill percentage and extrusion multiplier are the only parameters changed during fabrication; however, more

research can be done on the effects of other parameters such as layer height, printing speed, different infill patterns on the electrical and mechanical properties of the sensor.

2. The experiments were done iteratively; however, there is a need for a more systematic approach to performing impedance measurements. It will ensure that the sensors are tested under the same conditions, and hence, a proper comparison between different sensor prototypes can be established. There is a need for more reliable readout electronics. The electrical connections to the sensor can be improved by using pogo pins.

3. The sensor is tested within a limited force range of 4-12 N considering the time and resources constraints. Hence, the senor behaviour outside this range is unknown and requires further research.

4. The sensor designed is a 1D sensor with a position resolution up to 10 cm. This can be increased to 2D by implementing a similar approach used by Xu et. al [23]. The multi-frequency approach can be used to implement a multi-touch sensor.

5. A proper post-processing script can be developed to reduce the noise in the measurements. The current inverse model is limited to model data, and it can be further developed to process the measurement data.

A Differential force and position sensor paper

3D PRINTED DIFFERENTIAL FORCE AND POSITION SENSOR BASED ON LOSSY TRANSMISSION LINES

Martijn Schouten, Parth Patel, Remco Sanders, Gijs Krijnen
Robotics And Mechatronics group, University of Twente, Enschede, The Netherlands

ABSTRACT

This paper describes a differential capacitive sensor, which uses the piezoresistivity of the used electrodes to determine both the force that is applied to the sensor and the position where the force is applied. To do so both the real and the imaginary parts of the impedance of the sensor are used. We present the idea, its analysis as well as experimental results showing the feasibility of our approach.

INTRODUCTION

Previously it has been shown that a flexible parallel plate capacitor can be used to measure the applied normal force [1]. It also has been shown that a similar structure using multi-frequency readout can be used to measure force and the position where it is applied in 2D [2]. Structures like these enable flexible devices with few connections while still offering the possibility to determine a 2D resolved position of the point of contact of a force.

In a comparable fashion we here introduce a method to measure the magnitude of a force as well as its position along a given elongated structure by measuring the real and imaginary impedance of a 3D printed differential capacitive structure at a single frequency below the cut-off frequency of the sensor. In this approach the imaginary part of the impedance exclusively gives information on the magnitude of the force whereas the real part is affected by both the magnitude and the position of the force through the piezoresistive effect of the material. By doing so we show that it is already possible to measure the position where the force is applied using a single frequency measurement.

OPERATING PRINCIPLE AND MODEL

A cross-section of the proposed structure is shown in figure 1. The basis of the structure is formed by 3 layers of conductive thermoplastic polyurethane (TPU) layers, acting as the electrodes of the two capacitors. Between the top and middle layer a soft layer of X60 of 70 % infill provides a relative deformable upper capacitor, whereas the X60 layer of 100 % infill between the middle and bottom electrode provides a much stiffer structure, to act as reference capacitance. A circuit representation of an infinitely small part of the proposed geometry is shown in figure 2

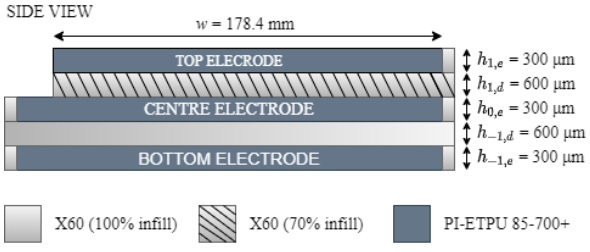

Fig. 1. Dimension of the 3D printed sensor.

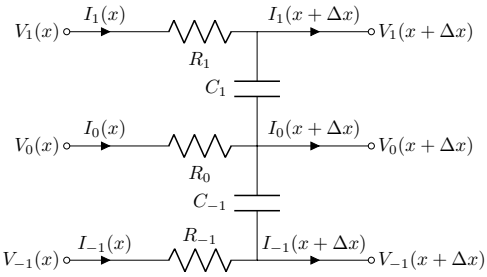

Fig. 2. Electrical circuit diagram of an infinitesimal part of the sensor

Due to the large resistance of the parallel plates of the 3D printed parallel plate capacitors they are expected to behave like a very lossy transmission line. The differential capacitive sensor described in this work uses two of these parallel plate capacitors printed on top of each other, in order to compensate for drift and non-linearity in mainly the resistive part. The sensor therefore can be seen as a combination of two coupled lossy transmission lines, as illustrated by figure 1.

The behaviour of the voltage along the different electrodes in this circuit can be described with the following differential equations [3, p. 50]

$$\frac{dV_n(x)}{dx} = -Z_n I_n(z) \tag{1}$$

The current can be described using

$$\begin{aligned}
\frac{dI_1(x)}{dx} &= G_1\left(V_0(x) - V_1(x)\right) \\
\frac{dI_0(x)}{dx} &= G_1\left(V_1(x) - V_0(x)\right) + G_{-1}\left((V_{-1}(x) - V_0(x)\right) \\
\frac{dI_{-1}(x)}{dx} &= G_{-1}\left(V_0(x) - V_{-1}(x)\right)
\end{aligned} \tag{2}$$

with R the resistance per meter length of the electrodes and G_n the admittance per meter length of the dielectric. Both are depending on the material properties and the geometry of the sensor through:

$$\begin{aligned}
Z_n &= \frac{\rho_n}{h_{n,e} w} \\
G_n &= j\omega C_n = \frac{j\omega \epsilon_n w}{h_{n,d}}
\end{aligned} \tag{3}$$

Where ϵ_n and ρ_n are the relative permittivity of the dielectrics the resistivity of the electrodes respectively. The geometry constants h_e, w and h_n are defined in Figure 1. To solve this system of equations it is rewritten into matrix form:

$$\frac{d\vec{S}}{dx} = \mathbf{A}\vec{S} \tag{4}$$

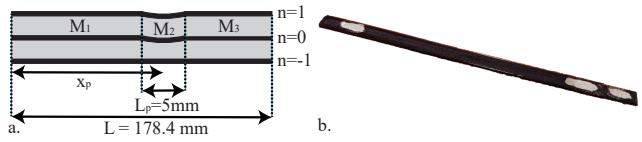

Fig. 3. a. Definition of the different sections of the sensor. b. A picture of the sensor

With:

$$S = \begin{bmatrix} V_1 \\ I_1 \\ V_0 \\ I_0 \\ V_{-1} \\ I_{-1} \end{bmatrix}, \; A = \begin{bmatrix} 0 & -Z_1 & 0 & 0 & 0 & 0 \\ -G_1 & 0 & G_1 & 0 & 0 & 0 \\ 0 & 0 & 0 & -Z_0 & 0 & 0 \\ G_1 & 0 & -G_1 - G_{-1} & 0 & G_{-1} & 0 \\ 0 & 0 & 0 & 0 & 0 & -Z_{-1} \\ 0 & 0 & G_{-1} & 0 & -G_{-1} & 0 \end{bmatrix} \tag{5}$$

The form of equation 4 suggest that a solution of this set of equations can be found from exponential functions based on the eigen-values and corresponding eigen-vectors, subjected to the proper boundary conditions. Or:

$$\overrightarrow{S}(x) = \mathbf{Y}(x)\overrightarrow{C} \tag{6}$$

with $\mathbf{Y}(x)$ a matrix formed by the eigenvectors $\overrightarrow{V}_n$ and the eigenvalues λ_n.

$$\mathbf{Y}(x) = \begin{bmatrix} \overrightarrow{V}_1 e^{\lambda_1 x} & \overrightarrow{V}_2 e^{\lambda_2 x} & \dots & \overrightarrow{V}_6 e^{\lambda_6 x} \end{bmatrix} \tag{7}$$

and $\overrightarrow{C}$ a vector of coefficients determined by the boundary conditions. In case $\overrightarrow{S}(x)$ is known at a certain position x, $\overrightarrow{C}$ can be obtained using:

$$\overrightarrow{C} = \mathbf{Y}^{-1}(x)\overrightarrow{S}(x) \tag{8}$$

This can be used to calculate the propagation of a known $S(0)$ over a length L using.

$$\overrightarrow{S}(L) = \mathbf{N}(L)\overrightarrow{S}(0) \tag{9}$$

with:

$$\mathbf{N}(L) = \mathbf{Y}(L)\mathbf{Y}^{-1}(0) \tag{10}$$

When the sensor is pressed, at the position where it is pressed it will have slightly different parameters than at the other positions where there is no applied pressure. Therefore in the analysis we split the sensor in three parts, see figure 3. Each of these sections will have its own **N** matrix, calculated using different parameters. Because the output of one section is connected to the input of the next section the overall behaviour can be obtained by multiplication of the respective **N** matrices. The matrix that can be used to calculate the propagation through the different sections in case $\overrightarrow{S}(0)$ is known, as in equation 9, can be calculated by inverting a single matrix in Matlab.

$$\mathbf{N}_{\text{tot}}(L) = \mathbf{N}_3\left(L - x_\text{p} - \frac{1}{2}L_\text{p}\right)\mathbf{N}_2\left(L_\text{p}\right)\mathbf{N}_1\left(x_\text{p} - \frac{1}{2}L_\text{p}\right) \tag{11}$$

In this work the measurement setup applies a fixed voltage on the input of the sensor. The other side of sensor is not connected and therefore the current going out is fixed at 0. In order to be able to apply this mixed boundary condition, masking matrices $\mathbf{M}_U$ and $\mathbf{M}_I$ are used to mask out the voltage and the current rows. This results in the following boundary condition equation.

$$\mathbf{M}_U\overrightarrow{S}(0) + \mathbf{M}_I\overrightarrow{S}(L) = \overrightarrow{B} \tag{12}$$

TABLE I
Printing parameters

	X60 100%	X60 70 %	PI-ETPU 85-700+	BVOH
Infill	100%	70 %	100%	100%
Wall line count	3	3	5	5
Top layers	N/A	1	N/A	N/A
Bottom layers	N/A	1	N/A	N/A

With:

$$\mathbf{M}_U = \begin{bmatrix} 1 & 0 & 0 & 0 & 0 & 0 \\ 0 & 0 & 0 & 0 & 0 & 0 \\ 0 & 0 & 1 & 0 & 0 & 0 \\ 0 & 0 & 0 & 0 & 0 & 0 \\ 0 & 0 & 0 & 0 & 1 & 0 \\ 0 & 0 & 0 & 0 & 0 & 0 \end{bmatrix}, \; \mathbf{M}_I = \begin{bmatrix} 0 & 0 & 0 & 0 & 0 & 0 \\ 0 & 1 & 0 & 0 & 0 & 0 \\ 0 & 0 & 0 & 0 & 0 & 0 \\ 0 & 0 & 0 & 1 & 0 & 0 \\ 0 & 0 & 0 & 0 & 0 & 0 \\ 0 & 0 & 0 & 0 & 0 & 1 \end{bmatrix}, \overrightarrow{B} = \begin{bmatrix} V_1(0) \\ I_1(L) \\ V_0(0) \\ I_0(L) \\ V_{-1}(0) \\ I_{-1}(L) \end{bmatrix} \tag{13}$$

Using these boundary conditions and equation 9 and 11, the current going into each electrode, which is part of $\overrightarrow{S}(0)$, can be calculated.

$$\overrightarrow{S}(0) = (\mathbf{M}_U + \mathbf{M}_I\mathbf{N}_{\text{tot}})^{-1}\overrightarrow{B} \tag{14}$$

Next the impedance measured by the LCR can be calculated using:

$$Z = -\frac{V_1(0) - V_0(0)}{I_0(0)} \tag{15}$$

What remains is a prediction of the change in the parameters of section 2. To predict the change in thickness the following equation can be used [1].

$$\Delta h_{n,d} = -\frac{F h_{n,d}}{A_0 E'_n} \tag{16}$$

Where Δh is the change in thickness, F is the applied force, h_n the original thickness, A_0 the original area and E' the effective Young's modulus. Since there is a relatively large amount of air in both dielectrics due to the 3D printing process, because of the air inside the dielectrics due to the printing process they will be assumed compressible (poisson ratio of zero) and the change in area of the plates will be neglected.

The piezoresistivity of the electrodes will be modelled on a macroscopic level, with a sensitivity factor S_n indicating the relative change in resistivity with applied force.

$$\frac{\Delta\rho_n}{\rho_n} = S_n F \tag{17}$$

METHODOLOGY

Sensor fabrication

The sensor was designed in Autodesk Inventor and sliced using Cura 4.7.1, using a custom post-processing script [4] and the parameters in table I. The sensor was printed on a Diabase H-series 3D printer and on top of a 200 µm thick layer of BVOH in order to make it easy to remove the sensor without damaging it. Figure 1 shows the dimensions of the 3D printed sensor.

Measurement setup

The sensor is placed on a mount and clamped from both ends. Electrical connections are made by soldering the wires to copper tape on the clamps. The copper tape is clamped onto silver conductive paint (Electrolube SCP26G) painted on the electrodes. The sensor mount is

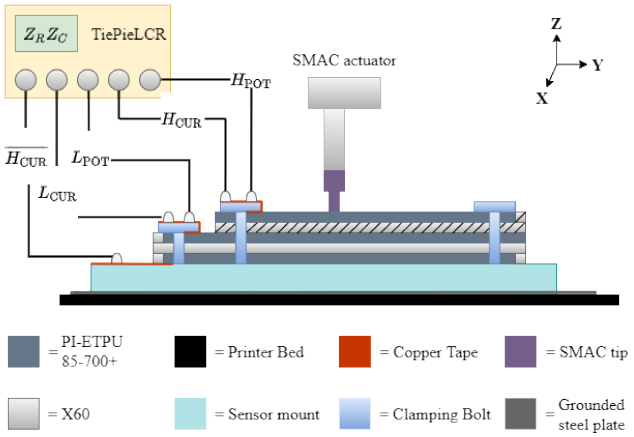

Fig. 4. Schematic of measurement setup

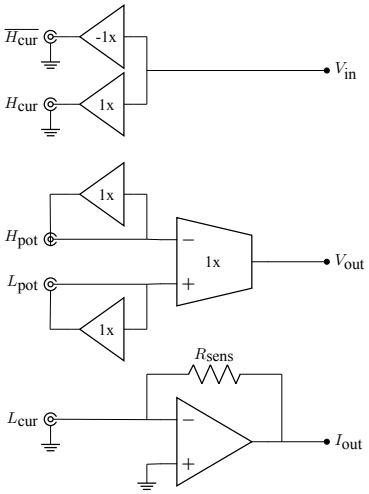

Fig. 5. Simplified circuit of the TiePieLCR. See Figure 4 for the connection of this circuit to the sensor.

placed on a grounded steel plate and fixed on the bed of a Rova3D printer by ORD solutions. The linear actuator is clamped on a steel frame fixing it at a fixed height above the print bed. To measure the impedance as a function of both force and position the linear actuator is set to consecutively apply a compressive force of 4,5,6,9 and 12 N for 2 seconds and then the measurement is repeated after increasing the y position of the bed.

Sensor readout

The readout of the sensor is done using a differential auto balancing bridge circuit [5], [6]. This circuit is build using LTC6268 and LTC6268-10 opamps, which combine a high input impedance with a large gain-bandwidth. The input impedance of the voltage measurement channels, H_{pot} and L_{pot}, are increased further by guarding the cables [7, p. 359]. The sensor is connected to this circuit as defined in Figure 4. The outputs V_{out} and I_{out} are measured using a Handyscope HS5-540 by TiePie Engineering, streaming at 3.125 MS s^{-1}. The harmonic excitation signal is generated using the arbitrary waveform generator of the Handyscope and connected to V_{in}. A python script is used to demodulate the voltage and current in order to calculate the impedance. The advantage of this approach is that the impedance can be

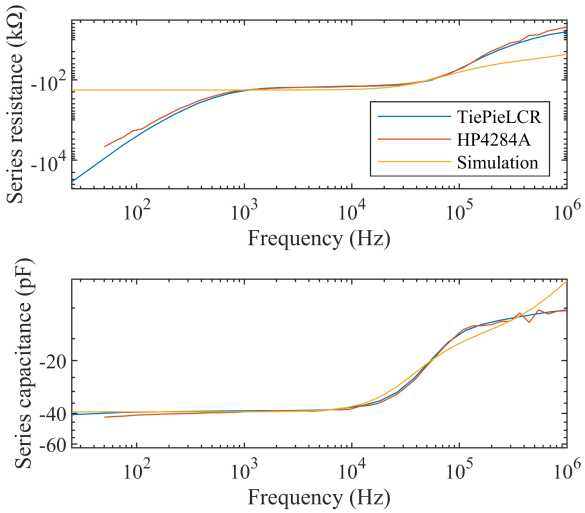

Fig. 6. Measured and predicted differential impedance spectrum

TABLE II
Parameters for fig 7

Parameter	Fit Fig 7	Start Fig 7	Fit Fig 6	Start Fig 6	Unit
ϵ_1	4.68	4.66	4.76	5.00	
ϵ_{-1}	6.54	6.54	6.54	6.70	
ρ_1	0.16	0.15	0.21	1.00	Ω m
ρ_0	0.99	0.93	1.33	1.00	Ω m
ρ_{-1}	0.04	0.04	0.05	1.00	Ω m
E'_1	0.93	1.00	N.A.	N.A.	MPa
E'_{-1}	6.00	6.00	N.A.	N.A.	MPa
S_1	0.41	0.03	N.A.	N.A.	N^{-1}
S_0	0.03	0.03	N.A.	N.A.	N^{-1}
S_{-1}	0.67	0.03	N.A.	N.A.	N^{-1}

measured continuously and with a large bandwidth. A simplified version of the circuit can be found in figure 5 and from here on will be referred to as TiePieLCR.

To verify the impedance spectrum measured by the readout circuitry the spectrum is also measured using a HP4284A LCR meter. To obtain $\overline{H_{\text{cur}}}$ for the differential measurement, the H_{cur} output of HP4284A is split by connecting the H_{cur} of the HP4284A to the V_{in} of the TiePieLCR.

Fitting

Both the impedance spectrum and measured impedance against force and position are fitted to the model by running Matlab's patternsearch on 6 cores of an i7 9850H for 30 s. For the fit of the impedance spectrum only frequencies between 1 kHz and 500 kHz have been used. Both the starting parameters and the fitted parameters can be found in Table 7.

RESULTS

Figure 6 show the measured and the simulated impedance spectrum. Figure 7 shows the simulated capacitance and resistance measurement as a function of the applied force and the position where the force is applied. For this simulations the fitted parameters in table II were used. Both the capacitance and the resistance are negative since the differences between the top and bottom capacitor are measured, and the bottom capacitance and electrode resistance are larger. The

figure shows that the imaginary part is only dependent on the force, while the real part is also dependent on the position. Figure 9 shows the measured capacitance and resistance as a function of the applied force and position.

Figure 8 plots the same data as Figure 7, but shows the force and position as a function of the capacitance and resistance, showing that it is possible to determine position and the force from these two measurements.

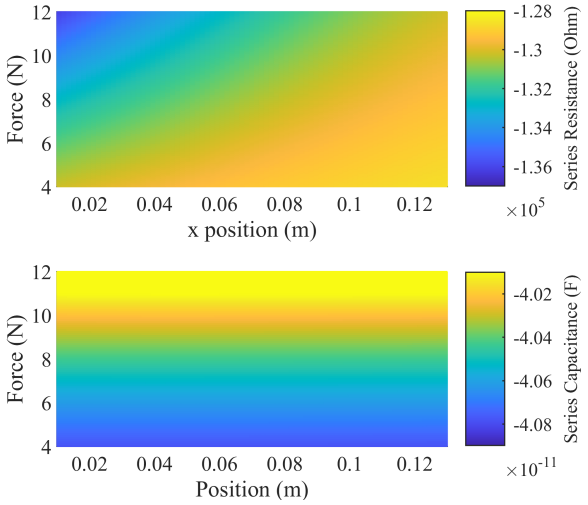

Fig. 7. Differential impedance against force and position as predicted by the model

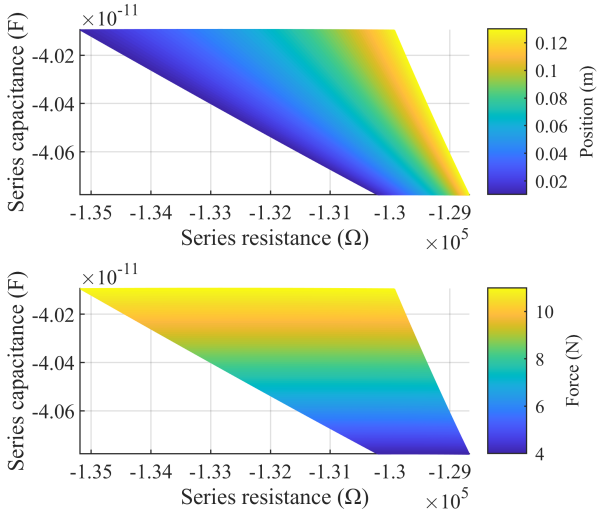

Fig. 8. Force and position against the differential impedance as predicted by the model

CONCLUSION AND DISCUSSION

In this work a model for a sensor based on a lossy transmission line that can be used to measure both magnitude and position of an applied force. Using this model was a sensor was designed and subsequently 3D printed. The capacitance of this sensor indeed was only dependent on the applied force while real part of this sensor indeed showed an dependence on both the position and the resistance.

The measured spectrum deviates from the model at low and high frequencies. The deviation in the resistance at low frequencies is expected to be due since the model does not take into account dielectric loss and leakage of

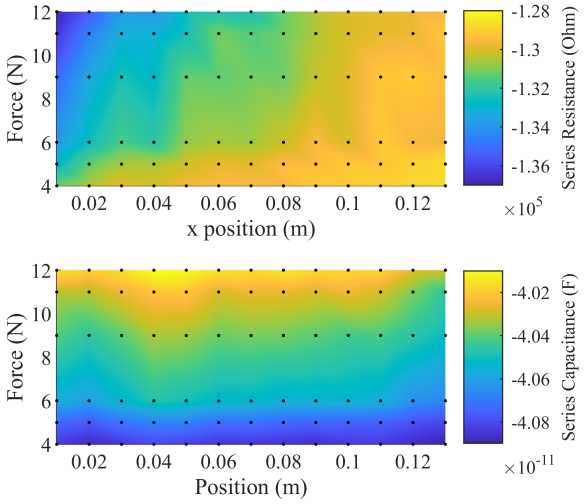

Fig. 9. Measured differential impedance against force and position. The black dots are measurement points.

the dielectric. The deviation at high frequencies might be due to the steel ground plate not being taken into account in the model.

This method has shown that it is possible to obtain even more information from the same structure, which when combined with multi-frequency readout might enable multi-touch applications or increased sensitivity. Although the current method is only implemented in 1D the method might be implemented in 2D by using a similar method as used by Xu et al. as well.

REFERENCES

[1] M. Schouten, R. Sanders, and G. Krijnen, "3D printed flexible capacitive force sensor with a simple micro-controller based readout," *Proceedings of IEEE Sensors*, vol. 2017-Decem, no. 3, pp. 1–3, 2017.

[2] D. Xu, A. Tairych, and I. A. Anderson, "Stretch not flex: programmable rubber keyboard," *Smart Materials and Structures*, vol. 25, no. 1, p. 015012, nov 2015. [Online]. Available: https://doi.org/10.1088/0964-1726/25/1/015012

[3] D. M. Pozar, *Microwave engineering*, 3rd ed. John Wilen & Sons, Inc., 2005.

[4] M. Schouten, "diabase_cura_post_processor," 2020. [Online]. Available: https://github.com/martijnschouten/diabase_cura_post_processor

[5] Keysight Technologies, "Impedance measurement handbook," access date: 16-02-2021. [Online]. Available: https://www.keysight.com/nl/en/assets/7018-06840/application-notes/5950-3000.pdf

[6] A. Dagamseh, C. Bruinink, R. Wiegerink, T. Lammerink, H. Droogendijk, and G. Krijnen, "Interfacing of differential-capacitive biomimetic hair flow-sensors for optimal sensitivity," *Journal of micromechanics and microengineering*, vol. 23, no. 3, p. 035010, Mar. 2013.

[7] P. Horowitz and W. Hill, *The Art of Electronics*, 3rd ed. USA: Cambridge University Press, 2015.

B Additional experiment results

B.1 Position measurement for SX60 using HP4248A

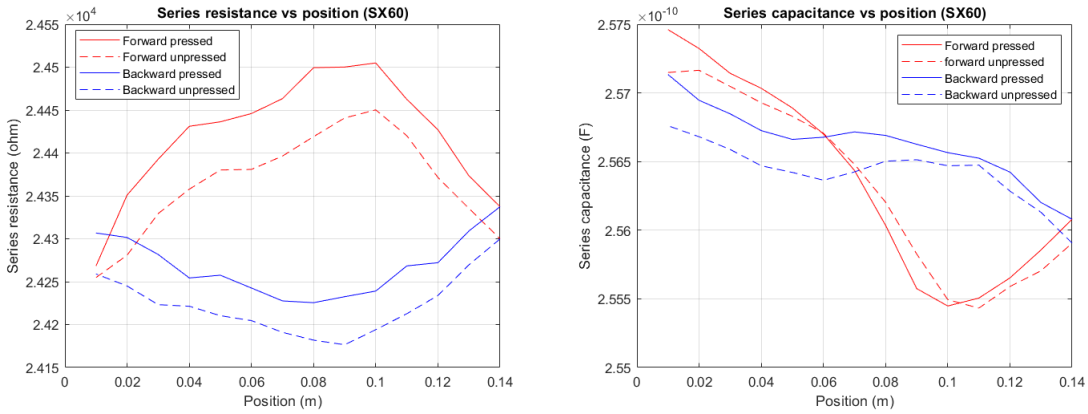

(a) Series resistance vs position

(b) Series resistance vs position

Figure B.1: Series resistance and capacitance measurements against position (HP4248A). The results show a reasonable consistency compared to sensor SNJ however, there still too much drift to resolve where the sensor was pressed.

B.2 Soft tip vs Hard tip DSX60INF (25 kHz)

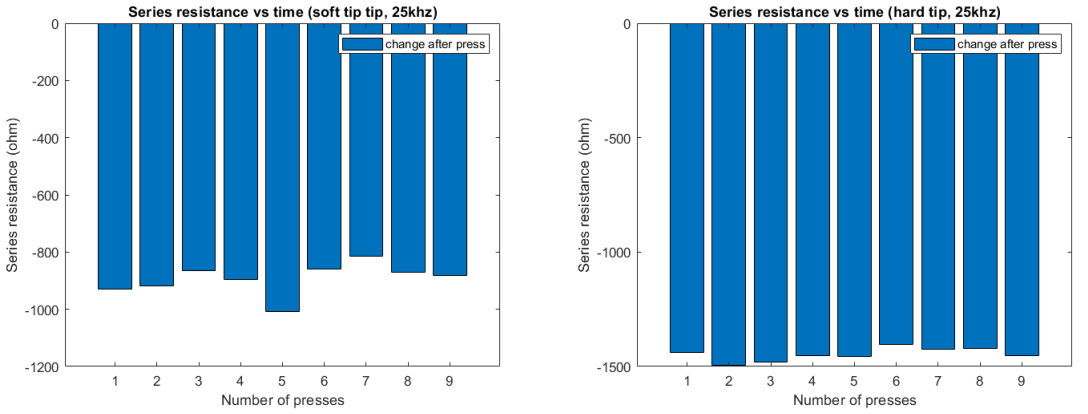

(a) Series resistance (Mean change −893 Ω)

(b) Series resistance (Mean change −1.44 kΩ)

Figure B.2: Comparison of change in series resistance between pressed and unpressed conditions for the two tips. The hard tip gives more change in resistance.

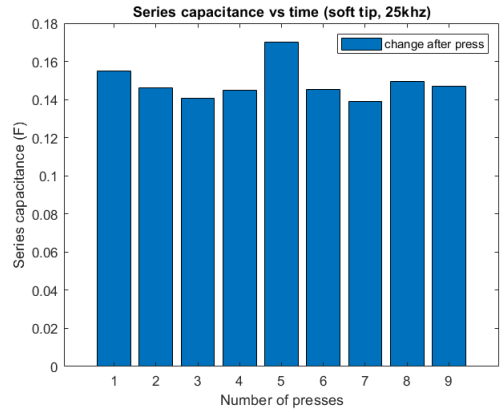

(a) Series capacitance (mean change 148 fF)

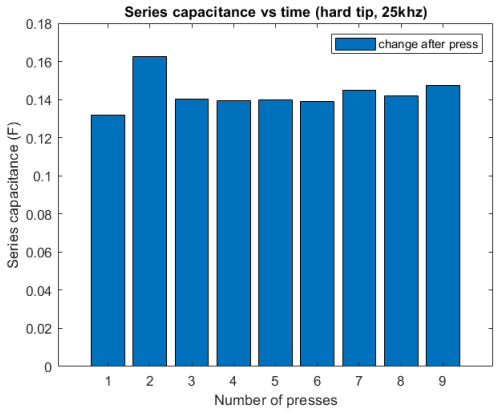

(b) Series capacitance (mean change 143 fF)

Figure B.3: Comparison of change in series capacitance between pressed and unpressed conditions for the two tips

B.3 Soft tip vs Hard tip DSX60INF (50 kHz)

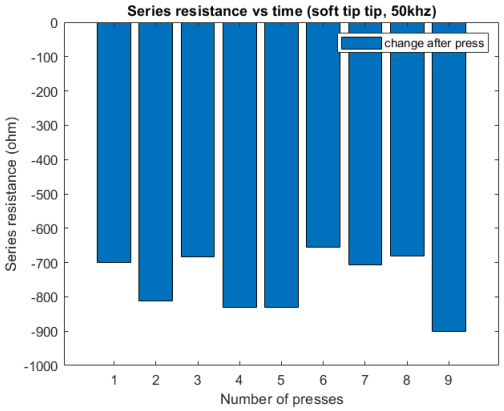

(a) Series resistance (Mean change −755 Ω)

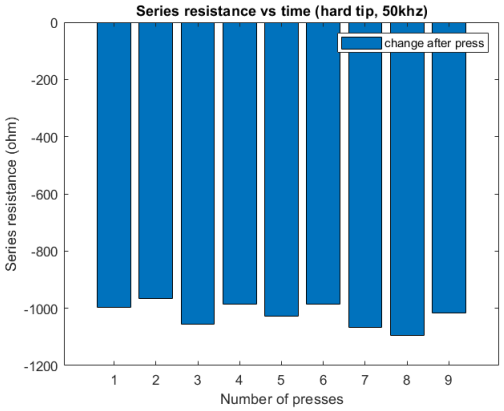

(b) Series resistance (Mean change −1.2 kΩ)

Figure B.4: Comparison of change in series resistance between pressed and unpressed conditions for the two tips. The hard tip gives more change in resistance.

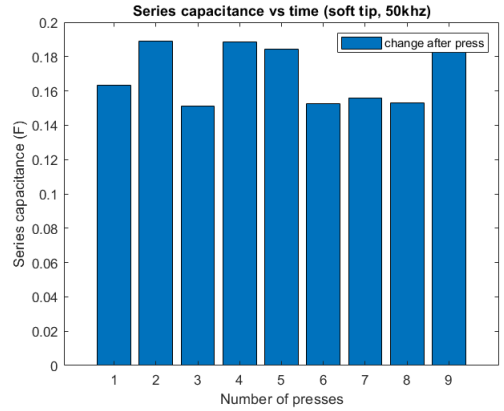

(a) Series capacitance (mean change 169 fF)

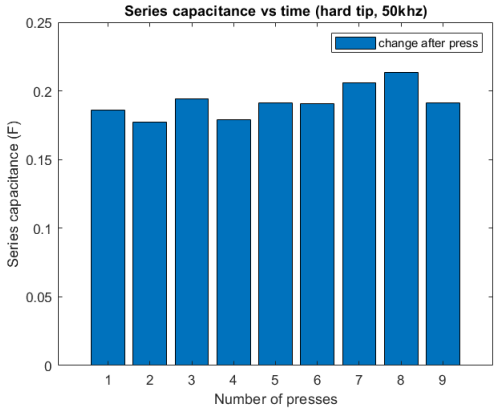

(b) Series capacitance (mean change 192 fF)

Figure B.5: Comparison of change in series capacitance between pressed and unpressed conditions for the two tips

B.4 Measurements with single electrode

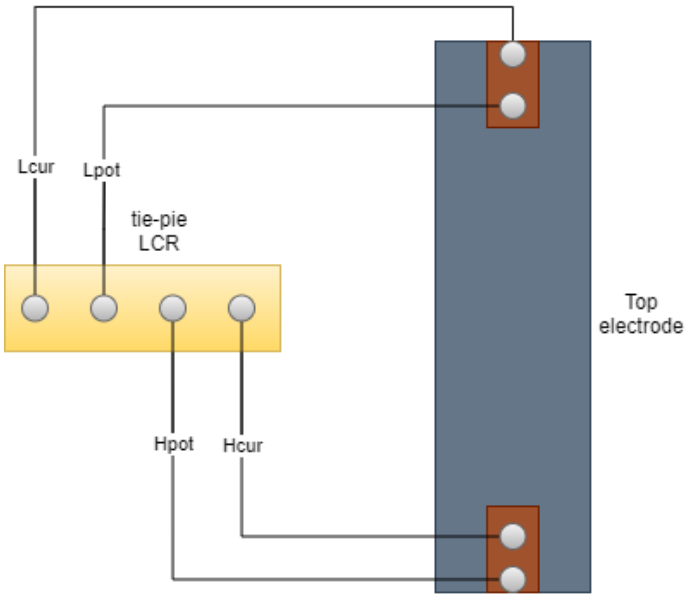

Figure B.6: Schematic of the connections for top electrode

B.4.1 Multiple presses at single point

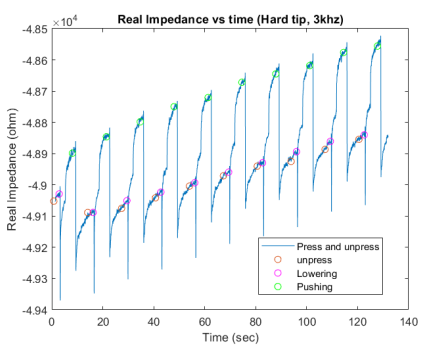

(a) Series resistance vs position

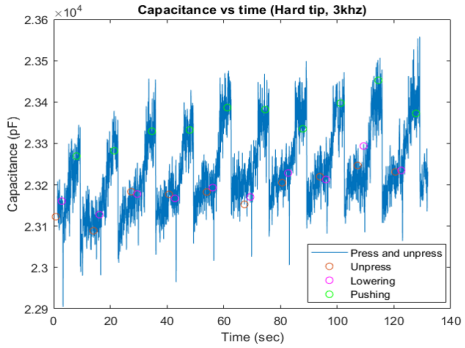

(b) Series resistance vs force and position

Figure B.7: Series resistance and capacitance measurements measurements of 10 presses at a single point. The measurement show drift.

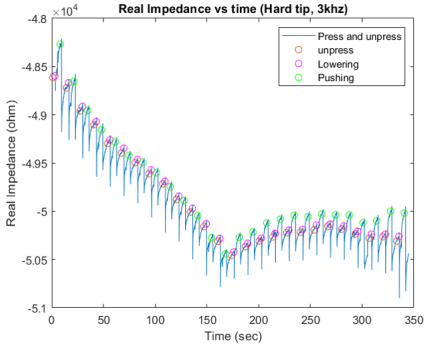

(a) Series resistance vs position

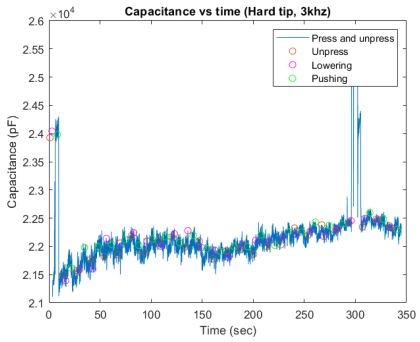

(b) Series resistance vs force and position

Figure B.8: Series resistance and capacitance measurements measurements by changing the position of the bed. The resistance measurement show drift.

Bibliography

[1] W. Yi, Y. Wang, G. Wang, and X. Tao, "Investigation of carbon black/silicone elastomer/dimethylsilicone oil composites for flexible strain sensors," *Polymer Testing*, vol. 31, no. 5, pp. 677–684, 2012.

[2] SMAC, "Linear_actuation_setup." https://www.smac-mca.com/lca-series-p-15.html.

[3] Keysight Technologies, "Impedance measurement handbook." https://www.keysight.com/nl/en/assets/7018-06840/application-notes/5950-3000.pdf. Access date: 17-02-2021.

[4] C. Weller, R. Kleer, and F. Piller, "Economic implications of 3d printing: Market structure models in light of additive manufacturing revisited," *International Journal of Production Economics*, vol. 164, 03 2015.

[5] Y. Xu, X. Wu, X. Guo, B. Kong, M. Zhang, X. Qian, S. Mi, and W. Sun, "The boom in 3d-printed sensor technology," *Sensors*, vol. 17, p. 1166, 05 2017.

[6] M. R. Khosravani and T. Reinicke, "3d-printed sensors: Current progress and future challenges," *Sensors and Actuators A: Physical*, vol. 305, p. 111916, 2020.

[7] M. Schouten, G. Wolterink, A. Dijkshoorn, D. Kosmas, S. Stramigioli, and G. Krijnen, "A review of extrusion-based 3d printing for the fabrication of electro-and biomechanical sensors," *IEEE Sensors Journal*, pp. 1–1, 2020.

[8] S. B. Kesner and R. D. Howe, "Design principles for rapid prototyping forces sensors using 3-d printing," *IEEE/ASME Transactions on Mechatronics*, vol. 16, no. 5, pp. 866–870, 2011.

[9] M. Schouten, R. Sanders, and G. Krijnen, "3d printed flexible capacitive force sensor with a simple micro-controller based readout," in *2017 IEEE SENSORS*, pp. 1–3, 2017.

[10] G. Wolterink, R. Sanders, and G. Krijnen, "Thin, flexible, capacitive force sensors based on anisotropy in 3d-printed structures," in *2018 IEEE SENSORS*, pp. 1–4, 2018.

[11] X. Aeby, R. v. Dommelen, and D. Briand, "Fully fdm 3d printed flexible capacitive and resistive transducers," in *2019 20th International Conference on Solid-State Sensors, Actuators and Microsystems Eurosensors XXXIII (TRANSDUCERS EUROSENSORS XXXIII)*, pp. 2440–2443, 2019.

[12] M. Saari, B. Xia, B. Cox, P. S. Krueger, A. L. Cohen, and E. Richer, "Fabrication and analysis of a composite 3d printed capacitive force sensor," *3D Printing and Additive Manufacturing*, vol. 3, no. 3, pp. 136–141, 2016.

[13] C. Hong, Y. Zhang, and L. Borana, "Design, fabrication and testing of a 3d printed fbg pressure sensor," *IEEE Access*, vol. 7, pp. 38577–38583, 2019.

[14] C. Hong, Y. Yuan, Y. Yang, Y. Zhang, and Z. A. Abro, "A simple fbg pressure sensor fabricated using fused deposition modelling process," *Sensors and Actuators A: Physical*, vol. 285, pp. 269–274, 2019.

[15] M. O. F. Emon, F. Alkadi, D. G. Philip, D.-H. Kim, K.-C. Lee, and J.-W. Choi, "Multi-material 3d printing of a soft pressure sensor," *Additive Manufacturing*, vol. 28, pp. 629–638, 2019.

[16] Y. Joo, J. Byun, N. Seong, J. Ha, H. Kim, S. Kim, T. Kim, H. Im, D. Kim, and Y. Hong, "Silver nanowire-embedded pdms with a multiscale structure for a highly sensitive and robust flexible pressure sensor," *Nanoscale*, vol. 7, no. 14, pp. 6208–6215, 2015.

[17] Y. Joo, J. Yoon, and Y. Hong, "Elastomeric nanowire composite for flexible pressure sensors with tunable sensitivity," *Journal of Information Display*, vol. 17, no. 2, pp. 59–64, 2016.

[18] F. Xu, X. Li, Y. Shi, L. Li, W. Wang, L. He, and R. Liu, "Recent developments for flexible pressure sensors: a review," *Micromachines*, vol. 9, no. 11, p. 580, 2018.

[19] S.-J. Woo, J.-H. Kong, D.-G. Kim, and J.-M. Kim, "A thin all-elastomeric capacitive pressure sensor array based on micro-contact printed elastic conductors," *Journal of Materials Chemistry C*, vol. 2, no. 22, pp. 4415–4422, 2014.

[20] C.-X. Liu and J.-W. Choi, "Patterning conductive pdms nanocomposite in an elastomer using microcontact printing," *Journal of Micromechanics and Microengineering*, vol. 19, no. 8, p. 085019, 2009.

[21] A. Rivadeneyra and J. A. López-Villanueva, "Recent advances in printed capacitive sensors," *Micromachines*, vol. 11, no. 4, p. 367, 2020.

[22] A. Perl, D. N. Reinhoudt, and J. Huskens, "Microcontact printing: limitations and achievements," *Advanced Materials*, vol. 21, no. 22, pp. 2257–2268, 2009.

[23] D. Xu, A. Tairych, and I. A. Anderson, "Stretch not flex: programmable rubber keyboard," *Smart Materials and Structures*, vol. 25, no. 1, p. 015012, 2015.

[24] J. Zhang, B. Yang, F. Fu, F. You, X. Dong, and M. Dai, "Resistivity and its anisotropy characterization of 3d-printed acrylonitrile butadiene styrene copolymer (abs)/carbon black (cb) composites," *Applied Sciences*, vol. 7, no. 1, p. 20, 2017.

[25] S. J. Leigh, R. J. Bradley, C. P. Purssell, D. R. Billson, and D. A. Hutchins, "A simple, low-cost conductive composite material for 3d printing of electronic sensors," *PloS one*, vol. 7, no. 11, p. e49365, 2012.

[26] A. Dijkshoorn, "Characterizing the anisotropic electrical properties of 3d printed conductive sheets." http://essay.utwente.nl/78084/, June 2019.

[27] NinjaTek, "Ninjaflex." https://ninjatek.com/ninjaflex/.

[28] M. Schouten, "Towards additively manufactured complex robotic systems," December 2017.

[29] W. Chen, X. Tao, P. Xue, and X. Cheng, "Enhanced mechanical properties and morphological characterizations of poly (vinyl alcohol)–carbon nanotube composite films," *Applied Surface Science*, vol. 252, no. 5, pp. 1404–1409, 2005.

[30] N. Stübler, J. Fritzsche, and M. Klüppel, "Mechanical and electrical analysis of carbon black networking in elastomers under strain," *Polymer Engineering & Science*, vol. 51, no. 6, pp. 1206–1217, 2011.

[31] H. Deng, L. Lin, M. Ji, S. Zhang, M. Yang, and Q. Fu, "Progress on the morphological control of conductive network in conductive polymer composites and the use as electroactive multifunctional materials," *Progress in Polymer Science*, vol. 39, no. 4, pp. 627–655, 2014.

[32] J.-C. Huang, "Carbon black filled conducting polymers and polymer blends," *Advances in Polymer Technology: Journal of the Polymer Processing Institute*, vol. 21, no. 4, pp. 299–313, 2002.

[33] Proto-pasta, "Conductive pla." https://www.proto-pasta.com/collections/all/products/conductive-pla.

[34] Palmiga-Innovation, "Pi-etpu85-700+ carbon black." https://rubber3dprinting.com/pi-etpu-95-250-carbon-black/.

[35] Ninjatek, "Eel." https://ninjatek.com/eel/.

[36] H. Watschke, K. Hilbig, and T. Vietor, "Design and characterization of electrically conductive structures additively manufactured by material extrusion," *Applied Sciences*, vol. 9, no. 4, p. 779, 2019.

[37] B. Eijking, R. Sanders, and G. Krijnen, "Development of whisker inspired 3d multi-material printed flexible tactile sensors," in *2017 IEEE SENSORS*, pp. 1–3, 2017.

[38] G. Wolterink, R. Sanders, F. Muijzer, B. van Beijnum, and G. Krijnen, "3d-printing soft semg sensing structures," in *2017 IEEE SENSORS*, pp. 1–3, 2017.

[39] G. Wolterink, A. Umrani, M. Schouten, R. Sanders, and G. Krijnen, "3d-printed calorimetric flow sensor," in *2020 IEEE SENSORS*, pp. 1–4, 2020.

[40] Makeshaper and Diabase, "X60." https://3dprint.com/167731/diabase-engineering-x60/.

[41] NinjaTek, "Ninjaflex." https://ninjatek.com/wp-content/uploads/2019/10/NinjaFlex-TDS.pdf.

[42] D. Engineering, "X60." https://flexionextruder.com/shop/x60-ultra-flexible-filament-natural/.

[43] D. Engineering, "Flexion extruder." https://www.diabasemachines.com/flexion-how-it-works.

[44] V. G. Surange and P. V. Gharat, "3d printing process using fused deposition modelling (fdm)," *International Research Journal of Engineering and Technology (IRJET), 3 (3)*, 2016.

[45] G. Ćwikła, C. Grabowik, K. Kalinowski, I. Paprocka, and P. Ociepka, "The influence of printing parameters on selected mechanical properties of fdm/fff 3d-printed parts," in *IOP conference series: materials science and engineering*, vol. 227, p. 012033, IOP Publishing, 2017.

[46] Y. Liu, H. Zhang, H. Porwal, J. J. Busfield, T. Peijs, and E. Bilotti, "Pyroresistivity in conductive polymer composites: a perspective on recent advances and new applications," *Polymer International*, vol. 68, no. 3, pp. 299–305, 2019.

[47] H. Tang, X. Chen, and Y. Luo, "Studies on the ptc/ntc effect of carbon black filled low density polyethylene composites," *European polymer journal*, vol. 33, no. 8, pp. 1383–1386, 1997.

[48] H. Xu, Y. Wu, D. Yang, J. Wang, and H. Xie, "Study on theories and influence factors of ptc property in polymer-based conductive composites," *Rev. Adv. Mater. Sci*, vol. 27, no. 2, pp. 173–183, 2011.

[49] S. K. Lee, Y. R. Kim, T. J. Yoo, J. H. Park, and J. H. Kim, "Study on electrical characteristics of fdm conductive 3d printing according to annealing conditions," *Journal of the Korean Society of Manufacturing Process Engineers*, vol. 17, no. 6, pp. 53–60, 2018.

[50] S. K. Lee, Y. C. Oh, and J. H. Kim, "Manufacturing experiments using fdm 3d-printed flexible resistance sensors with heterogeneous polymer material annealing," *Korean Society of Mechanical Engineers*, vol. 19, no. 1, pp. 81–88, 2020.

[51] M. Schouten, "diabase_cura_post_processor." https://github.com/martijnschouten/diabase_cura_post_processor.

[52] Fiberology, "Bvoh." https://fiberlogy.com/en/fiberlogy-filaments/bvoh/.

[53] L. Stauffer, "Cv measurement tips, tricks, and traps," *Technical report*, 2008.

[54] E. Dumitru and M. O. Popescu, "Methods of reducing capacitive coupling between five conductors located on a pcb," in *2013 4th International Youth Conference on Energy (IYCE)*, pp. 1–5, 2013.

[55] Stratasys, "Verocblack." https://https://www.stratasys.com/materials/search/vero.

[56] Stratasys, "Agilus30." https://www.stratasys.com/materials/search/agilus30.

[57] Stratasys, "Veroclear." https://www.stratasys.com/materials/search/veroclear.